Dissertation
submitted to the
Combined Faculties for the Natural Science and for Mathematics
of the Ruperto-Carola university of Heidelberg, Germany
for the degree of Doctor of Natural Sciences

Put forward by

Diplom-Physikerin: **Anke A. Wagner**
Born in: **Mainz**

Oral examination: February 7, 2013

The g-factor of the valence electron bound in lithiumlike silicon $^{28}Si^{11+}$:

The most stringent test of relativistic many-electron calculations in a magnetic field

Referees: Prof. Dr. Klaus Blaum

Prof. Dr. Selim Jochim

Für meine Eltern

The g-factor of the valence electron bound in lithiumlike silicon $^{28}Si^{11+}$: The most stringent test of relativistic many-electron calculations in a magnetic field: Within this thesis the g-factor of the valence electron bound in lithiumlike silicon $^{28}Si^{11+}$ has been measured with a relative precision of $\delta g/g = 1.1 \cdot 10^{-9}$. The determination of the g-factor is based on a measurement of the free cyclotron and the Larmor frequency of a single ion stored in a triple Penning trap setup. The free cyclotron frequency is determined from the non-destructive measurement of the eigenfrequencies of the trapped ion. To determine the Larmor frequency the continuous Stern-Gerlach effect is employed, which couples the spin orientation to the axial mode. Thus, a spin flip manifests as a tiny frequency jump of the axial frequency. The implementation of dedicated stabilization systems for temperature and magnetic field minimized environmental influences on the ion. The presented result $g_{\mathrm{exp}} = 2.000\,889\,889\,9(21)$ constitutes the most precise g-factor measurement of a three-electron system to date. It is in excellent agreement with the theoretical prediction $g_{\mathrm{theo}} = 2.000\,889\,909(51)$ and confirms the relativistic many electron calculations at the level of 10^{-4}. Since the sensitivity of this test is limited by the theoretical value, which is more than order of magnitude less precise than the experimental result, any further improvement of the theoretical uncertainty will directly improve the test of the relativistic many-electron calculations.

Der g-Faktor des Valenzelektrons gebunden in lithiumähnlichem Silizium $^{28}Si^{11+}$: Der genaueste Test der relativistischen Mehrelektronen-Rechnungen in einem magnetischen Feld: Im Rahmen dieser Arbeit wurde der g-Faktor des Valenzelektrons gebunden in lithiumähnlichem Silizium mit einer relativen Genauigkeit von $\delta g/g = 1.1 \cdot 10^{-9}$ gemessen. Die Bestimmung des g-Faktors erfolgt über eine Messung der freien Zyklotron- und der Larmorfrequenz eines einzelnen Ions gespeichert in einem dreifachen Penning-Fallensystem. Die freie Zyklotronfrequenz wird über den nicht-destruktiven Nachweis der Eigenfrequenzen des gespeicherten Ions bestimmt. Um die Larmorfrequenz zu bestimmen wird der kontinuierlichen Stern-Gerlach Effekts angewendet, der die Spinrichtung an die axiale Bewegung koppelt. Eine Änderung der Spinrichtung kann somit über einen extrem kleinen axialen Frequenzsprung bestimmt werden. Der Einfluss von äußeren Einflüssen auf das Ion konnte durch geeignete Stabilisierungssysteme für Temperatur und Magnetfeld reduziert werden. Das vorgestellte Ergebnis $g_{\mathrm{exp}} = 2.000\,889\,889\,9(21)$ ist die bisher genaueste Bestimmung des g-Faktors eines drei-Elektronen-Systems. Es ist in hervorragender Übereinstimmung mit dem theoretischen Wert $g_{\mathrm{theo}} = 2.000\,889\,909(51)$ und bestätigt die relativistischen Mehrelektronen-Rechnungen auf einem Level von 10^{-4}. Da die erreichte Genauigkeit des Tests durch den theoretischen Wert limitiert ist, welcher mehr als eine Größenordnung ungenauer ist als das experimentelle Ergebnis, wird jede weitere Verbesserung der theoretischen Unsicherheit direkt den erzielten Test der Mehrelektronen-Rechnungen verbessern.

Contents

List of Figures

List of Tables

Chapter 1

Introduction

The Standard Model is an important step towards the long term goal of physics - the complete understanding of all physical processes and their description within one grand unified theory [1]. However, only three of the four known forces, the electromagnetic, the weak and the strong force, are included in the Standard Model whereas gravitation is not included. Furthermore, there are still open questions, which cannot be answered, e.g. the finite mass of the neutrino or the matter-antimatter asymmetry. This leads to the conclusion that there has to be new physics beyond the Standard Model and a theory describing these effects.
To date the most successful quantum field theory [2,3] and thus "*the jewel of physics - our proudest possession*" [4], is the quantum electrodynamics (QED) theory, which describes the interaction between charged particles and light. The experimental discovery of the Lamb shift [5] and the anomaly of the magnetic moment of the electron [6] in 1947 marked the beginning of QED, which proved the importance of experiments to continuously question the existing theories. Since its beginnings QED has been the testing object of a large number of dedicated experiments and no discrepancy between the theoretical prediction and the experimental observation could be found so far. This great success of QED indicates that a possible deviation from QED most likely is very small and thus requires experiments performed at high-precision. To this end, Penning-trap based experiments provide an excellent possibility for highest precision measurements with single ions at lowest energies [7]. This has already been demonstrated in 1977 by Dehmelt and coworkers, who measured the g-factor of the free electron in a Penning trap to $\delta g/g = 2 \cdot 10^{-10}$ [8]. The accuracy for this value has been further improved over the years to presently $3 \cdot 10^{-13}$ [9]. Comparison with the theoretical prediction, which has been recently calculated with an uncertainty as low as $7 \cdot 10^{-13}$ [10], enables the most stringent test of free QED at a level of $7 \cdot 10^{-10}$.
Although QED has already been tested to an outstanding precision at low energies and fields there is still a need for stringent tests at high energies and strong fields. The highest accessible fields are provided by highly-charged ions, where a field strength for the remaining

electron(s) due to the binding potential of the nucleus of up to 10^{16} V/cm for hydrogenlike uranium can be achieved. Especially few-electron systems can be calculated to an impressive accuracy and thus provide the possibility for stringent tests of QED at high fields. The QED calculations dealing with the properties of electrons bound to a nucleus are denoted as bound-state QED (BS-QED) [11]. Due to the additional binding field of the nucleus and the consideration of the nucleus itself as well as interaction with possible additional electrons, the BS-QED calculations are more challenging than calculations of the free electron. For a test of QED mainly

- the Lamb shift
- the hyperfine splitting HFS and
- the g-factor

are investigated, since the corresponding observables can be both calculated and measured to a high accuracy [12, 13]. Tests of these three specific characteristics complement one another since the sensitivity towards particular contributions, the available field strength and the achievable precision are different. The scaling of the particular operators, e.g., is essentially different. The hyperfine splitting operator scales with $\sim 1/r^2$, the Lamb shift operator with $\sim 1/r$ and the g-factor operator with $\sim r$, where r is the distance of the electron to the nucleus. Accordingly, the main contribution to the hyperfine splitting arises from the behaviour of the electron wave function close to the nucleus and thus provides access to the highest achievable field strengths [14]. The g-factor, on the other hand, is mainly determined by the behaviour of the wave function on atomic scales. As a result the g-factor is less sensitive to nuclear parameters and thus can be calculated with a significantly higher accuracy [15], hereby enabling a highly sensitive test of QED effects. This has been impressively demonstrated recently by our group with the g-factor measurement of hydrogenlike silicon $^{28}Si^{13+}$ with an uncertainty of $\delta g_{\mathrm{exp}}/g_{\mathrm{exp}} = 5 \cdot 10^{-10}$. The experimental result is, once more, in excellent agreement with the theoretical prediction with an uncertainty of $\delta g_{\mathrm{theo}}/g_{\mathrm{theo}} = 8.5 \cdot 10^{-10}$ and thus provides the most stringent test of QED at strong fields to date [16].

Since the BS-QED contributions increase with the nuclear charge Z, the sensitivity towards these corrections increases for heavier ions assuming that the theoretical and experimental precision are independent from Z. However, for the g-factor as well as for the hyperfine splitting, the achievable theoretical precision for heavy ions is limited by poorly known nuclear parameters. In both cases, this limitation can be overcome by comparing the lithium- and the hydrogenlike charge state of the same isotope since the limiting uncertainties are significantly reduced in the specific difference [14, 17]. Accordingly, for a stringent test of QED in heavy ions the lithiumlike system has to be measured with a comparable accuracy

as the hydrogenlike one.
Moreover, investigations of lithiumlike ions can be used to probe the many-electron calculations itself. The g-factor is especially suited, since here the many electron contributions are of purely relativistic origin [18]. As a result the correct treatment can only be performed within the *ab initio* QED approach. Previously, the g-factors of lithium ^{6,7}Li and lithiumlike beryllium $^{9}Be^{+}$ have been measured. The atomic beam magnetic resonance method was employed to determine the g-factor of ^{6,7}Li with an uncertainty of $\delta g/g = 1 \cdot 10^{-6}$ [19]. The g-factor of $^{9}Be^{+}$ has been measured by laser-induced fluorescence technique with an uncertainty of $\delta g/g = 2 \cdot 10^{-7}$ [20] and confirmed the many electron QED at the level of $5 \cdot 10^{-3}$. There are approaches to test many-electron calculations in other systems, e.g. lifetime measurements [21] or energy transition measurements in boronlike argon [22]. However, these tests are not (yet) as sensitive to QED corrections as the g-factor, since the considered many-electron QED contributions for these systems are by one order of perturbation smaller than for the g-factor calculation.
In the course of this thesis the g-factor of the $2s$ valence electron bound in lithiumlike silicon $^{28}Si^{11+}$ has been measured with a relative uncertainty of $\delta g/g = 1.1 \cdot 10^{-9}$. The measurement is performed with a single ion, which is stored in a cryogenic Penning trap for almost arbitrary long storage times. The determination of the g-factor is based on the measurement of the Larmor frequency in well known magnetic field. To determine the magnetic field strength the free cyclotron frequency of the ion is measured simultaneously to the Larmor frequency, hereby cancelling magnetic field fluctuations in the leading order and thus enabling the measurement of the g-factor to a very high precision. The free cyclotron frequency is obtained by non-destructively measuring the eigenfrequencies of the ion in a homogeneous magnetic field. For the determination of the Larmor frequency microwaves are irradiated to induce spin flips, which are detected with the continuous Stern-Gerlach effect [23]. A magnetic bottle field is employed to couple the spin orientation to the axial oscillation, which results in a tiny axial frequency jump for a spin flip. To spatially separate the measurement of the eigenfrequencies and the detection of spin flips, a triple Penning trap setup has been developed. The third trap is required for the in-trap production of the highly-charged ions. Compared to the previous measurements of ^{6,7}Li and $^{9}Be^{+}$, the uncertainty of the g-factor of $^{28}Si^{11+}$ is improved by more than two orders of magnitude and the sensitivity to the many electron effects is increased by a factor of 15. Thus the presented measurement constitutes the most precise g-factor measurement of a three-electron system to date and confirms the relativistic many electron calculations at the level of 10^{-4} limited in accuracy by the theoretical value.

This thesis is ordered in the following way: The second chapter starts with a short historical overview over g-factor measurements and discusses the advantages of a comparison between lithium- and hydrogenlike g-factors for heavy ions. Afterwards, the basic principles

of the theoretical calculations of the g-factor are described, starting with the free electron and continuing with the (valence) electron bound in hydrogen- and lithiumlike ions. At the end of the second chapter the experimental measurement principle is introduced. Chapter three is dedicated to the Penning trap and the eigenfrequencies of the stored ion. The non-destructive detection techniques for the three eigenfrequencies in the two measurement traps as well as the spin state detection are addressed by chapter four. In chapter five the experimental setup of our experiment is presented. Chapter six deals with the stabilization systems, which have been developed in the course of this thesis. The preparative measurements required for a g-factor measurement are presented in chapter seven. In chapter eight the g-factor measurement is described and the possible uncertainties, which have to be considered are discussed. Finally, the experimental g-factor value for lithiumlike silicon is presented and compared to the theoretical prediction. The thesis is concluded with a brief summary of the achieved results and an outlook to future measurements in chapter nine.

Chapter 2

The g-factor

The gyromagnetic-factor (g-factor) is the dimensionless proportionality constant g[1], which connects the magnetic moment $\boldsymbol{\mu}$[2] of a charged particle to its spin $\mathbf{S}$

$$\boldsymbol{\mu} = -g\frac{e}{2m_\mathrm{e}}\mathbf{S} = -g\mu_\mathrm{B}\frac{\mathbf{S}}{\hbar}. \tag{2.1}$$

Here e and m_e are the charge and the mass of the electron, respectively, and $\mu_\mathrm{B} = e\hbar/(2m_\mathrm{e})$ is the Bohr magneton.

This magnetic moment originating from the spin caused the spatial splitting of a beam of silver atoms within an inhomogeneous magnetic field, which was first observed by Stern and Gerlach in 1922 [23]. Since the silver atoms do not have an angular momentum (L=0) this observation cannot be explained by classical physics. Three years later Goudsmit and Uhlenbeck introduced a quantized inner angular momentum [24], the spin, being responsible for the detected splitting. Another three years later, in 1928, Dirac formed his relativistic Dirac equation [25], which for the first time accounts for the spin of a particle and explains the corresponding magnetic moment. The value of the g-factor for the free electron can be derived from the Dirac equation to $g = 2$. In 1947, the first measurement of the electron g-factor was performed by Kusch and Foley [6], who measured the Zeeman splitting of the energy levels in gallium in a constant magnetic field. They determined a g-factor of $g = 2.002\,29(8)$ and therefore a small deviation from the predicted value of $g = 2$. This anomaly could be explained by quantum electrodynamics (QED) and its observation along with the discovery of the Lamb shift [5] resulted in an increasing interest and effort put into theoretical QED-calculations.

In the following decades several experiments with different approaches were performed to determine the g-factor of free electrons (see for example Ref. [26] and references therein). A major breakthrough in gaining precision was obtained by performing experiments with single

[1] If not marked differently g always denotes the electron spin g-factor g_s.

[2] In the course of this thesis bold letters indicate vectors.

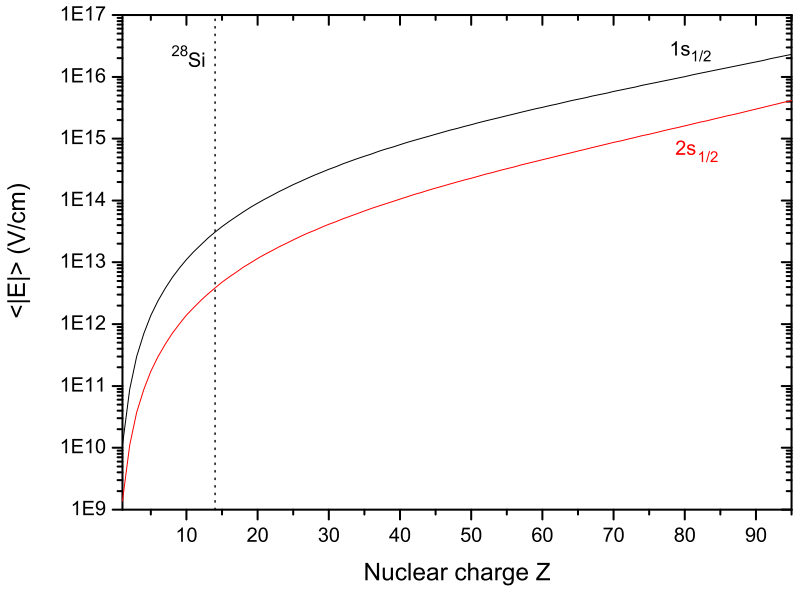

Figure 2.1: Electric field strength at the position of the remaining electron in hydrogenlike ions (black line) and the valence electron in lithiumlike ions (red line).

particles. In 1977 Van Dyck, Schwinberg and Dehmelt measured the g-factor of a single electron stored in a Penning trap with a remarkable precision to $g_{\mathrm{exp}}/2 = 1.001\,159\,652\,410(200)$ [8]. This precision could be even further improved and the most precise value up to date was measured by Gabrielse and co-workers in 2008 to $g_{\mathrm{exp}}/2 = 1.001\,159\,652\,180\,73(28)$ [9]. The theoretical value $g_{\mathrm{theo}}/2 = 1.001\,159\,652\,181\,78(77)$ [10] is in good agreement with the experimental value and demonstrates the great success of the QED and its predictions.
However, new effects beyond QED are expected to appear most likely in extreme situations, like strong electric or magnetic fields, where potential nonlinearities of QED in the field tensor $F^{\mu\nu}$ might become visible [27]. Therefore, it is of great interest to test QED in the high-field region. An optimal system is the g-factor of the electron bound to highly-charged ions, where it is possible to achieve electric field strengths at the position of the remaining electron(s) (see Fig. 2.1), which are otherwise not accessible in laboratories. Additionally, theoretical calculations for few-electron systems and especially hydrogenlike ions are well under control and high accuracies for the theoretical g-factor can be achieved.
In 2000 the g-factor of the electron bound in hydrogenlike carbon $^{12}C^{5+}$ has been measured with a relative uncertainty of $\delta g/g = 2.5 \cdot 10^{-9}$ [28] and in 2004 the measurement of the g-factor of $^{16}O^{7+}$ to $\delta g/g = 7.5 \cdot 10^{-10}$ [29] was performed. The recent measurement of hydrogenlike silicon $^{28}Si^{13+}$ to $\delta g/g = 5 \cdot 10^{-10}$ [16] is completely limited in accuracy by the

uncertainty of the electron mass. These measurements in combination with the corresponding theoretical values [15,30–33] demonstrated that the g-factor can be both calculated and measured to an impressive accuracy. However, the increasing contribution of nuclear size and nuclear polarization corrections, described in Sec. 2.1.2, put a limit on the theoretical accuracy for higher nuclear charges Z since the nuclear properties are only poorly known. As a result the g-factor of hydrogenlike uranium can only be calculated to $3 \cdot 10^{-6}$ due to the uncertainty of the nuclear size correction [17]. To partly overcome this limitation Shabaev and coworkers proposed to measure two charge states of the same isotope [17]. In fact, a favourable system from the theoretical point of view would be a hydrogenlike ion with the electron excited to the $2s$-state, since in this case additional electrons would not complicate the theoretical calculations. This system, however, cannot be investigated experimentally with sufficient precision due to the finite lifetime of the $2s$-state. Therefore, lithiumlike systems are employed where the principle remains the same but additional corrections due to the interelectronic interaction have to be considered.

The advantage of comparing the lithium- and the hydrogenlike g-factor can be seen, following [34,35], from the radial Dirac equations for an electron bound in the Coulomb potential $V(r)$ of the nucleus

$$\begin{aligned} \hbar c \left[\frac{d}{dr} + \frac{1+\kappa}{r} \right] g_{n\kappa}(r) - [E_{n\kappa} + m_e c^2 - V(r)] f_{n\kappa}(r) = 0, \\ \hbar c \left[\frac{d}{dr} + \frac{1-\kappa}{r} \right] f_{n\kappa}(r) + [E_{n\kappa} - m_e c^2 - V(r)] g_{n\kappa}(r) = 0. \end{aligned} \tag{2.2}$$

They have to be obeyed by the large and small radial components of the wavefunction $g_{n\kappa}(r)$ and $f_{n\kappa}(r)$ for defined n and κ. Here, n is the principal quantum number, κ is defined as $\kappa = (-1)^{j+l+1/2}(j+1/2)$, with l being the electron's orbital angular momentum and j its total angular momentum. $E_{n\kappa}$ denotes the binding energy. If κ is kept constant and the quantum number n is varied, the radial Dirac equations remain the same except for the binding energy. Close to the nucleus the binding energy is much smaller than the Coulomb potential $E_n \ll V(r)$ and thus, the resulting radial wavefunctions for the electron located in different atomic shells are similar except for a constant normalization factor. This normalization factor is almost independent on the nuclear structure but depends mainly on the behaviour of the wavefunction at the atomic scale. Therefore, it can be calculated with a high precision. As a result, the dependence of the ratio of the nuclear size contribution for the lithium- and the hydrogenlike g-factor $\xi = \Delta g_{NS}^{(1s)^2 2s} / \Delta g_{NS}^{1s}$ on the nuclear parameters is suppressed by two orders of magnitude compared to the nuclear size correction itself. Accordingly, the uncertainty due to the nuclear size correction is significantly reduced in the difference of the g-factors for two charge states, in this case for the $(1s)^2 2s_{1/2}$ and the $1s_{1/2}$ state

$$g' = g_{(1s)^2 2s_{1/2}} - \xi g_{1s_{1/2}}, \tag{2.3}$$

which therefore, can be calculated to a significantly higher accuracy than the individual g-factors.
The great interest in the g-factor of the valence electron in lithiumlike ions is, however, not only motivated by the increased achievable precision of the QED test for heavy ions, but also originates from the fact that it constitutes an excellent test object for the relativistic calculations of the electron-electron interaction. The g-factor is a well suited system for this task, since here these interactions are of purely relativistic origin. In the non-relativistic treatment the interaction would simply vanish even for many electrons. As a result, the negative-energy Dirac continuum has to be considered within the calculations since its contribution is of the same order of magnitude as that of the positive energy-states.
A few three-electron systems have been investigated previously. In 1967 the electronic g-factors of ^{6,7}Li have been measured to $\delta g/g = 1 \cdot 10^{-6}$ with the atomic beam magnetic resonance technique [19] and in 1983 D. Wineland *et al.* determined the g-factor of $^{9}Be^{+}$ with the laser-induced fluorescence technique to $\delta g/g = 2 \cdot 10^{-7}$ [20]. In the course of this thesis the g-factor of lithiumlike silicon ion $^{28}Si^{11+}$ has been determined to $\delta g/g = 1.1 \cdot 10^{-9}$ using a single trapped ion. The measurement represents the most precise g-factor determination of a three electron system to date. The comparison with the theoretical value yields the most stringent test of relativistic many-electron calculations in magnetic fields.

This chapter starts with the description of the theoretical calculations for the g-factor of the free electron and continues with the (additional) calculations for hydrogen- and lithiumlike ions, being more and more complex since further corrections and thus additional series expansions have to be considered. Finally, the experimental measurement principle for the g-factor of the electron bound in highly-charged ions is presented.

2.1 Theoretical *g*-factor

2.1.1 The *g*-factor of the free electron

The deviation from $g = 2$ for the free electron originates from the interaction between the electron and the background electromagnetic field and can be explained within the framework of QED. As usual within QED, the g-factor is expressed as a series expansion

$$\begin{aligned} g =& 2 \cdot (+A_2 \cdot \left(\frac{\alpha}{\pi}\right) + A_4 \cdot \left(\frac{\alpha}{\pi}\right)^2 + A_6 \cdot \left(\frac{\alpha}{\pi}\right)^3 + A_8 \cdot \left(\frac{\alpha}{\pi}\right)^4 \\ & + ... + a_{\text{hadronic,electroweak}}), \end{aligned} \tag{2.4}$$

where $a_{\text{hadronic,electroweak}}$ denotes the contribution of the hadronic and the electroweak interaction, respectively. The power of the fine-structure constant $\alpha \approx 1/137$ accounts for the number of virtual photons involved in the particular considered process. Due to the small

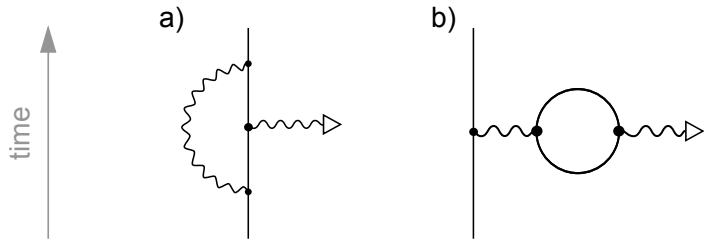

Figure 2.2: Feynman diagrams for the self-energy (a) and the vacuum polarization (b) of the free electron interacting with an external magnetic field. The solid line represents the free electron propagator, the waved line a photon. The triangle indicates the interaction with the external magnetic field.

value of the coupling constant $\alpha \ll 1$ and the fact that the coefficients are numbers of the order of unity the series converges rapidly.
Since the electron interacts with the electromagnetic field, it permanently emits and absorbs virtual photons, a process which is called self-energy (see Fig. 2.2 a). Furthermore, a virtual electron-positron pair can be produced from a virtual photon and then annihilates back to a virtual photon. This is denoted as vacuum polarization (see Fig. 2.2 b). Since both processes change the energy of the electron they contribute to the g-factor as well. The self-energy was first calculated by Schwinger to α/π, corresponding to $A_2 = 1/2$ [36]. Accordingly, this lowest order radiative correction term is often denoted as "Schwinger-term". The A_4- and A_6-coefficients have been calculated analytically, while the A_8-coefficient, implying the evaluation of 891 four-loop Feynman diagrams, has been calculated numerically. The analysis of the 12672 Feynman diagrams for the A_{10}-coefficient has been completed just recently and improved the precision of the theoretical value to $g_{\mathrm{theo}}/2 = 1.001\,159\,652\,181\,78(77)$ [10].
For the calculation of the g-factor, however, also the value of the fine-structure constant is required. In 2011 an independent determination of the fine-structure constant with a relative uncertainty of $6.6{\cdot}10^{-10}$ from a rubidium recoil experiment was performed, which enabled a test of QED on the 10^{-9}-level [37]. Nevertheless, the uncertainty of the theoretical value is completely dominated by the uncertainty of the fine-structure constant and thus one can turn it around. Assuming that the QED calculations are correct one can adjust α to a value that experimental and theoretical values coincide. From the Harvard experimental value for g-2 experiment $g_{\mathrm{exp}}/2 = 1.001\,159\,652\,180\,73(28)$ [9] the most precise value for the fine-structure constant $\alpha^{-1} = 137.035\,999\,173(35)$ [10] is obtained.

2.1.2 The g-factor of the bound electron

For the g-factor of the electron bound to a nucleus, several additional terms have to be taken into account. They can be classified into relativistic contributions (Breit), QED

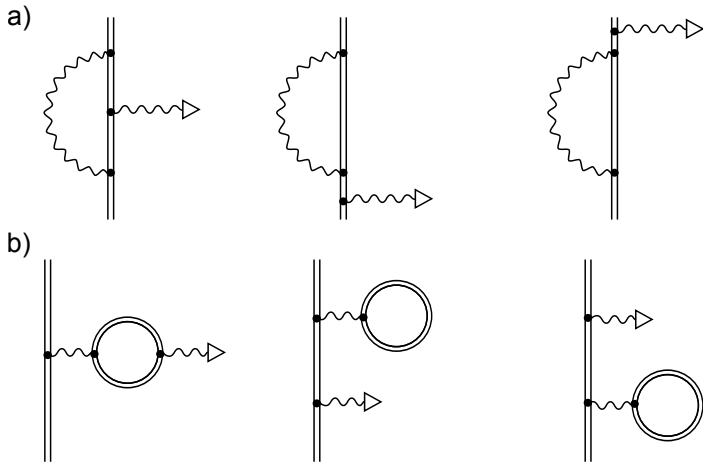

Figure 2.3: Feynman diagrams for the first order BS-QED correction (self-energy (a) and vacuum polarization (b)) of the bound electron. The double line represents the bound electron propagator and therefore contains the interaction between electron and binding field to all orders of $Z\alpha$.

contributions of the free and the bound electron and nuclear contributions

$$g = 2 + \Delta g_{\text{Breit}} + \Delta g_{\text{free}} + \Delta g_{\text{BS-QED}} + \Delta g_{\text{nucleus}} \tag{2.5}$$

and will be described in the following.

Relativistic contribution

In 1928 Breit performed the first calculation of the g-factor of an electron bound in a hydrogenlike ion within an external magnetic field by solving the Dirac equation for this system [38]. He obtained:

$$g_{\text{D}} = 2 + \Delta g_{\text{Breit}} = \frac{2}{3}\left[1 + 2\sqrt{1-(Z\alpha)^2}\right]. \tag{2.6}$$

This value still assumes a point-like and infinitely heavy nucleus but already considers the relativistic contribution.

Bound-state QED corrections

Going to the bound electron means that the impact of the binding field of the nucleus on the g-factor has to be considered. Accordingly, those calculations are denoted as bound-state QED (BS-QED) calculations. There are two possible approaches to include the photon exchange between electron and nucleus:

1. A second series expansion in $Z\alpha$ is introduced, which means that for each order in α a series expansion in $Z\alpha$ has to be evaluated. Accordingly, the coefficients A_i for the

free electron have to be extended to $Z\alpha$-dependent coefficients C_i and the g-factor of an infinitely heavy and pointlike nucleus then reads:

$$\begin{aligned} g = g_{\mathrm{D}} &+ \left(\frac{\alpha}{\pi}\right) \cdot [A_2 + C_2^1 \cdot (Z\alpha)^2 + C_2^2 \cdot (Z\alpha)^4 + ...] \\ &+ \left(\frac{\alpha}{\pi}\right)^2 \cdot [A_4 + C_4^1 \cdot (Z\alpha)^2 + C_4^2 \cdot (Z\alpha)^4 + ...] \\ &+ \left(\frac{\alpha}{\pi}\right)^3 \cdot [A_6 + C_6^1 \cdot (Z\alpha)^2 + C_6^2 \cdot (Z\alpha)^4 + ...] \\ &+ ... \,. \end{aligned} \tag{2.7}$$

2. The free electron propagator within the calculations is replaced by the eigenfunctions derived from the solution of the Dirac equation for the bound system.

In the first case, there arises a problem at least for heavier elements. The value of $Z\alpha$ approaches unity, the series expansion converges much less rapidely and very high orders would have to be considered for high precision. The second possibility provides a complete solution and decreases the number of Feynman diagrams considerably since the interaction with the nucleus is already included within the bound electron propagator (see Fig. 2.3). However, the resulting integral can only be calculated numerically and the computation is very difficult. Presently only the corrections up to the one-loop level (α/π) have been evaluated by employing the bound electron propagator, whereas the two-loop contributions ($(\alpha/\pi)^2$) have been calculated within a series expansion in $Z\alpha$. The uncalculated higher order terms of this series expansion limit the accuracy for the theoretical g-factor of hydrogenlike silicon.

Nuclear corrections

To calculate the g-factor with sufficient accuracy the nucleus cannot be considered as pointlike and infinitely heavy, but corrections due to its mass, size and shape have to be taken into consideration:

- The **nuclear recoil correction** accounts for the finite mass and thus the movement of the nucleus, which can be considered by an additional series expansion in $m_{\mathrm{e}}/M_{\mathrm{n}}$, with M_{n} being the mass of the nucleus. It has been calculated in [31] to all orders in αZ and to first order in $m_{\mathrm{e}}/M_{\mathrm{n}}$.

- Since the wavefunction of the electron depends on the nuclear charge distribution and thus on shape and size of the nucleus, the g-factor has to be corrected for the **finite nuclear size effect** [33, 39].

- Through the exchange of a virtual photon, nuclear levels can be excited, which is denoted as **nuclear polarization effect**. The influence on the g-factor has been calculated in [40].

Dirac		1.998 254 751
QED	α	0.002 324 044 (3)
	α^{2+}	−0.000 003 517 (1)
Interelectronic interaction	$1/Z$	0.000 321 592
	$1/Z^2$	−0.000 006 876 (1)
	$1/Z^{3+}$	0.000 000 085 (22)
screened QED	α/Z^{+}	−0.000 000 212 (46)
Nuclear effects	Recoil	0.000 000 039 (1)
	Finite size	0.000 000 003
Total theory		2.000 889 909 (51)

Table 2.1: The individual contributions to the theoretical g-factor of lithiumlike silicon $^{28}Si^{11+}$, which were calculated by D.A. Glazov, A.V. Volotka and V.M. Shabaev [41]. The "+" indicates that higher orders are included.

2.1.3 The *g*-factor of lithiumlike ions

The presence of more than one electron and the resulting mutual interaction complicate the calculations for lithiumlike systems and limit the theoretical accuracy at least for low and middle Z. Accordingly, there are again additional contributions, which have to be calculated for the g-factor of an electron bound to a lithiumlike ion:

$$g = g_{\mathrm{D}} + \Delta g_{\mathrm{int}} + \Delta g_{\mathrm{QED}} + \Delta g_{\mathrm{BSQED}} + \Delta g_{\mathrm{recoil}} + \Delta g_{\mathrm{NS}} + \Delta g_{\mathrm{NP}}. \tag{2.8}$$

g_{D} represents the one-electron Dirac value for a pointlike nucleus, Δg_{int} is the interelectronic interaction, Δg_{QED} is the QED correction, Δg_{SQED} is the screened QED correction and $\Delta g_{\mathrm{recoil}}$, Δg_{NS} and Δg_{NP} account for the nuclear recoil, the nuclear size and the nuclear polarization correction, respectively. The individual calculated contributions to the g-factor of lithiumlike silicon $^{28}Si^{11+}$ are listed in Tab. 2.1 and the dependence of the contributions on the nuclear charge Z can be seen in Fig. 2.4.
In order to calculate these contributions several series expansion have to be evaluated, which

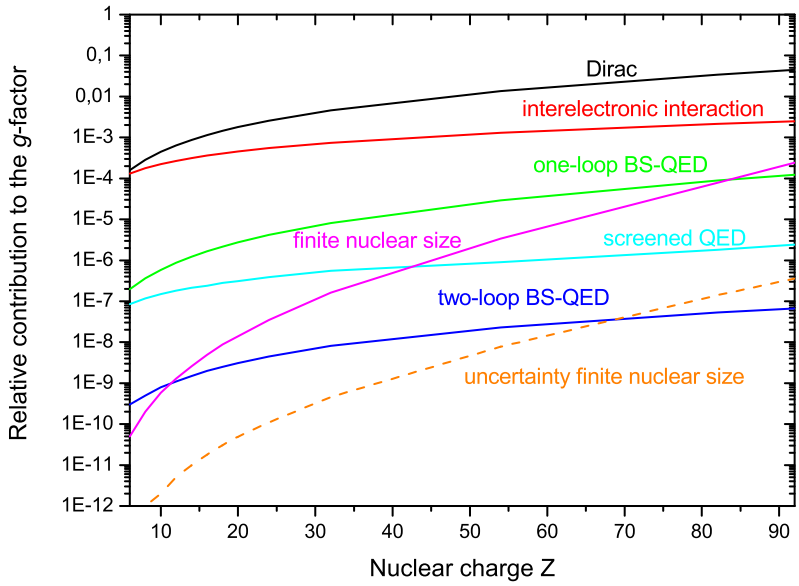

Figure 2.4: Relative theoretical contributions to the g-factor of the $2s$ electron bound in lithiumlike ions as a function of the nuclear charge.

can be arranged in orders of $(1/Z)$:

$$\begin{aligned} g_{(1s)^2 2s_{1/2}} &= g_{\mathrm{D}} \\ &+ \left(\frac{1}{Z}\right)^0 \left[D_0^1 \cdot \left(\frac{\alpha}{\pi}\right) + D_0^2 \cdot \left(\frac{\alpha}{\pi}\right)^2 + \ldots + \left(\frac{1}{M}\right)\left[R_0^0 + R_0^1 \cdot \left(\frac{\alpha}{\pi}\right) + \ldots\right]\right] \\ &+ \left(\frac{1}{Z}\right)^1 \left[D_1^0 + D_1^1 \cdot \left(\frac{\alpha}{\pi}\right) + D_1^2 \cdot \left(\frac{\alpha}{\pi}\right)^2 + \ldots + \left(\frac{1}{M}\right)\left[R_1^0 + R_1^1 \cdot \left(\frac{\alpha}{\pi}\right) + \ldots\right]\right] \\ &+ \left(\frac{1}{Z}\right)^2 \left[D_2^0 + D_2^1 \cdot \left(\frac{\alpha}{\pi}\right) + D_2^2 \cdot \left(\frac{\alpha}{\pi}\right)^2 + \ldots + \left(\frac{1}{M}\right)\left[R_2^0 + R_2^1 \cdot \left(\frac{\alpha}{\pi}\right) + \ldots\right]\right] \\ &+ \ldots + g_{\mathrm{NS}} + g_{\mathrm{NP}}. \end{aligned} \tag{2.9}$$

If the coefficients have not been calculated to all orders of $Z\alpha$ there is an additional series expansion in $Z\alpha$, which is not shown for the sake of clarity. The coefficients can be assigned to the appropriate contributions from Eq. (2.8) as follows:

- D_i^0 account for the interelectronic interaction,
- D_0^j correspond to the one-electron QED corrections,
- D_i^j for $i, j \geq 1$ are related to the screened QED correction,

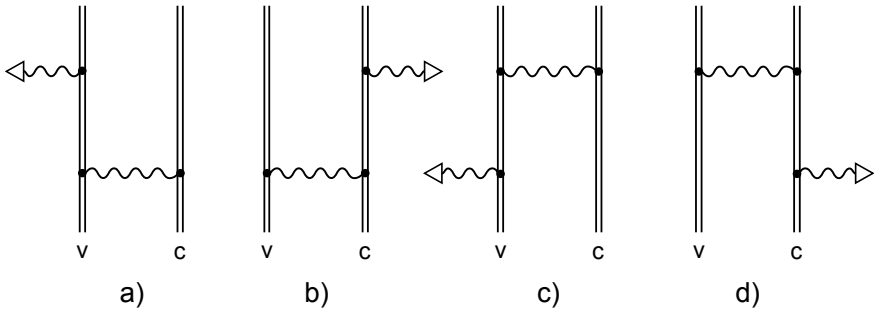

Figure 2.5: Feynman diagrams for the $(1/Z)$-term of the interelectronic interaction. Here v and c denote the valence and the core electron, respectively [17].

- R_i^j belong to the recoil corrections. Here, R_0^0 is denoted as one-electron recoil, R_1^0 as radiative recoil and R_i^0 for $i \geq 1$ as two-electron recoil correction.

The Dirac value

To the lowest order, the g-factor of a lithiumlike ion can be calculated, similar as for the hydrogenlike ion (compare Eq. (2.6)), by solving the Dirac equation for the electron bound to a nucleus within an external magnetic field. However, considering now a three-electron ion, it has to be evaluated for the $2s$-state and then yields:

$$g_{\mathrm{D}} = \frac{2}{3}\left[1 + \sqrt{2 + 2\sqrt{1-(Z\alpha)^2}}\right]. \tag{2.10}$$

The interelectronic interaction

The one-photon exchange correction, shown in Fig. 2.5, was calculated by Shabaev *et al.* within the framework of QED and by employing the Fermi Model for the nuclear charge distribution [17]. The difference between this result and the one for a pointlike nucleus is considered as the uncertainty. In 2004 Glazov *et al.* performed the calculation of order $1/Z^2$ and higher with the large-scale configuration-interaction Dirac-Fock-Sturm method [42]. This method is used to approximately calculate the electron-electron interaction in all orders in $(1/Z)$ and thus yields $D_1^0 + D_2^0 + D_3^0 + ...$ It also accounts for the negative-energy-spectrum contribution, which cannot be neglected in the case of the g-factor, by including the magnetic potential in the Dirac equation and thus breaking the symmetry of the Coulomb potential. Since the one-photon exchange term is already calculated within QED, the D_1^0-contribution is separated and replaced by the QED-result. Very recently the two-photon exchange term (of order $1/Z^2$) has also been evaluated within the framework of QED [43], but was published so far only for the hyperfine splitting [44].

The QED correction

To zeroth order in $1/Z$, the one-electron QED correction, similar as for the hydrogenlike ion, has to be performed for the $2s$-state. The self-energy correction has been calculated for the $2s$-state to all orders in αZ in [45] and the vacuum-polarization correction has been evaluated in [42, 46], both together constituting the one-loop QED-correction. The higher order terms have not been evaluated to all orders in $(Z\alpha)$ yet. In [32] the second-order correction has been calculated up to order $(Z\alpha)^4$, whereas the third-order calculation has only been calculated to $(Z\alpha)^2$. Nevertheless, presently for the g-factor of lithiumlike silicon the higher order terms can be neglected without affecting the accuracy, which is limited by the screened QED corrections.

The screened QED

The screened QED covers the influence of the interelectronic interaction on the QED effects and its calculation constitutes, besides the interelectronic interaction, one of the main challenges for the theoreticians. Since the rigorous evaluation within the framework of QED has not been accomplished neither to all orders nor for all elements, there are approaches treating either the QED-contribution or the interelectronic interaction just approximately:

1. The electron-electron interaction is calculated rigorously whereas the QED calculation is performed perturbatively. It has been calculated to order $(Z\alpha)^2/Z$ in [42]. Higher order terms in $(1/Z)$, being especially relevant in the low-Z-region, are extracted from Yan *et al.* [47], where the interelectronic interaction is considered to all orders in $(1/Z)$ but nonrelativistic wave functions are employed.

2. The QED correction is on the one hand calculated within an effective screening potential, which partly includes the interaction between the valence electron and the core electrons, and on the other hand within the binding potential of the nucleus [48]. The difference between both values yields the screening correction. Due to the incomplete description of the electron-electron interaction within the effective screening potential the uncertainty is limited and was found to be higher than the uncertainty of the first approach for $Z \leq 30$.

In 2009 the screened one-loop QED correction (the self-energy and the vacuum-polarization) has been calculated within a rigorous QED approach for $^{208}Pb^{79+}$, decreasing the uncertainty for the g-factor by 10 % [49, 50]. However, this calculation has not been performed for lower Z, yet, and thus for $^{28}Si^{11+}$ the results from the first approach are employed.

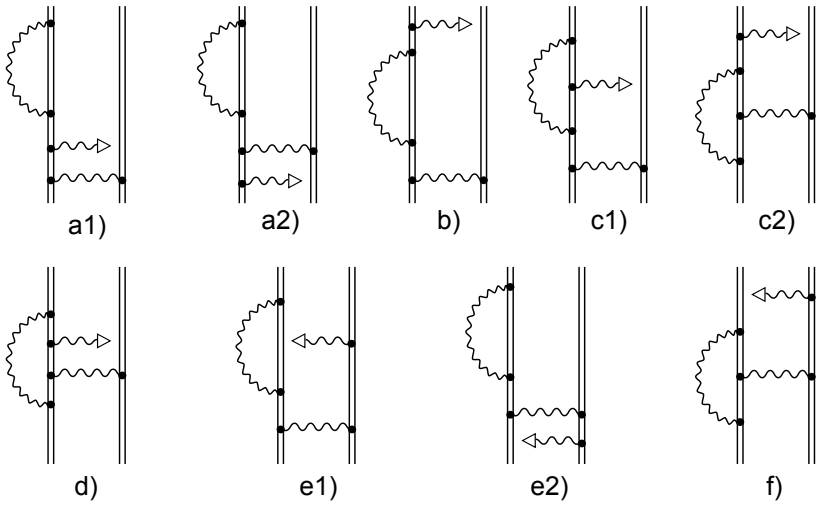

Figure 2.6: Feynman diagrams for the screened self-energy diagrams within an external magnetic field. They account for the interference between the interelectronic interaction and the QED-corrections [50].

The nuclear corrections

To zeroth order in $(1/Z)$ the one-electron nuclear recoil has been calculated in [51] for an arbitrary ns-state to

$$\Delta g_{\mathrm{rec}} = \frac{m_{\mathrm{e}}}{M_{\mathrm{n}}} \frac{(Z\alpha)^2}{n^2}. \tag{2.11}$$

Again the calculations of Yan *et al.* [47, 52] are used to obtain the two-electron recoil contribution by extrapolating his results for the g-factors of lithiumlike ions for $Z \leq 12$. The remaining nuclear recoil contributions have not been calculated for the $2s$-state yet.
For low Z the nuclear size correction was evaluated analytically in [39], whereas a numerical calculation for high Z is performed by considering a Fermi-distributed nuclear charge. Additionally, in the difference between the hydrogen- and the lithiumlike g-factor the nuclear size correction is significantly reduced.
The nuclear polarization correction can be neglected at the present level of accuracy.

2.2 Experimental g-factor

In order to test the calculations performed in the framework of QED, the theoretical prediction has to be compared to reality. Thus, the g-factor has to be determined experimentally with a precision at least comparable to the one of theory. Since frequencies are the physical quantities, which can be measured with the highest precision, it is preferable to trace the g-factor measurement back to frequency measurements. Within an external magnetic field

B one can determine the g-factor by measuring the precession frequency (Larmor frequency ν_L) of the electron spin around the magnetic field:

$$\nu_\mathrm{L} = \frac{1}{2\pi}\frac{g}{2}\frac{e}{m_\mathrm{e}}B. \tag{2.12}$$

Obviously, the magnetic field at the position of the electron has to be known to the same relative precision as aimed for in the g-factor determination. To achieve this precision one takes advantage of the ion where the electron is bound to and measures its cyclotron frequency

$$\nu_\mathrm{c} = \frac{1}{2\pi}\frac{q}{m}B, \tag{2.13}$$

where q and m are the charge and the mass of the ion, respectively. Combining Eq. (2.12) and (2.13) reveals that the magnetic field cancels and the g-factor can be determined by measuring the frequency ratio $\Gamma \equiv \nu_L/\nu_c$:

$$g = 2\frac{\nu_L}{\nu_c}\frac{q}{e}\frac{m_\mathrm{e}}{m} = 2\cdot\Gamma\frac{q}{e}\frac{m_\mathrm{e}}{m}. \tag{2.14}$$

Both frequencies are measured simultaneously in order to minimize shifts due to a drift of the magnetic field. Another advantage that arises from the simultaneous measurement is that the g-factor measurement can be interrupted and continued at any time, enabling a break of the measurement without loosing data.

The free cyclotron frequency of the ion can be determined by measuring the eigenfrequencies of the ion stored in a Penning trap, which will be discussed in the next chapter. The Larmor frequency, however, is not related to an oscillating charge and cannot be measured directly. Thus another technique has to be applied. Therefore, microwaves at the expected Larmor frequency are irradiated into the trap to induce a transition between the two spin states. In order to detect the spin orientation the continuous Stern-Gerlach effect [23] is employed. A magnetic inhomogeneity is induced to couple the spin orientation to the axial eigenmode of the ion. Within this magnetic inhomogeneity a precise measurement of the eigenfrequencies and thus the free cyclotron frequency is impossible. To account for this, the double-Penning trap technique has been implemented, spatially separating the high-precision measurement of the frequency ratio from the spin state detection [53]. The two traps which are used in our experiment are

- the precision trap (PT) with a very homogeneous magnetic field where the actual g-factor measurement takes place by measuring the free cyclotron frequency while simultaneously irradiating microwaves to change the spin state.

- the analysis trap (AT) with an inhomogeneous magnetic field, which is exclusively used to determine the spin orientation.

In the following chapters the measurement techniques for the Larmor and free cyclotron frequency are described in detail and the experimental setup as well as the measurement cycle of a g-factor measurement are presented.

Chapter 3

Trapping ions

In order to determine the g-factor of the electron bound in a highly-charged ion with an uncertainty of the order of 10^{-9} or better, the ion has to be observed for long times without any external disturbance. Moreover, it is absolutely mandatory that the measurement is performed with a single ion, since any interaction with other particles would disturb the measurement and thus preclude high-precision.
A Penning trap is a perfectly suited and well-understood tool to store a single ion for almost arbitrary long time and to manipulate the ion in a controlled manner. The motional frequencies of the ion inside the trap can be measured non-destructively to a high precision. Applying the continuous Stern-Gerlach effect even the spin state of the electron can be detected with almost 100 % reliability. The principle of a Penning trap is presented in this chapter whereas the techniques to measure the frequencies and the spin state are addressed in the next chapter.

3.1 The Penning trap

Within a strong magnetic field B_0 the ion with charge-to-mass ratio q/m is forced on a circular path around the magnetic field lines and oscillates with the free cyclotron frequency

$$\nu_\mathrm{c} = \frac{1}{2\pi}\frac{q}{m}B_0. \tag{3.1}$$

Without loss of generality the magnetic field is aligned along the $\hat{z}$-axis

$$\boldsymbol{B} = B_0 \cdot \hat{\mathbf{e}}_z. \tag{3.2}$$

Accordingly, the ion is confined in the plane perpendicular to the magnetic field. In order to achieve a storage within the third direction in space, the $\hat{z}$-direction, a static electric field is applied. This superposition of a strong magnetic and a weak electric field is called a Penning trap [54].

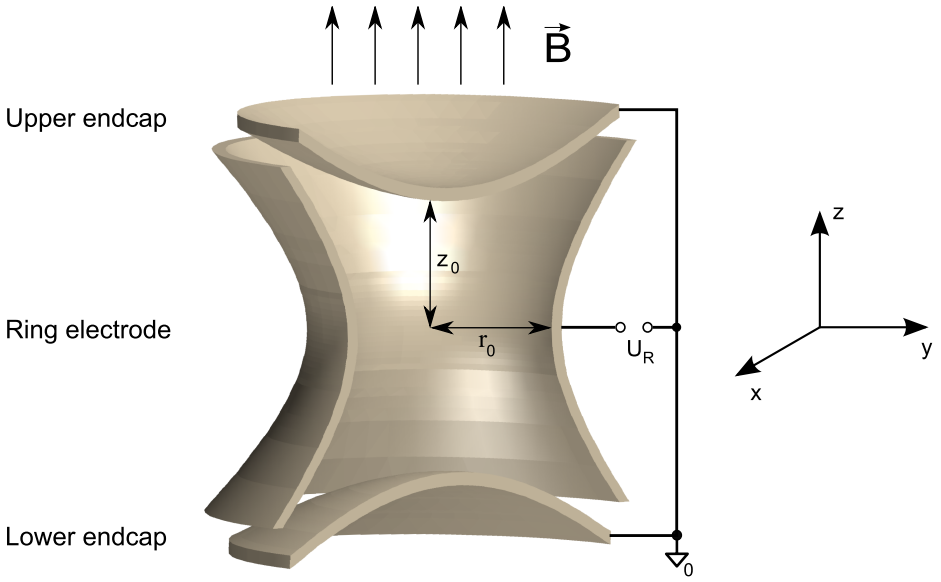

Figure 3.1: Cross section of a hyperbolic Penning trap with a ring electrode and two endcap electrodes. Radial confinement of a charged particle is achieved by a magnetic field $\boldsymbol{B}$ along the $\hat{z}$-axis, whereas the voltage U_R applied between ring and endcap electrodes provides the axial confinement. The trap geometry is characterized by the radius r_0 of the ring electrode and the distance $2z_0$ between the two endcaps. Ideally the electrodes would have an infinite length to create a perfect quadrupole potential.

3.1.1 The ideal Penning trap

To obtain a harmonic motion of the ion, with an oscillation frequency independent from the motional amplitude, an electric quadrupole potential is used for the axial confinement

$$\Phi(r) = \frac{U_R}{2d^2}\left(\frac{r_0^2}{2} - z^2\right). \tag{3.3}$$

Here U_R is the voltage applied to the electrodes and d is a characteristical trap parameter. A configuration to create this potential are electrodes whose surfaces form equipotential lines of the potential. Such a hyperbolic Penning trap with the characteristic trap parameter

$$d = \sqrt{\frac{1}{2}\left(\frac{r_0^2}{2} + z_0^2\right)} \tag{3.4}$$

is shown in Fig. 3.1. The electric field results in an uncoupled harmonic oscillation along the magnetic field lines with the axial frequency

$$\omega_z = \sqrt{\frac{qU_R}{md^2}}. \tag{3.5}$$

Furthermore, it influences the radial motion of the ion by slightly modifying the free cyclotron frequency (Eq. (3.1)) and superimposing a slow drift frequency around the trap

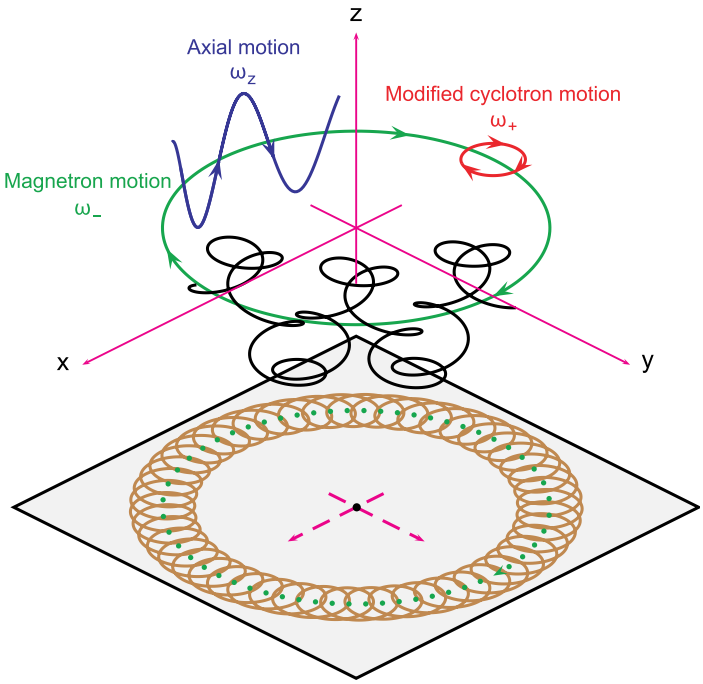

Figure 3.2: The three eigenmotions of a charged particle stored in a Penning trap and the resulting superposition (black) [55]. The amplitudes of the particular motions are arbitrarily chosen.

centre. Solving the equations of motions [54]

$$\begin{aligned} \ddot{x} - \omega_c \dot{y} - \frac{1}{2}\omega_z^2 x = 0 \\ \ddot{y} + \omega_c \dot{x} - \frac{1}{2}\omega_z^2 y = 0 \\ \ddot{z} + \omega_z^2 z = 0 \end{aligned} \tag{3.6}$$

yields for the radial motions the modified cyclotron frequency ω_+ and the magnetron frequency ω_-

$$\begin{aligned} \omega_+ &= \frac{\omega_c}{2} + \sqrt{\frac{\omega_c^2}{4} - \frac{\omega_z^2}{2}} \\ \omega_- &= \frac{\omega_c}{2} - \sqrt{\frac{\omega_c^2}{4} - \frac{\omega_z^2}{2}}. \end{aligned} \tag{3.7}$$

A graphical presentation of the three eigenmotions is shown in Fig. 3.2. For a strong magnetic and a comparably weak electric field the eigenfrequencies usually obey the hierarchy

$$\omega_c > \omega_+ \gg \omega_z \gg \omega_-. \tag{3.8}$$

The experimental frequencies for a lithiumlike silicon $^{28}Si^{11+}$ stored in our two measurement

	analysis trap			**precision trap**		
	ν (Hz)	T (K)	A (µm)	ν (Hz)	T (K)	A (µm)
ν_-	3 771	0.08	3.8	10 396	0.064	2.0
ν_z	411 780	2.5	14.9	687 335	4.2	11.6
ν_+	22 392 580	54.4	1.3	22 721 951	138.8	2.0
ν_c	22 396 366			22 732 347		

Table 3.1: Eigenfrequencies of a $^{28}Si^{11+}$-ion for a ring voltage of -8.5 V in the precision trap and -3.1 V in the analysis trap as well as typical temperatures T and the corresponding oscillation amplitudes A are listed.

traps of 7 mm inner diameter are listed in Tab. 3.1.
The radicands within the equations for the eigenfrequencies reveal that for stable trapping conditions two requirements have to be fulfilled:

$$qU_R > 0 \qquad \text{and} \qquad \omega_c \geq \sqrt{2}\omega_z. \tag{3.9}$$

The first one simply reflects the need of a suitably adjusted polarity of the electric trapping potential for the stored charge whereas the second condition describes the point where the repulsive force in the radial plane due to the electric field exceeds the confinement strength of the magnetic field.
In an ideal Penning trap the eigenfrequencies are linked among each other

$$\omega_+ \cdot \omega_- = \frac{\omega_z^2}{2}. \tag{3.10}$$

Of much greater interest, however, is the correlation between the eigenfrequencies and the free cyclotron frequency, being the actual frequency of interest, by the following relations

$$\begin{aligned} \omega_c &= \omega_+ + \omega_- \\ \omega_c^2 &= \omega_+^2 + \omega_z^2 + \omega_-^2. \end{aligned} \tag{3.11}$$

Whereas the first equation only holds for an ideal Penning trap, the second relation, the so-called "invariance theorem", remains valid for imperfections concerning the alignment between the trap and the magnetic field axis and an ellipticity[1] of the trapping potential due to defects on the electrode surface for example [56, 57]. Because of the typical hierarchy of the frequencies (see Eq. 3.8) the resulting uncertainty of ω_c is mainly dominated by the

[1] Ellipticity denotes an imperfection of the rotational symmetry.

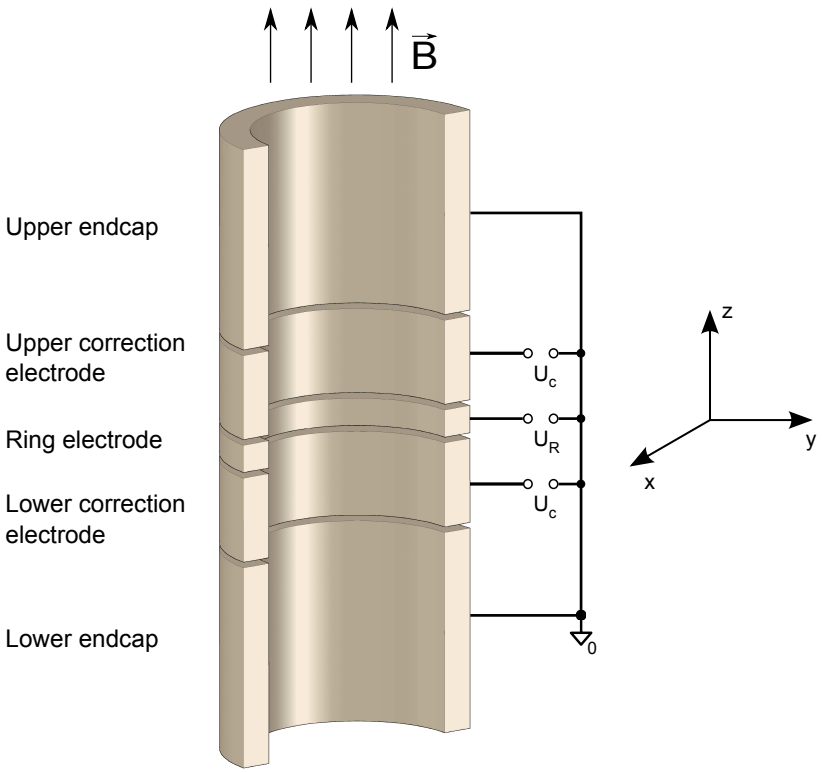

Figure 3.3: Cross section of a simplified five-electrode cylindrical Penning trap. The additional correction electrodes are used to tune the potential at the trap centre to a high harmonicity.

uncertainty of ω_+:

$$\Delta\omega_c = \sqrt{\left(\frac{\omega_+}{\omega_c}\Delta\omega_+\right)^2 + \left(\frac{\omega_z}{\omega_c}\Delta\omega_z\right)^2 + \left(\frac{\omega_-}{\omega_c}\Delta\omega_-\right)^2}, \tag{3.12}$$

implying that the modified cyclotron frequency has to be measured to the highest precision of all eigenfrequencies.

3.1.2 The real cylindrical Penning trap

In reality it is not possible to achieve perfectly homogeneous magnetic fields or purely harmonic electric fields but deviations from the ideal configuration have to be considered and well understood. The hyperbolically shaped electrodes allow for a good approximation of the ideal Penning trap. However, already there, imperfections e.g. due to machining precision, finite size of the experiment, assembling and aligning problems or patch potentials on the electrode surfaces have to be considered. In addition, the magnetic field is never perfectly homogeneous, although the superconducting magnets already provide a very high

homogeneity, and any ferromagnetic material implemented within or close to the trap generates further disturbances of the magnetic field.
Furthermore, hyperbolic electrodes are difficult to manufacture and if ion transport between different traps or any external radiation is required the symmetry has to be broken by drilling holes in the endcap electrodes. These disadvantages can be overcome by a cylindrical Penning trap [58], like the configuration shown in Fig. 3.3, which is used in our experiment (for details of our setup see chapter 5). By introducing two additional electrodes, the correction electrodes, the electric quadrupole potential can be well approximated for a small volume around the trap centre. The ratio between the voltage applied to the ring U_{R} and the voltage applied to the correction electrodes U_{c} is denoted as *tuning ratio TR*

$$TR = \frac{U_{\mathrm{R}}}{U_{\mathrm{c}}}. \tag{3.13}$$

In order to describe the non-harmonic contributions, the electric potential of a real Penning trap can be written as a series expansion [58]

$$\Phi(r,\theta) = \frac{U_R}{2}\sum_{k=1}^{\infty} C_k r^k P_k(\cos\theta) \tag{3.14}$$

where $P_k(\cos\theta)$ are the Legendre polynomials and C_k are the expansion coefficients. In order to obtain an ideal quadrupole potential it is required to achieve $C_2 = 1$ and $C_k = 0$ for $k \neq 2$. The odd coefficients vanish for a mirror symmetric configuration across the $z = 0$ plane. In reality the mirror symmetry is not perfectly fulfilled, due to split correction electrodes or patch potentials on the electrode surfaces for instance, but the odd coefficients are quite small. The influence of the particular coefficients on the ion are the following:

- The C_0-coefficient does not have any influence on the ion.
- C_1 results in a constant force on the ion and thus just shifts the equilibrium position of the oscillation. This is used in the experiment to control and manipulate the position of the ion inside the trap by applying asymmetric voltages to the electrodes and thus deliberately introducing a C_1-term. However, usually the potential is expanded around the equilibrium position of the ion, which means that $C_1 \equiv 0$.
- The C_2-term is responsible for the harmonic confinement. Due to the presence of other coefficients Eq. (3.5) is slightly modified to

$$\omega_z = \sqrt{C_2 \frac{qU_R}{m}}. \tag{3.15}$$

- The higher-order odd terms C_3, C_5, ... can be usually neglected due to the mirror symmetry.

- $C_4 \neq 0$ corresponds to a dependence of the ions' frequency on its motional amplitude, which is highly unwanted. Fortunately the C_4-term can be minimized by adjusting the tuning ratio, which is described in chapter 7.5.1.

- The C_6-coefficient as well as the other higher even order terms also result in an energy-dependent shift of the oscillating frequency but become less important due to the typical particle amplitudes, which are small compared to the trap dimensions. C_6 can be eliminated by an appropriate choice of the trap geometry and the higher order terms can be neglected for the usual motional amplitudes of the ion.

Optimization of the electric trapping potential

Besides the rotational and the mirror symmetry of the trap, which suppress the influence of the odd coefficients, additional measures can be taken to optimize the electric potential:

- An adequately chosen trap geometry enables the simultaneous elimination of the C_4- and the C_6-coefficient. This is denoted as a *compensated trap*.

- Changing the voltage of the correction electrodes to eliminate the C_4-term implies a change of the C_2-term as well and thus alters the axial frequency. Although this provides no limitation for the achievable precision it complicates the experimental work of the trap optimization process. Therefore, it is useful to make the axial frequency independent from the tuning ratio. This again can be achieved by choosing a suited ratio between the lengths of correction and ring electrodes and results in an *orthogonal trap* configuration.

A detailed description of the design of an orthogonal and compensated cylindrical Penning trap can be found in [58, 59].

Frequency shifts due to the anharmonic electric field

For a non-vanishing C_4-coefficient the resulting dependence of the eigenfrequencies and (for completeness) of the Larmor frequency on the energy E in the particular modes can be expressed in a matrix form [54]:

$$\begin{pmatrix} \Delta\omega_+/\omega_+ \\ \Delta\omega_z/\omega_z \\ \Delta\omega_-/\omega_- \\ \Delta\omega_L/\omega_L \end{pmatrix} = \frac{6C_4}{qU_R C_2^2} \begin{pmatrix} \frac{1}{4}(\omega_z/\omega_+)^4 & -\frac{1}{2}(\omega_z/\omega_+)^2 & -(\omega_z/\omega_+)^2 \\ -\frac{1}{2}(\omega_z/\omega_+)^2 & \frac{1}{4} & 1 \\ -(\omega_z/\omega_+)^2 & 1 & 1 \\ 0 & 0 & 0 \end{pmatrix} \cdot \begin{pmatrix} E_+ \\ E_z \\ E_- \end{pmatrix}. \quad (3.16)$$

Since at least the axial energy is not constant but thermally distributed due to its connection to the detection system, a non-vanishing C_4-coefficients leads to a broadened axial signal

and thus decreases the achievable precision and accuracy. Therefore it is highly desirable to eliminate the C_4-term, which can be done experimentally and is described in chapter 7.5.1.

Frequency shifts due to the inhomogeneous magnetic field

The magnetic field in reality is not perfectly homogeneous as assumed in the case of the ideal Penning trap, but inhomogeneities due to the superconducting magnet itself or ferromagnetic materials implemented in the setup have to be considered. They again result in energy-dependent frequency shifts. In our experiment we even deliberately introduce a magnetic inhomogeneity in one of our two measurement traps to detect the spin direction [60]. A ferromagnetic ring electrode is used to produce *a magnetic bottle* (see Fig. 4.5) of the form

$$\Delta B_z = B_2 \left(z^2 - \frac{r^2}{2} \right). \tag{3.17}$$

Accordingly, we have a strong (required) inhomogeneity in one trap, but even in the second trap, about 4 cm apart, the main inhomogeneity is caused by the tail of this magnetic bottle, although already strongly suppressed. Within such a magnetic inhomogeneity the frequencies of the ion depend on the energy of the particular oscillation modes [54]:

$$\begin{pmatrix} \Delta\omega_+/\omega_+ \\ \Delta\omega_z/\omega_z \\ \Delta\omega_-/\omega_- \\ \Delta\omega_L/\omega_L \end{pmatrix} = \frac{B_2}{B_0}\frac{1}{m\omega_z^2} \begin{pmatrix} -(\omega_z/\omega_+)^2 & 1 & 2 \\ 1 & 0 & -1 \\ 2 & -1 & -2 \\ -(\omega_z/\omega_+)^2 & 1 & 2 \end{pmatrix} \cdot \begin{pmatrix} E_+ \\ E_z \\ E_- \end{pmatrix}, \tag{3.18}$$

which prevents any high-precision measurement and motivates the spatial separation of the spin state detection and the measurement of the frequency ratio Γ.
On the other hand a precise knowledge of B_2 allows for a determination of the radial energies

$$\frac{\Delta\omega_z}{\omega_z} = \frac{B_2}{B_0}\frac{1}{m\omega_z^2}(E_+ - E_-) \tag{3.19}$$

by measuring the axial frequency shift.

Relativistic corrections

Until now the motion of the ion has been treated in the non-relativistic regime. Additional relativistic corrections have been calculated in [54] to

$$\begin{pmatrix} \Delta\omega_+/\omega_+ \\ \Delta\omega_z/\omega_z \\ \Delta\omega_-/\omega_- \\ \Delta\omega_L/\omega_L \end{pmatrix} = -\frac{1}{mc^2} \begin{pmatrix} 1 & \frac{1}{2} & -(\omega_z/\omega_+)^2 \\ \frac{1}{2} & \frac{3}{8} & -\frac{1}{4}(\omega_z/\omega_+)^2 \\ -(\omega_z/\omega_+)^2 & -\frac{1}{4}(\omega_z/\omega_+)^2 & \frac{1}{4}(\omega_z/\omega_+)^4 \\ \frac{2}{9} & \frac{1}{2} & -(\omega_z/\omega_+)^2 \end{pmatrix} \cdot \begin{pmatrix} E_+ \\ E_z \\ E_- \end{pmatrix}. \tag{3.20}$$

For typical ion temperatures during this experiment (see Tab. 3.1) the maximum resulting relative frequency shifts are of the order of 10^{-13} and can thus be neglected at the precision achieved in the measurement presented in this thesis.

Chapter 4

Frequency measurements

The g-factor measurement is performed on a single ion whose eigenfrequencies have to be measured non-destructively to a high precision. This is achieved by electronically detecting the image-charges, which are induced in the electrodes by the oscillating ion. Since it is very challenging to detect the current of a single ion, which is only of the order of fA, a highly sensitive detection system has to be employed.
As already mentioned, two spatially separated traps are required for the g-factor measurement: one for the detection of the spin orientation (analysis trap or in short AT) and one for the high-precision measurement of the frequency ratio Γ (precision trap or PT). Due to the different purposes of these traps and the resulting different conditions, the requirements concerning the detection of the oscillation frequencies vary. Therefore, in most cases different techniques for the frequency measurements are applied in the two traps. All these techniques are based on the measurement of the axial frequency, since both the radial modes and the spin orientation can be coupled to the axial mode. This means, that all eigenfrequencies as well as the spin state can be determined with a single axial detection system for each trap.
In the first section of this chapter the basic principles of the ion detection are presented whereas the following sections deal with the experimental realization and the different detection techniques, which have been applied in this thesis.

4.1 Image-current detection technique

The double-trap method requires a non-destructive measurement technique since after the measurement of the ion's eigenfrequencies in the PT the same ion has to be transported to the AT to determine the spin orientation. All measurement techniques used in this experiment are based on the interaction of the ion with an impedance connected to the trap electrodes. The oscillating ion induces mirror charges within the electrodes resulting in a

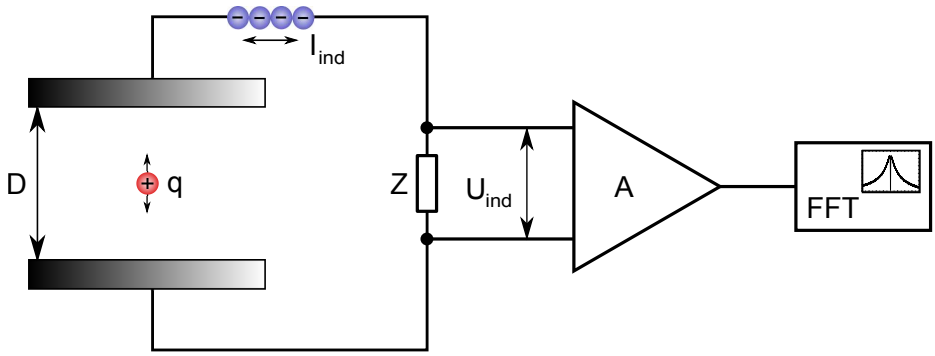

Figure 4.1: Basic principle of the non-destructive ion detection technique: The oscillating ion with charge q induces mirror charges in the trap electrodes, which are separated by the distance D. The resulting current I_{ind} creates a voltage drop U_{ind} across the impedance Z, which is amplified and then analysed with a fast Fourier transformation (FFT).

very tiny current across the impedance, which transforms the current into a voltage drop. This voltage drop is amplified by a custom-build amplifier, which is placed as close to the trap as possible to avoid additional parasitic capacitance. Afterwards the signal is analysed with a fast Fourier transformation (FFT) to obtain the frequency information (see Fig. 4.1). In the following the details of this detection scheme are described for the axial motion.
The current induced by the ion with charge q amounts to

$$I_{\mathrm{ind}} = \frac{dq}{dt} = \frac{q}{D}\dot{z}. \tag{4.1}$$

Here D denotes the *effective electrode distance*, which is the distance of two infinitely large parallel plates where the ion would induce the same electric field as it does in the real electrode configuration. Accordingly, D depends on the trap geometry as well as on the electrodes used for the detection. The effective electrode distance can be simulated as described in [61] and yields

$$D = 7.38\,\mathrm{mm} \tag{4.2}$$

for the precision trap with the detection system connected to the correction electrode (compare Fig. 4.8).
The induced current of a single ion is only of the order of fA. Accordingly, a very high impedance Z has to be employed to transfer this tiny current into a measurable voltage drop

$$U_{\mathrm{ind}} = I_{\mathrm{ind}} \cdot Z = \frac{q}{D} Z \cdot \dot{z}. \tag{4.3}$$

An adequately high impedance can be achieved by a tank circuit, which is tuned to the resonance frequency of the ion. Therefore, an inductance L is connected in parallel to the trap and forms together with the unavoidable capacitance C, arising from the trap, the

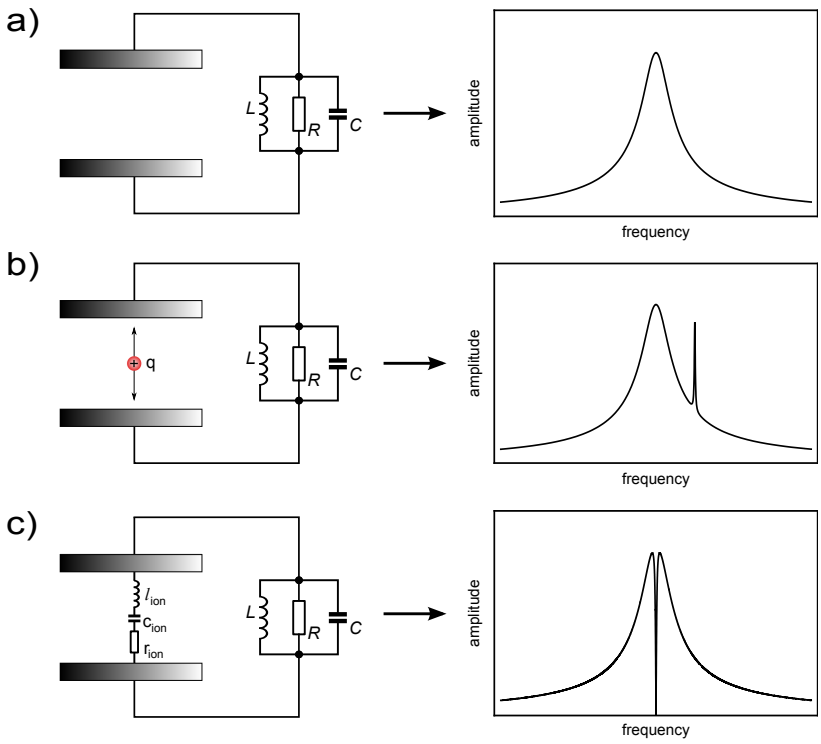

Figure 4.2: Simulated noise resonance of the tank circuit without an ion in the trap (a). An excited ion stored in the trap dissipates power and appears as a peak (b). The ions' oscillation frequency is detuned from the resonance frequency of the detection system. A stored ion in thermal equilibrium with the detection system can be considered as a series resonance circuit with capacitance c_{ion}, inductance l_{ion} and resistance r_{ion}. It shorts the noise of the resonator at its oscillation frequency and thus appears as a dip in the noise spectrum (c).

cabling, the amplifier and the inductance itself, a tank circuit with the impedance

$$Z = \left(\frac{1}{i\omega L} + i\omega C + \frac{1}{R} \right)^{-1}. \tag{4.4}$$

On resonance the capacitance is compensated by the inductance yielding an effective resistance of

$$R = Q\omega_0 L, \tag{4.5}$$

where ω_0 is the resonance frequency of the tank circuit

$$\omega_0 = \frac{1}{\sqrt{L\,C}}, \tag{4.6}$$

and Q is its quality factor. The quality factor describes the energy loss per oscillation cycle and is given by

$$Q = \frac{\omega_0 L}{R_{\mathrm{L}}}. \tag{4.7}$$

R_{L} summarizes loss mechanisms of the system and has to be minimized to achieve a high quality factor. To this end superconducting materials, as niobium titanium (NbTi), are used for the wire and the housing of the inductance.
The thermal noise amplitude of this tank circuit

$$u_{r,eff} = \sqrt{4k_{\mathrm{B}}T \cdot B \cdot \mathrm{Re}(Z)} \tag{4.8}$$

depends on the temperature T, the monitoring bandwidth B and the real part of the impedance Z. k_{B} is the Boltzmann constant. Calculating the real part of Z and inserting it into Eq. (4.8) gives the thermal noise resonance of the tank circuit as shown in Fig. 4.2a).

4.1.1 Peak detection and resistive cooling

If the axial temperature of the ion inside the trap is sufficiently excited to overcome the thermal noise of the resonator a peak can be detected at the resonance frequency of the ion (see Fig. 4.2b). Simultaneously, electric power according to $P = I^2_{\mathrm{ind,rms}} \cdot R$ is dissipated by the resistance of the tank circuit and results in an exponential decrease of the motional energy of the ion. Thus, the ion is resistively cooled with a cooling time constant

$$\tau = \frac{D^2}{R} \cdot \frac{m}{q^2} \tag{4.9}$$

until it reaches thermal equilibrium with the tank circuit. Since the tank circuit is cooled to liquid helium temperature the axial temperature, in the absence of any heating mechanism, is $T_{\mathrm{z}} = 4.2\,\mathrm{K}$. However, by application of electronic feedback, which is described in section 4.2.4, the quality factor can be changed leading to an effective change of the temperature of the resonator and thus of the ion.

4.1.2 Dip detection

Once the ion is in thermal equilibrium the signature of the ion within the frequency spectrum changes entirely. This can be understood from the equation of motion for the ion interacting with the detection system. Due to the voltage drop across the impedance of the tank circuit the ion experiences an additional force

$$F = \frac{q}{D} U_{\mathrm{ind}} = \frac{q}{D} I_{\mathrm{ind}} Z, \tag{4.10}$$

which adds to the force of the electric trapping potential (see Eq. 3.6):

$$\ddot{z} + \omega_{\mathrm{z}}^2 z + \frac{q}{mD} I_{\mathrm{ind}} Z = 0. \tag{4.11}$$

With Eq. (4.1) the space coordinate z can be expressed in terms of the induced current. After rearranging the coefficients, one obtains

$$\frac{D^2}{q^2} m \cdot \dot{I}_{\mathrm{ind}} + Z \cdot I_{\mathrm{ind}} + \frac{D^2}{q^2} m \omega_{\mathrm{z}}^2 \int I_{\mathrm{ind}} dt = 0. \tag{4.12}$$

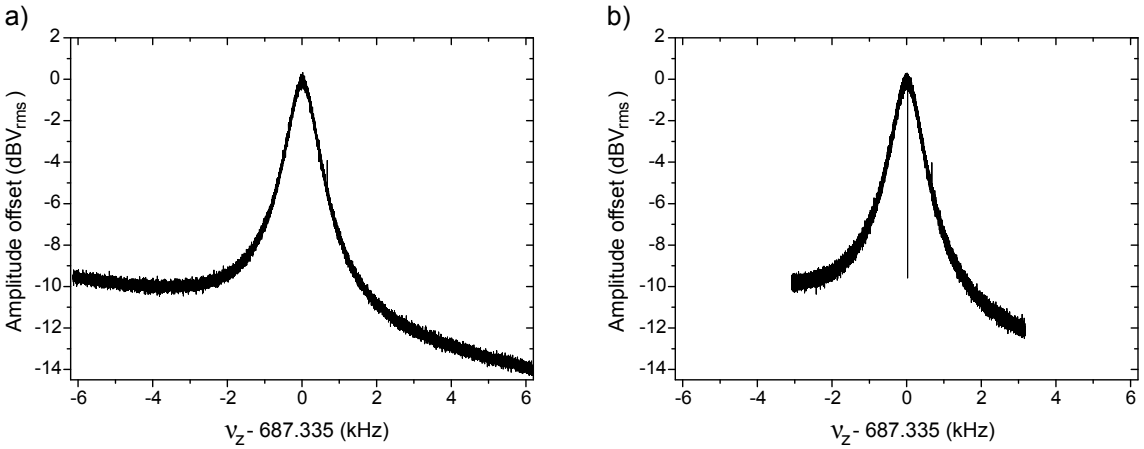

Figure 4.3: The axial resonator for the PT without (a) and with a stored ion (b) is shown. The linear decreasing noise background arises from the frequency dependence of the detection system.

This relation is equivalent to the differential equation of a series tank circuit when substituting

$$l_{\mathrm{ion}} = \frac{D^2}{q^2} m \qquad c_{\mathrm{ion}} = \frac{q^2}{D^2} \frac{1}{m\omega_{\mathrm{z}}^2} \qquad \text{and} \qquad \omega_{\mathrm{z}} = \frac{1}{\sqrt{l_{\mathrm{ion}} c_{\mathrm{ion}}}}. \tag{4.13}$$

Thus, the ion can be considered as a series tank circuit as shown in Fig. 4.2b). Since there is very little damping of the ion's axial oscillation the resistance at its resonance frequency nearly vanishes. The resulting signal is obtained in a similar way as described for the tank circuit by additionally considering the series tank circuit of the ion when calculating the impedance of the system. At the frequency of the ion a sharp minimum, a so-called "dip", appears, which can be understood as a short cut of the thermal noise of the resonator at the oscillation frequency of the ion. Accordingly, the frequency of the ion can be measured in thermal equilibrium with the tank circuit and thus at low temperatures. This is a highly desirable feature since it minimizes energy-dependent systematic shifts of the eigenfrequencies. The -3 dB-width of the dip

$$\Delta\nu_{\mathrm{z}} = \frac{1}{2\pi} \frac{1}{\tau} = \frac{1}{2\pi} \frac{R}{m} \frac{q^2}{D^2} \tag{4.14}$$

scales with the charge and the mass of the ion and therefore depends on the ion species being detected. Furthermore, when extending the described principle from a single ion to an ion cloud, the dip width is directly proportional to the number of ions n

$$\Delta\nu_{\mathrm{z}}(n) = \frac{n}{2\pi} \frac{R}{m} \frac{q^2}{D^2} \tag{4.15}$$

and can be used to count the number of ions and especially to verify that only a single ion of the detected species is left in the trap.

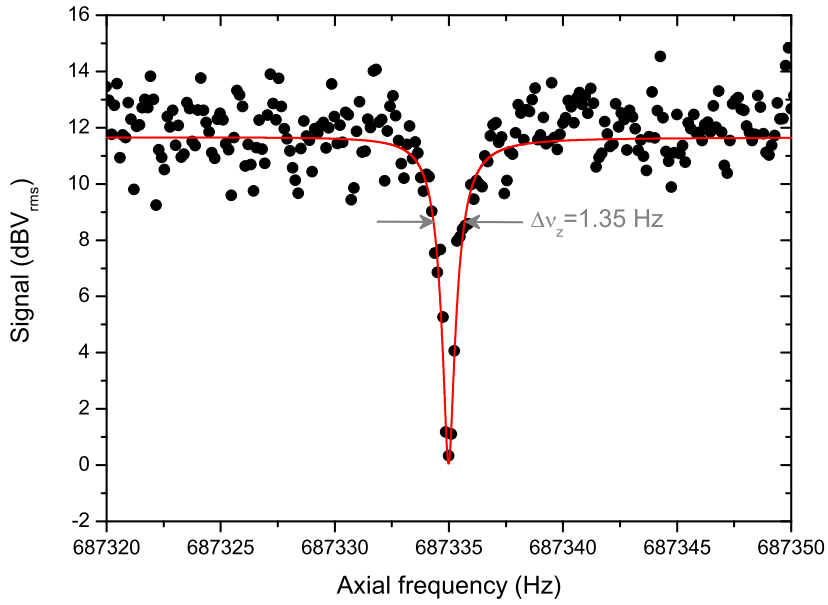

Figure 4.4: The axial frequency of a single $^{28}Si^{11+}$-ion is measured by fitting the data (black dots) with the lineshape given in Eq. (4.16) (red line). For an averaging time of 150 s the resonance center can be determined to 25 mHz [62] at a total frequency of 687 kHz.

4.2 Axial frequency measurement

The axial frequency depends on the trapping voltage and thus can be easily adjusted experimentally. This means that the oscillation frequency of different ion species can be tuned to the resonance frequency of the detection system simply by changing the voltage applied to the ring electrode. Therefore, the axial frequency provides an extremely comfortable access to the measurement of all eigenfrequencies. On this account, the radial modes as well as the orientation of the electron's spin are detected via the axial frequency.

4.2.1 Precision trap - Dip technique

In the precision trap the axial frequency is detected by the dip-technique. However, in reality, the ideal picture, given in Sec. 4.1.2, has to be extended due to the noise contribution of the amplifier u_{amp} and its amplification A as well as a frequency dependence of the detection system κ_{det}, which results in a linear decreasing noise level as can be seen in Fig. 4.3. The frequency information is deduced from a fit of the theoretically expected lineshape [61]:

$$u(\omega) = A \cdot (1 + \kappa_{\mathrm{det}}(\omega - \omega_{\mathrm{R}})) \cdot \sqrt{u_{\mathrm{e}}^2(\omega) + u_{\mathrm{amp}}^2(\omega)} \tag{4.16}$$

to the dip (see Fig. 4.4). Here u_e is the Johnson noise voltage density at the electrode:

$$|u_\mathrm{e}(\omega)| = u_\mathrm{n} \left| \frac{\omega\omega_0(\omega-\omega_\mathrm{z})(\omega+\omega_\mathrm{z})}{\omega\omega_0\omega_\mathrm{z}^2(i-\frac{\omega}{\tau\omega_0^2}) - i\omega^3\omega_0 + Q(\omega-\omega_0)(\omega+\omega_0)(\omega-\omega_\mathrm{z})(\omega+\omega_\mathrm{z})} \right|, \quad (4.17)$$

with u_n being the maximum amplitude on resonance

$$u_\mathrm{n} = \sqrt{4k_\mathrm{B}TR}. \quad (4.18)$$

The second factor in Eq. (4.17) describes the frequency response of a series tank circuit (ion), which is connected in parallel to a parallel tank circuit (resonator). The free fit parameters are the axial frequency ω_z, the dip width τ and the amplification A, while the parameters of the detection system, namely $Q, R, \omega_\mathrm{R}, \kappa_\mathrm{det}$ and u_amp, are determined from an independent fit to the resonance without any ion present.

4.2.2 Analysis trap - Spin state detection

As introduced in Sec. 2.2 the Larmor frequency of the electron is not related to one of the eigenfrequencies of the ion and thus cannot be measured directly. However, it can be determined by probing the transition between the two Zeeman-levels (spin up and spin down), which is done by irradiating microwaves close to the expected Larmor frequency of ∼105 GHz to induce a spin flip. This demands the possibility to detect the spin orientation. To this end, the *continuous Stern-Gerlach effect* [60] is employed: A magnetic inhomogeneity is introduced in the analysis trap by using a ring electrode made of a ferromagnetic material, which is in our case nickel. In second order it results in a quadratic dependence of the magnetic field on the axial coordinate, which adds to the homogeneous magnetic field B_0:

$$B_\mathrm{z} = B_0 + B_2\left(z^2 - \frac{r^2}{2}\right). \quad (4.19)$$

Considering the shape of the resulting magnetic field lines (see Fig. 4.5a) such a configuration is called a *magnetic bottle*. The ion inside this magnetic field gradient experiences an additional force in the axial direction

$$F_\mathrm{z} = -\nabla_\mathrm{z}(\mu \cdot B) = -2\mu_\mathrm{z}B_2 z, \quad (4.20)$$

which depends on the spin momentum

$$\mu_\mathrm{z} = -g\mu_\mathrm{B}S_\mathrm{z}/\hbar \quad (4.21)$$

and therefore on the spin direction. $\mu_\mathrm{B} = e\hbar/(2m_e)$ is the Bohr magneton. The additional contributions to μ_z due to the radial motions are neglected since the radial energies are

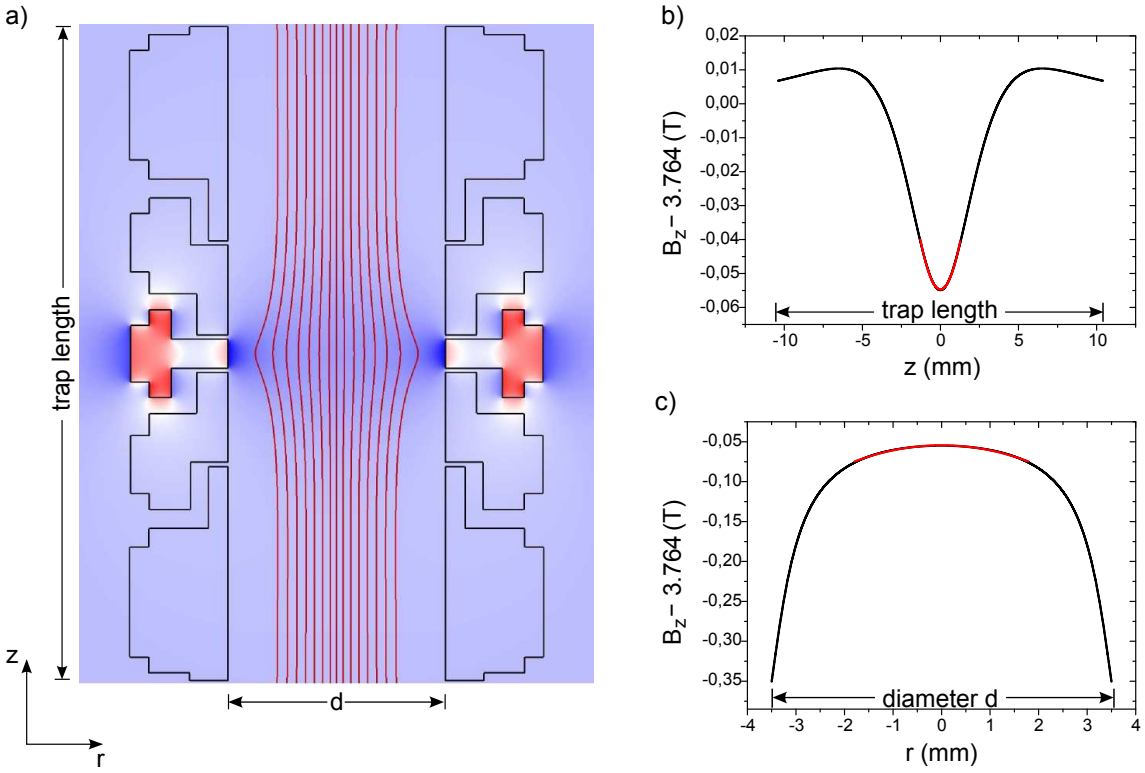

Figure 4.5: Characteristics of the magnetic bottle in the analysis trap. In a) the magnetic field lines for a nickel ring are simulated with COMSOL. To illustrate the bottle-like form of the field lines, the saturation magnetization had to be increased by a factor of 20 compared to the employed nickel-material. b) and c) show a cross-section of the magnetic field in axial and radial direction, respectively, for the correct saturation magnetization of nickel $\mu_0 M = 0.644\,\mathrm{T}$ [63]. The red line indicates the region where a quadratic dependence of the magnetic field on the respective coordinate can be fitted to the data.

considered to be constant. Within a magnetic field there are only two possible orientations for the spin, namely spin up and spin down

$$S_\mathrm{z} = \pm\frac{1}{2}\hbar. \tag{4.22}$$

From the resulting equation of motion

$$\ddot{z} + \left(\omega_{z,0}^2 \pm \frac{g\mu_\mathrm{B}B_2}{m}\right) z = 0 \tag{4.23}$$

it can be seen that the axial frequency in the magnetic bottle slightly depends on the spin orientation

$$\omega_\mathrm{z} = \sqrt{\omega_{\mathrm{z},0}^2 \pm \frac{g\,\mu_\mathrm{B}B_2}{m}} \simeq \omega_{\mathrm{z},0} \pm \frac{g\,\mu_\mathrm{B}B_2}{2m\,\omega_{\mathrm{z},0}}. \tag{4.24}$$

Here $\omega_{z,0}$ is the axial frequency without a magnetic inhomogeneity. Accordingly a change of the spin orientation, a *spin flip*, manifests in a small jump of the axial frequency

$$\Delta\nu_{z,SF} = \frac{g\,\mu_B B_2}{4\pi^2 m\,\nu_{z,0}}, \tag{4.25}$$

whose size mainly depends on the strength of the magnetic bottle B_2 and the mass of the ion m. For the parameters used in our experiment ($B_2 = 10\,\mathrm{mT/mm^2}$, $\nu_{z,0} = 412\,\mathrm{kHz}$, $m = 28\,\mathrm{u}$) the frequency jump for a $^{28}Si^{11+}$-ion amounts to

$$\Delta\nu_{z,SF}(^{28}\mathrm{Si}) = 240\,\mathrm{mHz}. \tag{4.26}$$

To detect such a small frequency jump within a total axial frequency of 412 kHz requires a very high stability of the axial frequency and thus of the trapping voltage. Demanding maximum allowed fluctuations of one quarter of a frequency jump due to a spin flip calls for a voltage stability of

$$\frac{\Delta U_R}{U_R} = 2\frac{\Delta\nu_z}{\nu_z} = 2.5\cdot 10^{-7}. \tag{4.27}$$

This stability can be provided by the high-precision voltage source UM1-14 [64]. However, it was found that the UM1-14 is limited by its supply voltage and therefore a new low-noise voltage supply was developed in [65], which is shortly described in Sec. 5.3.2.

The required frequency stability was one of the main challenges of this experiment (see [66]), since the investigation of the frequency fluctuations and the identification of the responsible source was rather difficult and time-consuming. Finally a series of experimental improvements led to success:

- the implementation of cryogenic switches to short the excitation lines and thus eliminate noise sources [61],
- a new design of the reflector electrode to keep the measurement traps clean from ions during the charge-breeding process and thus prevent charging of the electrodes (Sec. 5.2.1),
- new trap electrodes were manufactured where great care has been taken to achieve extremely smooth surfaces (Sec. 5.2.3),
- the implementation of a phase-sensitive detection technique (Sec. 4.2.3).

Although a spin flip can be detected by measuring the axial frequency with the dip-technique, a phase-sensitive detection technique enables a faster measurement with an increased resolution. As can be seen in the following section, the achieved frequency stability is very high and allows for an unambiguous detection of a spin flip.

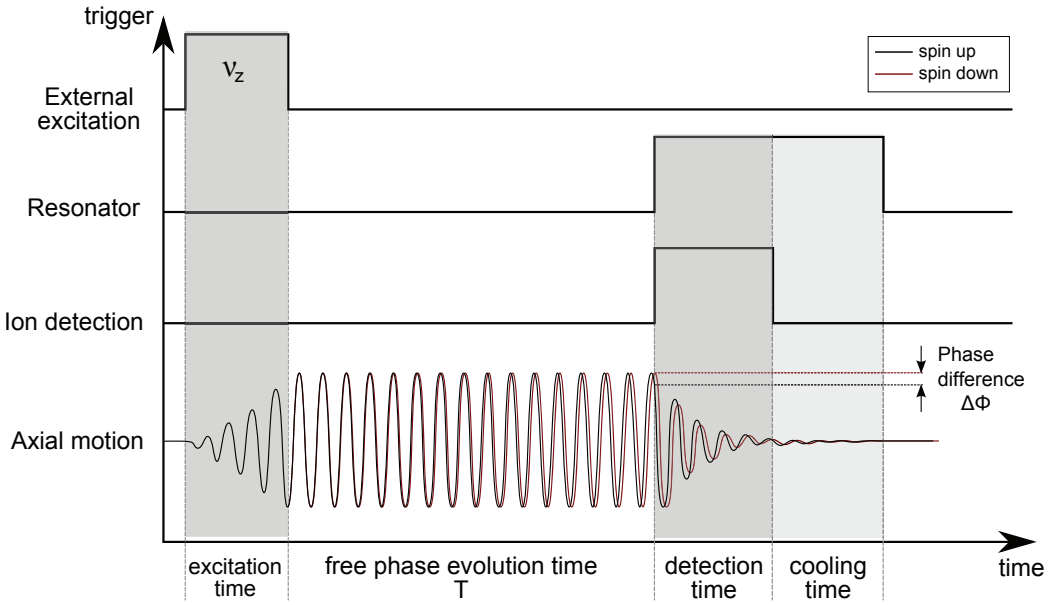

Figure 4.6: Measurement scheme and corresponding oscillation amplitude of the phase-sensitive detection technique. First, the ion's motion is excited by a dipolar excitation at the axial oscillation frequency ν_z to impress the initial phase. After a fixed evolution time with a detuned resonator to enable a free phase evolution, the resonator is switched back and the phase of the ion is detected. To ensure a sufficient cooling the ion is afterwards resistively cooled for several cooling time constants.

4.2.3 Analysis trap - Phase measurement

The axial frequency in the analysis trap can be measured with the dip-technique as well, which is used for trap optimization and cooling purposes. However, during the g-factor measurement, the AT is exclusively required to detect the spin orientation and there is no need for an accurate absolute frequency measurement. In fact, as described in Sec. 4.2.2, a small frequency difference has to be resolvable, which requires a high stability of the axial frequency and thus a measurement time as short as possible. Therefore it is advantageous to use a phase-sensitive measurement as proposed in [67], which enables a faster measurement with a higher resolution than the dip-technique. It exploits that for slightly different frequencies the phase evolution velocity is different.

The experimental realization is outlined in Fig. 4.6. Initially, a burst dipolar excitation at the assumed axial oscillation frequency ν_z is performed, which has to be strong enough to impress the phase on the axial oscillation of the ion. The axial resonator is detuned from the resonance frequency of the ion by applying appropriate electronic feedback (see Sec. 4.2.4). This detuning is required for a complete decoupling of the ion from the environment and allows for a free evolution of phase and frequency without a damping of the motion. After a

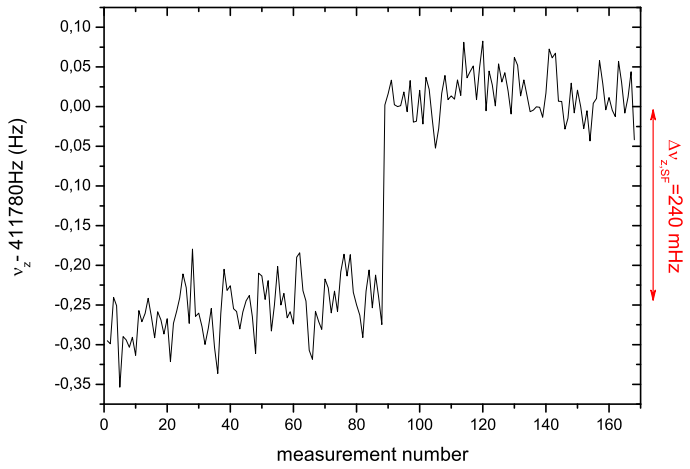

Figure 4.7: A spin flip of a single $^{28}Si^{11+}$-ion is clearly visible as a discrete jump $\Delta\nu_{z,SF}$ of the axial frequency. By irradiating microwaves at the Larmor frequency, a transition from the lower to the upper spin state is induced. The frequency measurement is performed with the phase-sensitive detection technique (for details see text).

well-defined evolution time T_{ev}, the resonator is switched back for the detection and cooling period. Then, an FFT-analyser is employed to read out the phase difference $\Delta\Phi$ relative to its 10 MHz reference signal from the peak in the frequency spectrum. This phase difference is related to the required frequency information by

$$\Delta\nu_z = \frac{\Delta\Phi}{2\pi T_{ev}}. \tag{4.28}$$

Finally, the ion is resistively cooled for a time period of several cooling time constants to ensure that it reaches thermal equilibrium with the detection system.

From Eq. (4.28) it can be seen that for a phase resolution better than 2π the obtained frequency resolution exceeds the Fourier limit $\delta\nu_{FL} = 1/T_{ev}$. To this account the phase evolution time should be chosen to yield a phase difference below 2π. On the other hand the obtainable frequency resolution increases with the evolution time since the phase difference increases and thus calls for a long evolution time. To resolve the frequency jump of 240 mHz due to a spin flip the phase evolution time was chosen to be T_{ev}=800 ms. Comparing this to the averaging time required for the dip detection of the order of several 10 s illustrates the time-related advantage of the phase-sensitive detection technique.

The measurement accuracy of this technique depends on

- the initial excitation amplitude, which is limited by the resulting systematic frequency shifts and the jitter due to the not perfectly reproducible excitation,

- the detuning of the resonator, limited due to technical reasons,
- the phase evolution time,
- the measurement time.

As described in Sec. 4.2.2 the detection of single spin flips was one of the main challenges of the experiment. After the described experimental improvements, we can nowadays distinguish between the two spin states with almost 100 % reliability as can be seen in Fig. 4.7, where the axial frequency is consecutively measured and a discrete jump due to a spin flip can be unambiguously resolved.

4.2.4 Electronic feedback

A very important feature for our experiment is active electronic feedback [68], which is used to shift the resonance frequency of the tank circuit or to change the effective temperature of the detection system and thus of the ion. To accomplish electronic feedback, the thermal noise of the tank circuit is amplified and capacitively fed back to the tank-circuit (see Fig. 4.8). The feedback strength or feedback gain G_{FB} can be influenced by a variable attenuator, whereas the type of the feedback can be chosen by adjusting the phase of the fed-back signal with a phase shifter. For a simplified treatment the noise of the amplifier is neglected.

In general, there are two different types of feedback which can be distinguished:

1. The phase of the feedback is shifted by $\pm 90°$ compared to the detected signal, hereby changing the effective parallel capacitance of the resonator [61] and thus resulting in a shifted position of the resonator without changing the quality factor Q. This feedback type is used when the interaction of the ion with the resonator should be minimized, required for example for the phase-sensitive detection technique in the analysis trap.

2. A 0°- or 180°-phase shifted feedback-signal is applied to vary the quality factor Q of the resonator and thus change the effective temperature of the ion. The resulting resistance and temperature depend on the feedback gain G_{FB} according to:

$$\begin{aligned} R_{\mathrm{eff}} &= (1 \pm G_{\mathrm{FB}})R \\ T_{\mathrm{eff}} &= (1 \pm G_{\mathrm{FB}})T. \end{aligned} \tag{4.29}$$

   The two different algebraic signs account for the two possibilities which can be adjusted by an appropriate choice of the phase:

   - *Positive feedback* (0°) increases the quality factor of the resonator as well as the temperature and the dip-width of the ion. It is applied for a faster detection of the dip.

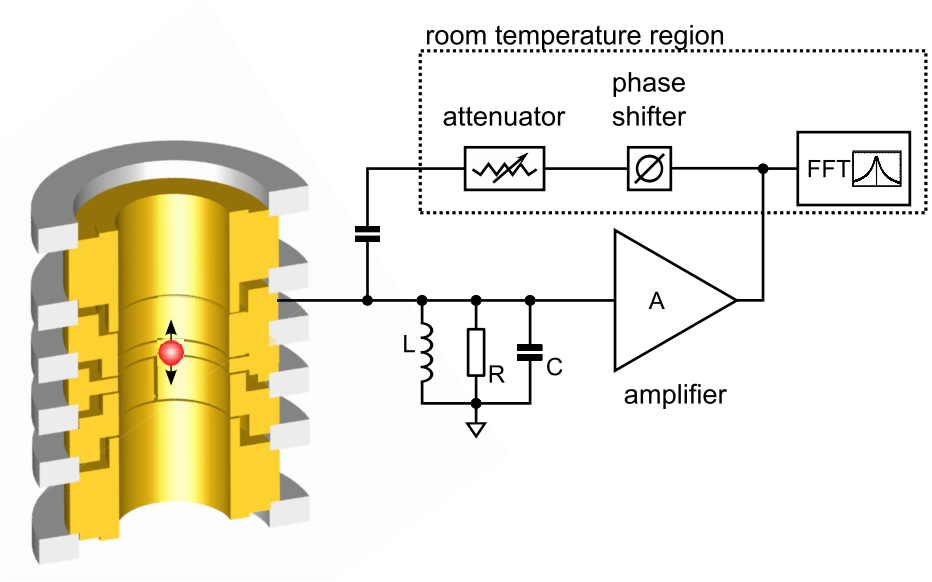

Figure 4.8: Setup for the application of electronic feedback. The detected signal is amplified and phase-shifted before it is fed back to the tank-circuit. Appropriate choice of amplification and phase allow for changing the resonance frequency of the detection system and/or its quality factor.

- *Negative feedback* (180°) decreases the quality factor of the resonator as well as the temperature and the dip-width of the ion. It is used to cool the ion motion below the environmental temperature.

In the experiment the additional noise of the amplifier has to be considered, which basically means that the achievable temperature with electronic feedback is not arbitrarily low but has a minimum, which depends on temperature and signal-to-noise ratio (SNR) of the detector. Then, even stronger feedback results in an increased effective temperature and thus should be avoided [61, 68].

For phases between the described discrete values, the resulting feedback signal is a mixture of both cases. The size of the shift of the resonator position or the change of the quality factor can be continuously adjusted with the phase shifter.
Experimentally, feedback is adjusted by first choosing a suited feedback gain G_{FB} and then scanning the phase until the required feedback is obtained. In Fig. 4.9 the effect of positive and negative feedback on the resonator and the signature of the ion is demonstrated.

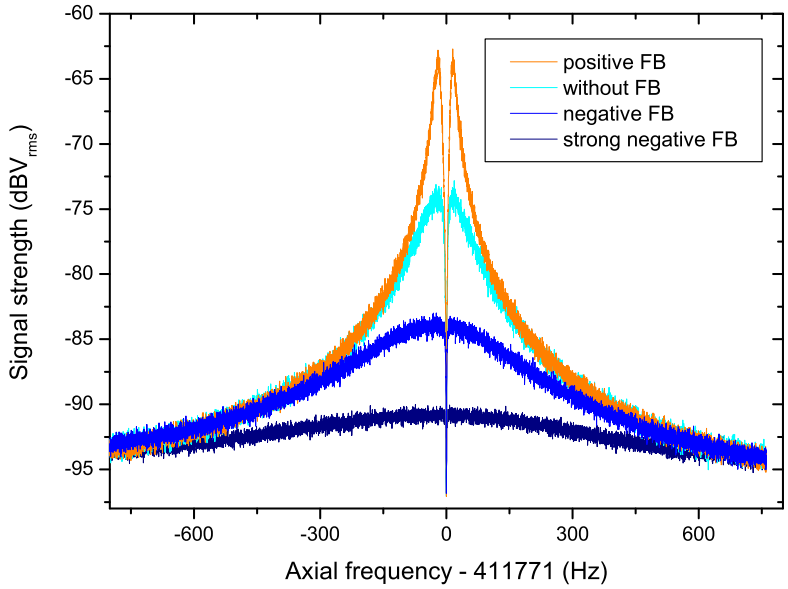

Figure 4.9: The effect of 0°/180°-electronic feedback is illustrated by applying various strengths of feedback to the axial detection system of the AT [61]. For negative feedback the quality factor as well as the width of the dip are decreased while positive feedback increases both.

4.3 Modified cyclotron frequency measurement

For the g-factor measurement the modified cyclotron frequency ν_+ has to be determined with the highest precision of all eigenfrequencies (see Sec. 3.1), making its detection most important. The determination of the modified cyclotron frequency is conducted with different detection techniques, which all employ the axial detection system as described in the following.

4.3.1 Precision trap - Double-dip technique

In this section, the "double-dip" technique is introduced, which allows for a measurement of the modified cyclotron frequency in the precision trap as well as for cooling of both radial modes. A detailed mathematical description can be found in [54, 69] and references therein. A fully quantum mechanical approach is presented in [70].
By irradiating a radiofrequency (rf) field at the lower sideband $\nu_{\mathrm{rf}} = (\nu_+ - \nu_z)$ the modified cyclotron frequency is coupled to the axial frequency [69]. The system can be understood

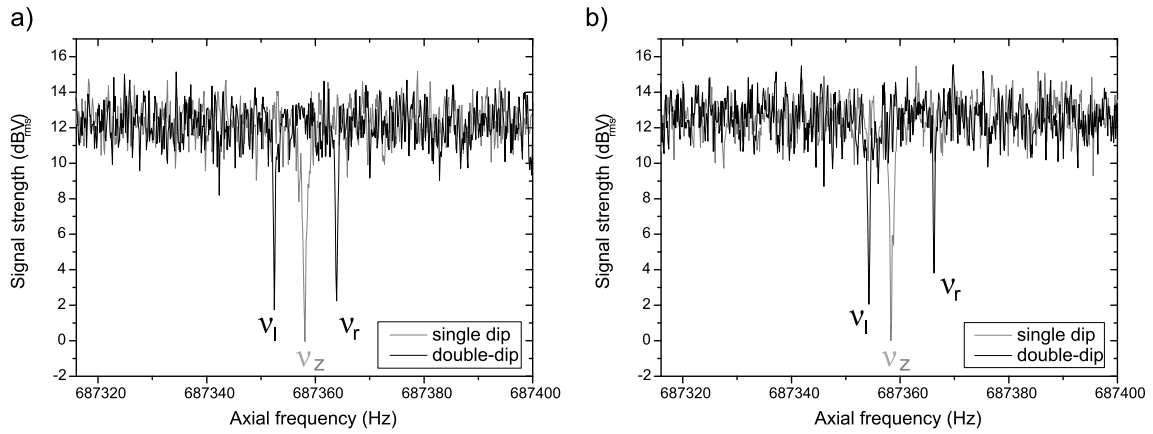

Figure 4.10: Cyclotron double-dip (a) with almost no detuning and (b) with a slight detuning of the coupling frequency from the lower sideband. The grey line shows the single axial dip recorded directly before the double-dip. The larger the detuning the more asymmetric are the widths, depths and positions of the two dips with respect to the single dip.

as an analogon to quantum mechanical dressed states. While irradiating a continuous sinusoidal waveform, the energy is permanently transferred between the two modes with the Rabi-frequency Ω_0 depending on the strength of the coupling field [70]. As a result of this periodic energy transfer, the axial motion is amplitude modulated according to

$$\begin{aligned} z(t) &= z_0 \cos\left(\frac{2\pi\Omega_0}{2}t\right)\sin(2\pi\nu_z t+\varphi) \\ &= \frac{1}{2}z_0\left[\sin\left(2\pi\left(\nu_z-\frac{\Omega_0}{2}\right)t+\varphi'\right)+\sin\left(2\pi\left(\nu_z+\frac{\Omega_0}{2}\right)t+\varphi'\right)\right]. \end{aligned} \tag{4.30}$$

φ and φ' denote arbitrary phases of the oscillation. It can be seen from the second relation that the axial dip splits into two (see Fig. 4.10), the so-called *double-dip*, with frequencies

$$\nu_\mathrm{l} = \nu_\mathrm{z} - \frac{\Omega_0}{2} \qquad \text{and} \qquad \nu_\mathrm{r} = \nu_\mathrm{z} + \frac{\Omega_0}{2}. \tag{4.31}$$

Here ν_z is the unperturbed axial frequency in absence of a coupling field.
If the coupling frequency is slightly detuned with regard to the exact sideband frequency $\nu_\mathrm{rf} = (\nu_+ - \nu_\mathrm{z} + \delta)$, the energy transfer from one mode to the other is not completely modulated. In this case the Rabi-frequency is slightly modified, depending now on the detuning δ: $\Omega = \sqrt{\Omega_0^2 + \delta^2}$. The resulting split frequencies are:

$$\nu_\mathrm{l} = \nu_\mathrm{z} - \frac{\delta}{2} - \frac{\Omega}{2} \qquad \text{and} \qquad \nu_\mathrm{r} = \nu_\mathrm{z} - \frac{\delta}{2} + \frac{\Omega}{2}. \tag{4.32}$$

Obviously, only for vanishing detuning $\delta = 0$ the position of the double-dip is symmetric around the uncoupled axial frequency of the single dip.

Adding up the two resulting frequencies yields

$$\nu_\mathrm{l} + \nu_\mathrm{r} = 2\nu_\mathrm{z} - \delta = \nu_\mathrm{z} - \nu_\mathrm{rf} + \nu_+ \tag{4.33}$$

and reveals the possibility to determine the modified cyclotron frequency by measuring the frequencies of the single dip ν_z and the double-dip ν_l and ν_r while knowing the irradiated rf-frequency ν_rf

$$\nu_+ = \nu_\mathrm{rf} - \nu_\mathrm{z} + \nu_\mathrm{l} + \nu_\mathrm{r}. \tag{4.34}$$

A remarkable feature of this relation is that a possible detuning of the coupling frequency is exactly cancelled out and does not influence the determination of the modified cyclotron frequency.
The measurement of the axial frequency with the single dip is performed before and after the double-dip in order to eliminate systematic shifts due to a linear drift of the voltage applied to the electrodes. An interpolation of the two single measurements yields the axial frequency information during the double-dip measurement.

Sideband cooling

Another important application of the sideband coupling is the cooling of the radial modes. The energy transfer between the two modes means that the quantum number of one mode is increased while the other is decreased and vice versa. This means, that the quantum numbers n_z for the axial and $n_\pm$ for the radial modes equal and thus the expectation value of the energy of both modes are related to each other by their respective frequency ratio:

$$\langle E_\pm \rangle = h\nu_\pm \left(\langle n_\pm \rangle + \frac{1}{2} \right) = h\nu_\pm \left(\langle n_\mathrm{z} \rangle + \frac{1}{2} \right) = \frac{\nu_\pm}{\nu_\mathrm{z}} h\nu_\mathrm{z} \left(\langle n_\mathrm{z} \rangle + \frac{1}{2} \right) = \frac{\nu_\pm}{\nu_\mathrm{z}} \langle E_\mathrm{z} \rangle. \tag{4.35}$$

This is, according to $\langle E \rangle = k_\mathrm{B} T$ equivalent to

$$T_+ = \frac{\nu_+}{\nu_\mathrm{z}} T_\mathrm{z} \qquad \text{and} \qquad T_- = \frac{\nu_-}{\nu_\mathrm{z}} T_\mathrm{z}. \tag{4.36}$$

Since the axial motion is coupled to the axial detection system it is permanently resistively cooled as described in Sec. 4.1.1. Thus, the excess energy, which is transferred from the radial mode to the axial mode is dissipated until the equilibrium temperature for the radial mode according to Eq. (4.36) is reached, leading to a cooling of the radial mode as well. This is the standard cooling technique for the magnetron motion and, since no cyclotron resonator was available for direct resistive cooling, for the modified cyclotron mode as well.

Furthermore, the sideband coupling is employed to measure the axial temperature in the analysis trap. The B_2-term shifts the axial frequency according to the ion's modified cyclotron amplitude and thus is a measure of the energy in the modified cyclotron mode

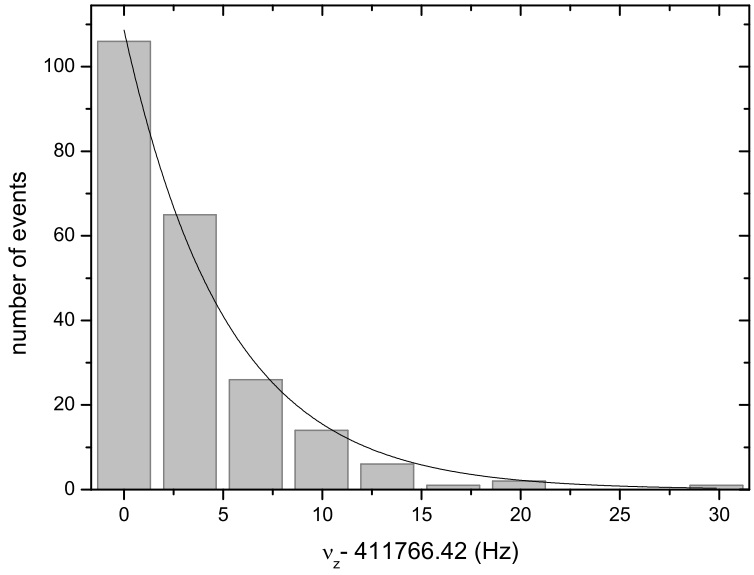

Figure 4.11: Measurement of the axial temperature in the analysis trap. The modified cyclotron mode is repeatedly coupled to the axial mode and the respective axial frequency shift is measured. The histogram of the axial frequency shifts yields the Boltzmann-distribution. From an exponential fit (black line) the axial temperature can be deduced to 1.9 K during the application of negative electronic feedback.

(compare Eq. (3.18)). Being coupled to the tank circuit the axial energy changes on timescales of the cooling time constant. The energy is Boltzmann-distributed

$$\frac{p(E_\mathrm{z})}{dE_\mathrm{z}} = \frac{1}{k_\mathrm{B}T_\mathrm{z}} e^{-\frac{E_\mathrm{z}}{k_\mathrm{B}T_\mathrm{z}}} \tag{4.37}$$

with an expectation value of

$$\langle E_\mathrm{z} \rangle = k_\mathrm{B}T_\mathrm{z} = k_\mathrm{B}T_\mathrm{tc}, \tag{4.38}$$

which depends on the temperature T_tc of the free charge carriers in the tank circuit. For the temperature measurement, the axial energy is transferred to the modified cyclotron mode by sideband coupling. From the very moment on where the coupling is switched off the energy stored in the cyclotron mode is constant. This energy represents one statistical value of the Boltzmann-distribution of the axial mode. Knowing the size of the B_2-term, the corresponding axial frequency shift can be used according to Eq. (3.18) to determine the energy in the cyclotron mode. The coupling is performed several 10 to 100 times and after each coupling the axial dip is recorded and the frequency is compared to the minimum

achievable frequency, corresponding to the minimum cyclotron energy. Here, the magnetron energy is considered to be constant and thus is neglected. A histogram of the frequency differences yields the Boltzmann-distribution of the cyclotron energy (see Fig. 4.11). The expectation value of the modified cyclotron temperature can be obtained from an exponential fit to the data and is directly related to the axial temperature according to Eq. (4.36). This method can also be employed to measure the axial temperature in the precision trap when performing the coupling there and adiabatically transporting the ion to the analysis trap where the frequency shift is measured. This requires the assumption that the temperature of the ion is not affected by the transport, which has been experimentally verified.

Moreover, this method can be used to cool the cyclotron motion below the equilibrium temperature according to Eq. (4.36). Therefore, the Boltzmann-distribution has to be measured once and from this measurement a threshold for the axial frequency can be determined, which corresponds to the maximum allowed energy stored in the cyclotron mode. With this information the coupling and the corresponding axial frequency measurement is repeated until the axial frequency is below the threshold. The choice of this threshold not only defines the distribution of the initial cyclotron temperature but also the mean time, which is required to find an accepted energy value. This method is commonly used to cool the cyclotron motion in the analysis trap during a g-factor measurement.

4.3.2 Precision trap - PnA

A new measurement technique for the modified cyclotron frequency has been developed by Sven Sturm in his Ph.D.-thesis to replace the double-dip technique and overcome its limitations [61, 71], namely the long required averaging time, the linewidth of the dip and the measurement via the axial frequency, which depends on the trapping potential. In the style of the well-known PnP-technique (Pulse 'n' Phase) [72] the new technique is denoted as PnA (Pulse 'n' Amplify), since it effectively can be considered as an extension of the PnP-technique. It was shown that the experimentally achievable precision for the g-factor could be increased by one order of magnitude with the PnA-technique. However, it was not applied in the g-factor measurement performed in this thesis since the comparison between the experimental and theoretical g-factor for $^{28}Si^{11+}$ is anyhow limited by theory already at the $2.5 \cdot 10^{-8}$-level. Moreover, the double-dip technique is on the one hand more reliable due to a simpler experimental implementation and on the other hand constitutes a lower risk to loose the ion. Nevertheless, the PnA-technique was used for several other measurements within this work where the resolution of the double-dip method was not sufficient to resolve the investigated effects and is therefore briefly introduced in the following.

As a first step the phase of the cyclotron mode is defined by a short dipolar excitation pulse at ν_+ (see Fig. 4.12). After a well-defined evolution time the cyclotron mode is coupled to the axial mode by irradiating an rf-signal at $\nu_{\mathrm{rf}} = \nu_+ + \nu_{\mathrm{z}}$. The coupling pulse transfers

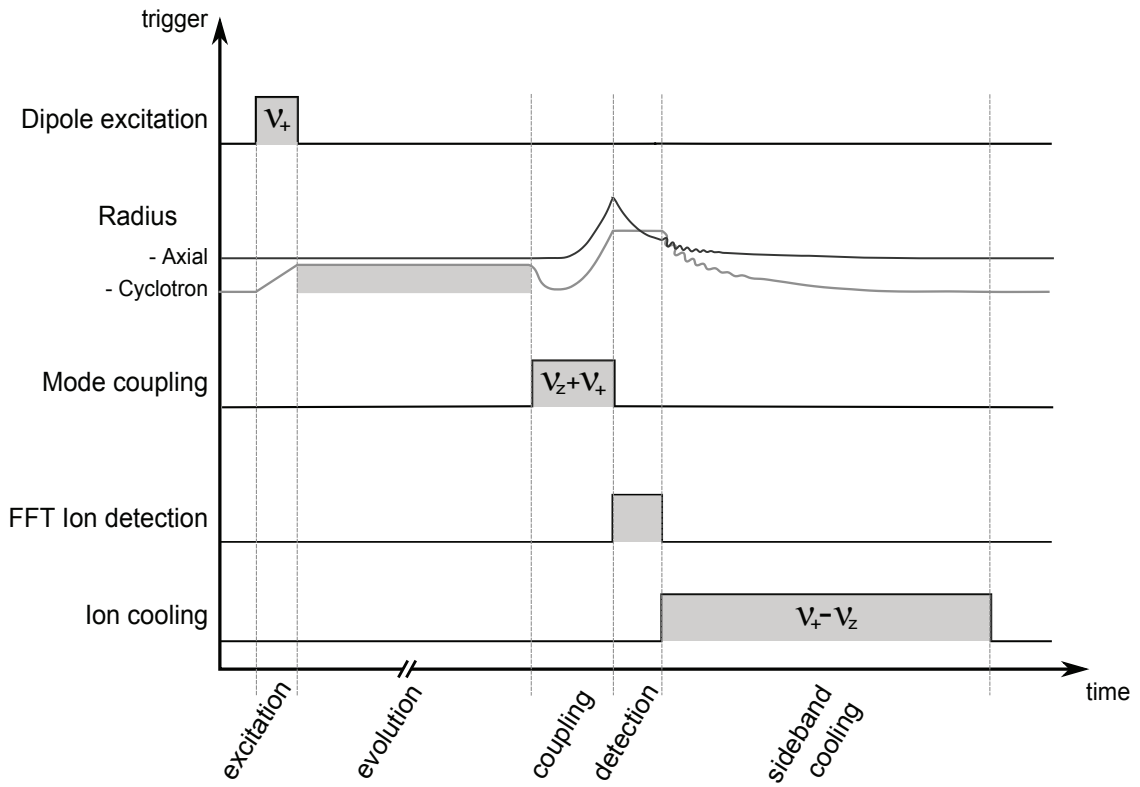

Figure 4.12: Measurement scheme for the PnA-technique [71]. First the cyclotron mode is excited to define its phase. After a well-defined evolution time, the cyclotron mode is coupled to the axial mode by an rf-excitation on the upper sideband, resulting in an amplification of cyclotron and axial radii while transferring the cyclotron phase to the axial oscillation. Then the axial phase is read out and both modes are cooled.

the phase information of the modified cyclotron mode to the axial mode and excites both modes. The axial phase is then determined from the resulting peak with an FFT-analyser. Finally, both the axial and the modified cyclotron mode, are cooled again.
The application of the upper sideband is the very important difference to the PnP-technique, which uses the lower sideband $\nu_{\mathrm{rf}} = \nu_+ - \nu_{\mathrm{z}}$. In order to detect the phase information of the peak both techniques require an excitation of the axial oscillation above the thermal noise of the resonator. However, the origin of the required energy is essentially different:

- Coupling the two modes with the lower sideband $\nu_{\mathrm{rf}} = \nu_+ - \nu_{\mathrm{z}}$ results in an energy exchange as described in chap. 4.3.1. This means that, according to Eq. (4.35), the axial energy after the coupling is defined (and thus limited) by the modified cyclotron energy before the coupling. Accordingly, the energy of the modified cyclotron energy before the coupling has to be sufficiently high. Such a high cyclotron energy causes systematic frequency shifts and, due to the limited reproducibility of the excitation, a

high frequency jitter.

- When applying the upper sideband $\nu_{\mathrm{rf}} = \nu_+ + \nu_{\mathrm{z}}$ the required energy for the excitation of the axial mode originates from the coupling field without any upper limitation. This means that the achievable axial amplitude is only determined by the strength of the coupling pulse and does not depend on the cyclotron amplitude before the coupling. In this case, the initial excitation of the modified cyclotron motion only has to be strong enough to define its phase, revealing the advantage of a cyclotron motion as cold as possible.

Accordingly, the application of the upper sideband to couple the modified cyclotron mode to the axial mode enables a measurement of the modified cyclotron frequency at very low energies.
When measuring the absolute modified cyclotron frequency several phase measurements for different evolution times are required since the slope of the unwrapped phases of the obtained linear function yields the frequency information. However, being only interested in relative changes of the modified cyclotron frequency, it is sufficient to perform consecutive measurements for the same evolution time. The achieved resolution thereby depends on the evolution time, which on the one hand has to be chosen long enough to resolve the investigated effect but on the other hand must not be too long to result in a phase jump larger than 2π and thus mask the true size of the frequency change.

4.3.3 Analysis trap - Modified cyclotron frequency detection

A measurement of the modified cyclotron frequency in the analysis trap is required to determine the magnetic field and thus the expected Larmor frequency. For an expected relative width of the Larmor resonance[1] of 10^{-6} the modified cyclotron frequency has to be measured to the same relative uncertainty of $\delta\nu_+/\nu_+ = 10^{-6}$. However, the application of the double-dip technique is not possible for a single $^{28}Si^{11+}$-ion with the present detection system. Due to the coupling of the axial frequency to the thermal bath of the tank circuit, the fluctuation of the cyclotron energy during the sideband coupling results in axial frequency shifts as described in section 4.3.1 and the double-dip is smeared out. This effect is too large to detect the double-dip. Only the disappearance of the single dip can be observed when irradiating an rf-frequency close to true coupling frequency, which was formerly used to determine the modified cyclotron frequency [66].
A more sophisticated technique uses the axial frequency shift $\Delta\nu_{\mathrm{z}} = \nu_{\mathrm{z,hot}} - \nu_{\mathrm{z,cold}}$ as a function of the cyclotron excitation $\nu_{\mathrm{rf}} \approx \nu_+$. Therefore, the cyclotron motion is excited

[1] This was actually not the case for this measurement as will be described in Sec. 7.5.3

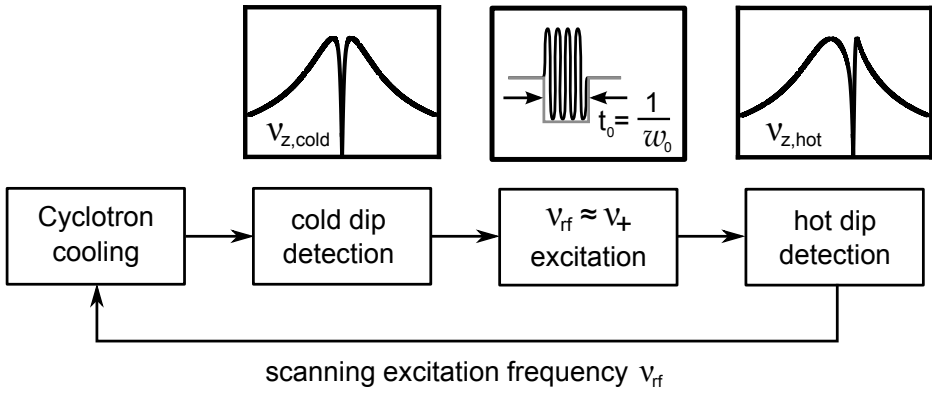

Figure 4.13: Measurement scheme for the modified cyclotron frequency in the analysis trap. After cooling the modified cyclotron mode below a fixed threshold an axial dip for the cold cyclotron mode is measured. Then an excitation pulse ν_{rf} close to the expected modified cyclotron frequency is performed whose length t_0 determines the width w_0 of the obtained resonance (see Fig. 4.14). Finally an axial dip for the hot cyclotron mode is detected and the cycle starts again with a different excitation frequency.

with a burst pulse and the resulting axial frequency shift $\Delta\nu_{\mathrm{z}}$ according to

$$\frac{\Delta\nu_{\mathrm{z}}}{\nu_{\mathrm{z}}} = \frac{B_2}{B_0}\frac{1}{4\pi^2 m\nu_{\mathrm{z}}^2}E_+ \tag{4.39}$$

is measured. Scanning the excitation frequency and measuring the dependence of the frequency shift yields a resonance like the one shown in Fig. 4.14.

The general form of this resonance depends on the ratio between axial temperature and length of the excitation pulse. In the presented case, which is the commonly used one, the axial temperature is low ($T_{\mathrm{z}} \sim 2\,\mathrm{K}$) whereas the excitation pulse is rather short ($t_0 \sim 0.1\,\mathrm{s}$) and therefore determines the frequency resolution. To calculate the theoretical lineshape of the resonance, the Fourier transform of the excitation pulse, being a sinusoidal signal triggered with a rectangular pulse of length $t_0 = 1/w_0$, has to be calculated

$$F(\nu_{\mathrm{rf}}) = \int_{-\infty}^{\infty} \sin(\nu_+ \cdot t)\cdot \mathrm{rect}(w_0 \cdot t)\mathrm{e}^{-i\,\nu_{\mathrm{rf}}\,t}\mathrm{d}t. \tag{4.40}$$

Due to the convolution theorem this can be solved by calculating the individual Fourier transforms and convolving the results. The Fourier transform of the sine is the delta-function

$$F_1(\nu_{\mathrm{rf}}) = \int_{-\infty}^{\infty} \sin(\nu_+ \cdot t)\mathrm{e}^{-i\,\nu_{\mathrm{rf}}\,t}\mathrm{d}t = i\pi\delta(\nu_{\mathrm{rf}} - \nu_+), \tag{4.41}$$

whereas the Fourier transform of the rectangular pulse is the sinc-function

$$F_2(\nu_{\mathrm{rf}}) = \int_{-\infty}^{\infty} \mathrm{rect}(w_0 \cdot t)\mathrm{e}^{-i\,\nu_{\mathrm{rf}}\,t}\mathrm{d}t = \frac{1}{w_0}\frac{\sin(\frac{\nu_{\mathrm{rf}}}{2w_0})}{(\frac{\nu_{\mathrm{rf}}}{2w_0})} = \frac{1}{w_0}\mathrm{sinc}\left(\frac{\nu_{\mathrm{rf}}}{2w_0}\right). \tag{4.42}$$

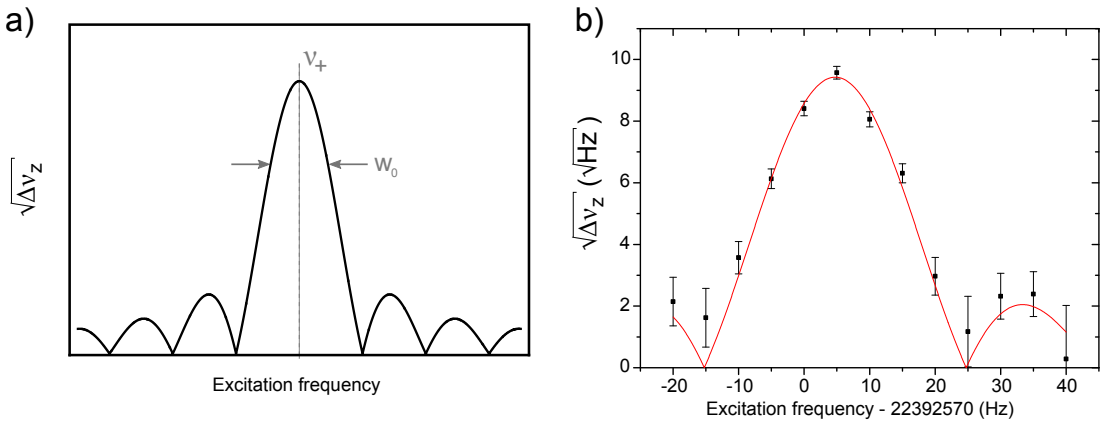

Figure 4.14: The modified cyclotron frequency in the analysis trap is determined by measuring the axial frequency shift $\Delta\nu_z$ as a function of the excitation frequency. The expected (simplified) linewidth is a sinc-function as shown in a), with a width depending on the length of the excitation. The centre frequency corresponds to the sought-after modified cyclotron frequency and is extracted from a fit to the measured data points (b). The data points are averaged over 11 single measurements.

The absolute value of the convolution of F_1 and F_2 yields the real function

$$\begin{aligned} |F(\nu_{\mathrm{rf}})| = |F_2(\nu_{\mathrm{rf}}) * F_1(\nu_{\mathrm{rf}})| &= \left| A \cdot \int_{-\infty}^{\infty} \mathrm{sinc}\left(\frac{\nu}{2w_0}\right) \delta(\nu_{\mathrm{rf}} - \nu_+ - \nu)\mathrm{d}\nu \right| \\ &= \left| A \cdot \mathrm{sinc}\left(\frac{1}{2w_0}(\nu_{\mathrm{rf}} - \nu_+)\right) \right|, \end{aligned} \tag{4.43}$$

where the prefactors are combined in an overall amplitude factor A.
As a last step to obtain the theoretical form of the resonance one has to consider that the excitation linearly increases the radius of the cyclotron motion, whereas the axial frequency shift (see Eq. (4.39)) is related to the energy

$$E_+ = \frac{1}{2} m (2\pi\nu_+)^2 r_+^2 \tag{4.44}$$

and thus to the square of the radius. This means that the square root of the measured frequency shift has to be used for the data analysis, finally resulting in

$$\sqrt{\Delta\nu_z} = \left| A \cdot \mathrm{sinc}\left(\frac{1}{2w_0}(\nu_{\mathrm{rf}} - \nu_+)\right) \right|. \tag{4.45}$$

The uncertainty for each measurement depends on the reproducibility of the initial cold cyclotron energy, which is defined by the threshold chosen for the sideband cooling as described in Sec. 4.3.1. To minimize the resulting uncertainty the measurement for each excitation frequency is repeated several times.

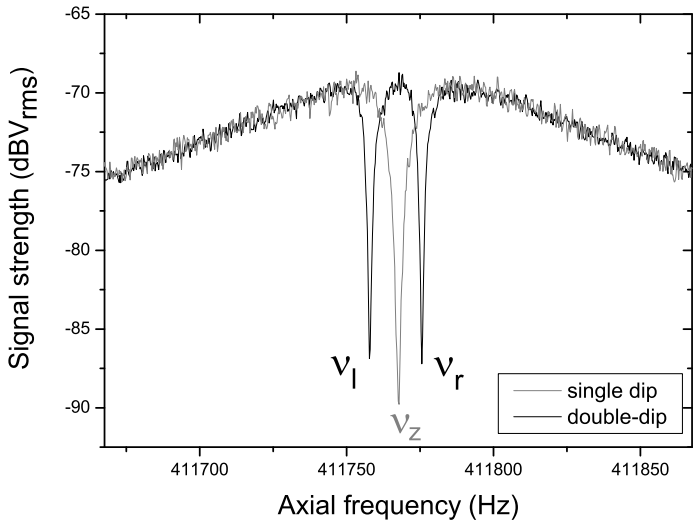

Figure 4.15: Magnetron double-dip in the analysis trap. The grey curve shows the single axial dip without any coupling field, the black line shows the splitting of the dip when coupling the magnetron to the axial mode.

Using long excitation times where the obtained frequency resolution is not limited by the pulse length or employing higher axial temperatures, the lineshape of the resonance is a Boltzmann-curve. This can be understood by considering that within the magnetic bottle the averaged magnetic field, which is experienced by the ion during the excitation, depends on its axial amplitude and thus on its energy. Therefore, the Boltzmann-distribution of the axial energy is reflected in the averaged magnetic field and accordingly in the modified cyclotron frequency as well. Already for an axial temperature increased by a factor of four this becomes visible.
Accordingly, for a high-precision measurement of the modified cyclotron frequency with this technique, the exact lineshape has to be calculated by convolving the asymmetric Boltzmann-distribution with the symmetric sinc-function to avoid systematic shifts. However, to determine the modified cyclotron frequency to the required precision of 22 Hz in the analysis trap, it is sufficient to simply fit the sinc-function to the data and extract the position of the maximum.

4.4 Magnetron frequency measurement

The magnetron frequency is detected by the double-dip technique in both traps. In a similar way as described for the modified cyclotron frequency, the magnetron frequency can

be coupled to the axial frequency. However, in this case the upper sideband $\nu_{\mathrm{rf}} = \nu_{\mathrm{z}} + \nu_{-}$ has to be used since the magnetron motion is a metastable motion whose energy increases with decreasing quantum number. The magnetron frequency can be obtained from the double-dip via

$$\nu_{-} = \nu_{\mathrm{rf}} + \nu_{\mathrm{z}} - \nu_{\mathrm{r}} - \nu_{\mathrm{l}}. \tag{4.46}$$

To achieve a relative uncertainty of $\delta g/g = 10^{-9}$ it is sufficient, according to Eq. (3.11), to measure the magnetron frequency to $\delta\nu_{-}/\nu_{-} = 10^{-3}$. Thus, it is measured only before and, as a cross-check, after the g-factor measurement.

Chapter 5

The experimental setup

The experimental setup for the high-precision measurement of the g-factor of highly-charged ions has to meet very demanding requirements, namely a strong homogeneous magnetic field, a cryogenic environment, an extremely good vacuum in the trap region and low-noise detection systems. The setup to fulfill these conditions is introduced in this chapter. Especially the large components, like the overall layout, the magnet, the cryostat and the apparatus with the helium dewar are still the same as in the design of the first g-factor experiment of light ions in Mainz [73]. However, the trap tower and almost all parts of the cryogenic electronics had to be redesigned for the current g-factor experiment of medium-heavy highly-charged ions. Furthermore, in the course of this thesis, the external influences like temperature, pressure and magnetic field fluctuations have been minimized by appropriate stabilization systems, which are described in chapter 6.
In the first section of this chapter the overall setup is introduced, including the superconducting magnet and the cryostats. Afterwards the trap tower is presented and discussed in some detail. Here, also the design of a new reflector electrode and the careful optimization of the trap electrodes are described, both having been important steps to achieve the high stability of the axial frequency in the analysis trap and hereby enabling the detection of a single spin-flip. The last part is dedicated to the electronic parts of the setup, namely the cryogenic amplifiers, the high-precision voltage source, the excitation lines and the microwave setup.
Further details of the design and the setup can be found in the theses of my former Ph.D.-colleagues Joseba Alonso [74], Birgit Schabinger [66] and Sven Sturm [61].

5.1 The overall setup

A sketch of the overall setup is shown in Fig. 5.1. The apparatus is vertically inserted into the bore of a superconducting magnet. A liquid nitrogen cryostat is attached on top of the

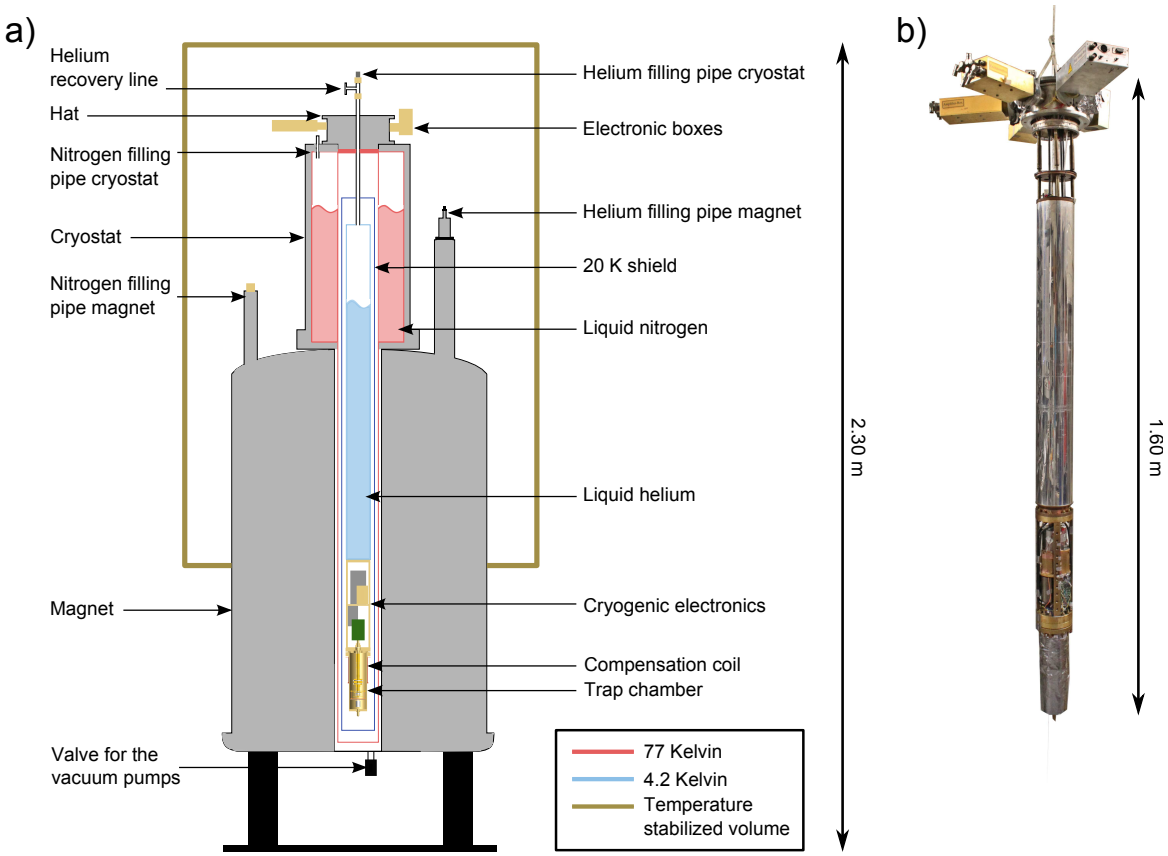

Figure 5.1: Cross section of the experimental setup (a) and a photo of the apparatus (b), which is inserted into the magnet. The apparatus is shown without the 20 K shield.

magnet whereas the liquid helium cryostat is located in the apparatus itself. At the so-called "hat", which rests on the cryostat and thus fixes the apparatus, the room-temperature electronics boxes are attached to several flanges. The high-precision voltage source UM1-14 as well as the voltage supply BS1-12 for the cryogenic amplifiers are located on top of these boxes. The experiment from approximately half the height of the magnet is enclosed by a box to provide a temperature stabilized environment as developed in the course of this thesis (see Sec. 6.1).

All additionally required electronic devices, as for instance FFT-analyser, frequency synthesizers and microwave setup, are placed on a rack next to the magnet. About a dozen frequency synthesizer are employed for the various excitation and cooling purposes, which are synchronized with the 10 MHz signal of the rubidium atomic clock FS725 from Stanford Research. A personal computer is used for remote control of the devices via GPIB, USB, RS232 or Ethernet connections. The software "National Instruments *LabView*" is not only employed to control these devices, but also for data acquisition and automation of measurement routines.

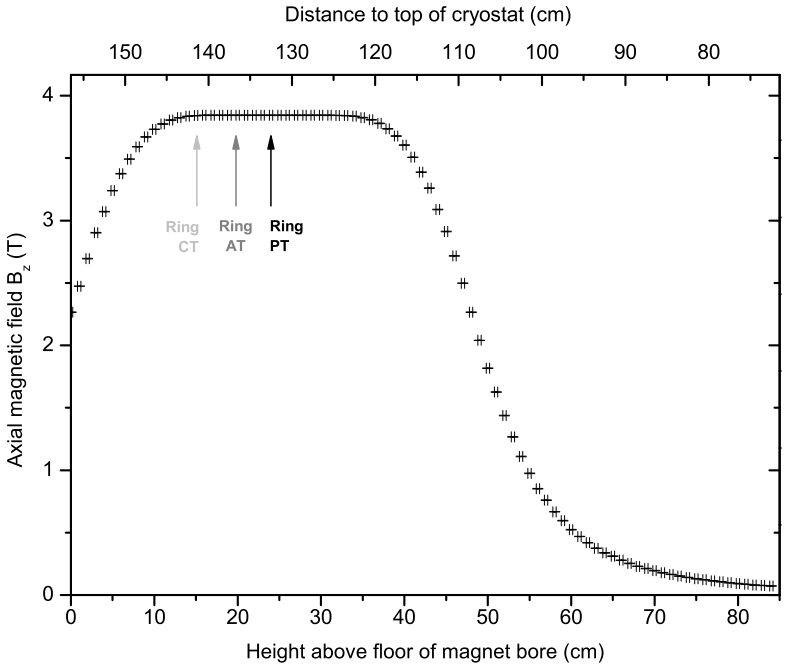

Figure 5.2: Axial component of the magnetic field measured with a Hall-probe within the bore of the superconducting magnet. The positions of the particular ring electrodes are marked for the three traps.

5.1.1 The magnet

The superconducting NMR-magnet from Oxford Instruments has a vertical room-temperature bore of 127 mm and provides a magnetic field of 3.764 T. The axial component of the magnetic field, measured with a Hall-probe, is shown in Fig. 5.2. For the superconducting coils liquid helium and nitrogen reservoirs are required, which have a capacity of 28.8 l and 84 l, respectively, corresponding to holding times of about two weeks and nine days. At the lower bottom of the bore, vacuum pumps can be connected via a valve to evacuate an insulation vacuum in the bore of the magnet in order to minimize heat conductance to the helium cryostat.

5.1.2 The liquid nitrogen and helium cryostats

The trap chamber as well as the detection electronics are operated at 4.2 K to achieve an eXtremely High Vacuum (XHV)[1] in the trap region, to minimize the Johnson noise in

[1] XHV denotes vacuum with pressures below 10^{-12} mbar.

the electronic parts and to enable a cooling of the ion's motion to amplitudes as small as possible. The temperature of 4.2 K is achieved by a liquid helium cryostat, which is installed within the apparatus and has a refill volume of about 5 l. It is directly attached to the cryogenic-electronic section and massive copper rods lead to the trap tower to provide thermal conductivity. The filling pipe is simultaneously used as mechanical suspension for the whole apparatus. It is connected to the helium recovery line, which is a closed system for the liquefaction of the evaporated helium. In order to reduce the thermal load on the helium cryostat, a 20 K-shield, connected to the filling pipe of the helium dewar, is placed around the helium cryostat, the cryogenic electronics and the trap chamber. For further reduction of the thermal load a 77 K-stage is implemented, which is provided by a liquid nitrogen cryostat. It is placed on top of the superconducting magnet and has a refill volume of 12 l. The attached 77 K-shield is permanently installed within the magnet bore. Inserting the apparatus into the magnet, the 77 K-shield is closed by an aluminium plate with fins providing the thermal contact.

5.2 The triple Penning trap system

The centerpiece of the experiment is the trap tower, which is shown in Fig. 5.3. It mainly consists of three cylindrical open-endcap Penning traps: the creation trap (CT), the analysis trap (AT) and the precision trap (PT).
Starting from the top, the trap tower is screwed to the upper montage flange (UMF). It contains several vacuum feedthroughs to guide the signals into the trap chamber and vice-versa and a quartz glass window as an inlet for the microwave irradiation. The precision trap is separated from this window by a long distance electrode to be placed in the homogeneous region of the magnet and to avoid perturbations of the trapping potential due to possible surface-charges on the window. Five transport electrodes connect the PT to the analysis trap with the ferromagnetic ring electrode. Below the AT there is the mini-EBIT for the creation of the highly-charged ions, including the reflector electrode and the creation trap. The electrodes (see Fig. 5.4), except for the ring electrode of the AT, are made of gold-plated oxygen-free high thermal conductivity (OFHC) copper. Sapphire rings and, in case of the high-voltage electrodes, macor rings ensure electric isolation between the electrodes. Split electrodes are separated by two sapphire balls with a diameter of 1 mm.
The trap chamber, which encloses the trap tower, is screwed to the UMF and sealed with indium. At its bottom, a pinch-off-tube of thin copper is used to connect the turbo molecular pumps for the evacuation of the vacuum before cryocooling. Having achieved a sufficient vacuum, the pinch-off-tube is cold-welded, leaving a hermetically sealed trap chamber. When cooling down the apparatus to 4.2 K the vacuum is significantly improved due to the cryo-pump effect, therefore, achieving an XHV of $p \leq 10^{-16}$ mbar. This results in almost arbitrary

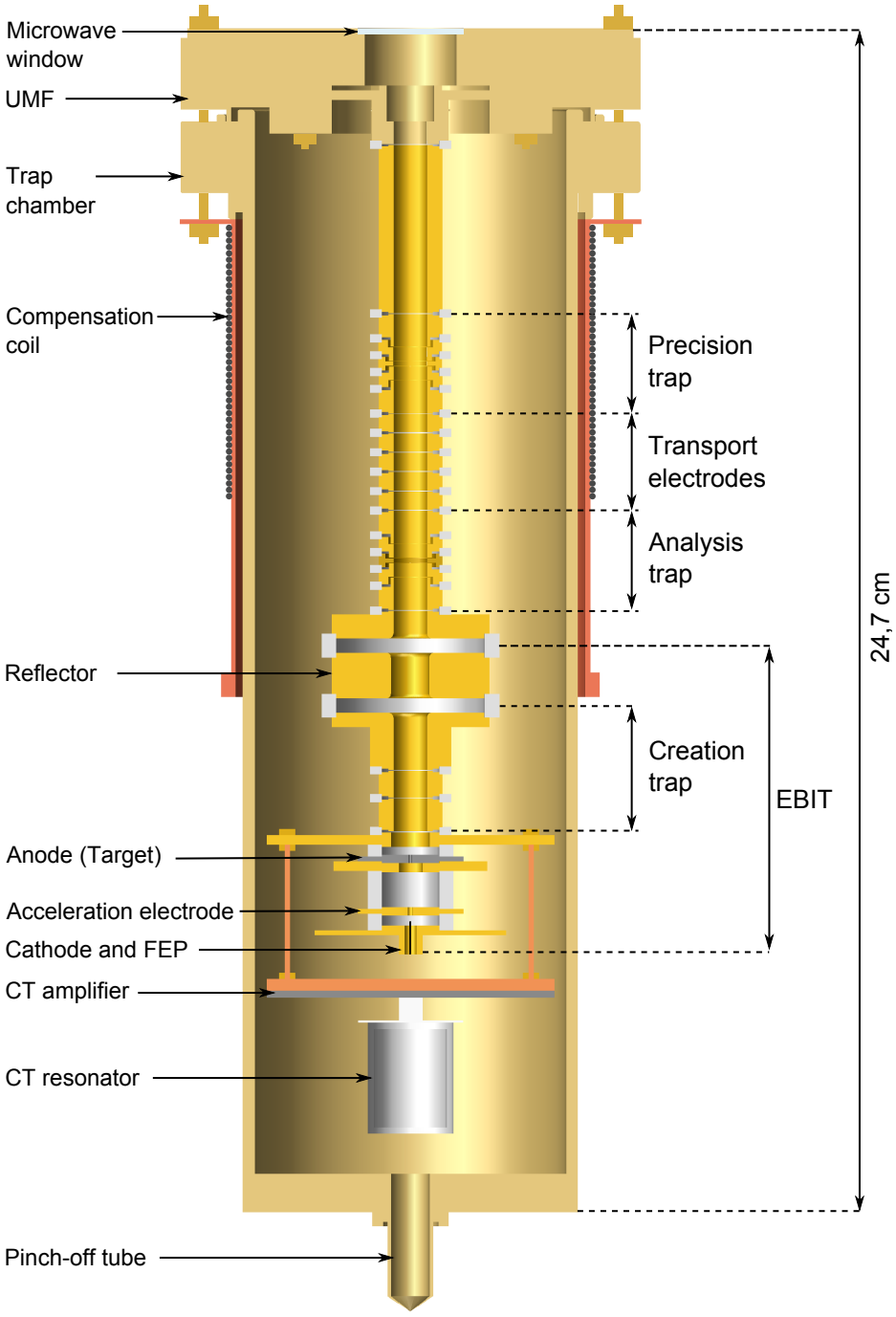

Figure 5.3: Technical drawing of the trap tower inside the hermetically sealed trap chamber. The compensation coil is mounted around the trap chamber. For clarity the cabling as well as the feedthroughs in the upper montage flange (UMF) are not shown. For more details see text.

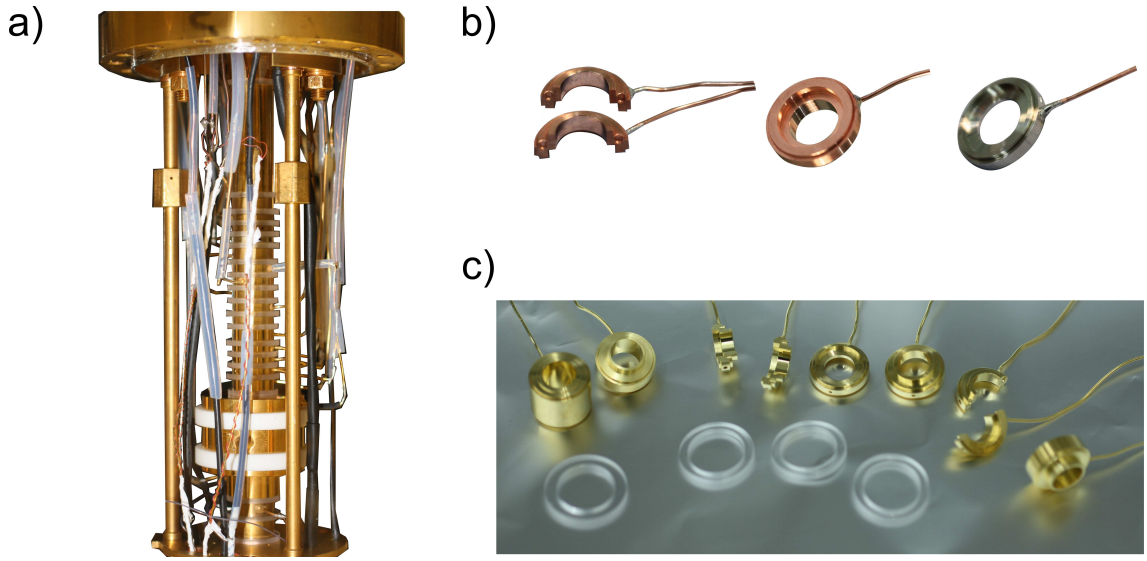

Figure 5.4: A photograph of the trap tower after cabling is shown in (a). (b) shows a split and an unsplit correction electrode as well as a nickel ring. In (c) several electrodes after gold-plating as well as some sapphire rings can be seen.

long storage times even for a single highly-charged ion. A single $^{28}Si^{13+}$ ion was stored for five month before it was lost due to technical problems.

5.2.1 Miniature EBIT

The completely closed vacuum chamber requires the in-trap production of the highly-charged ions. To this end a miniature electron-beam-ion-trap (EBIT) was designed [75]. Electrons are released from a field-emission-point (FEP). They can be accelerated up to 8 keV by a voltage applied to the acceleration electrode and are guided by the magnetic field lines. A reflector electrode is used to reflect the electrons, causing them to oscillate between reflector and FEP. Due to the Coulomb repulsion the electron beam is broadened until it hits the target, which is placed between FEP and reflector. Then, neutral atoms and singly charged ions are released from the target. The neutral atoms travel through the trap volume until they hit the electrodes or are ionized by the electron beam, which can happen in the whole region of the mini-EBIT. Those ions, which are created in the trapping region of the CT are captured and are consecutively ionized by the electron beam. An appropriate choice of the applied voltages enables the adjustment of current density and electron energy. Moreover, the duration of the charge-breeding process can be freely chosen.
A consequence of this setup is that the electron beam, which is required to produce the higher charge states, cannot be prevented to hit the target and thus atoms and ions are continuously released. Therefore, the resulting ion cloud contains not only different species

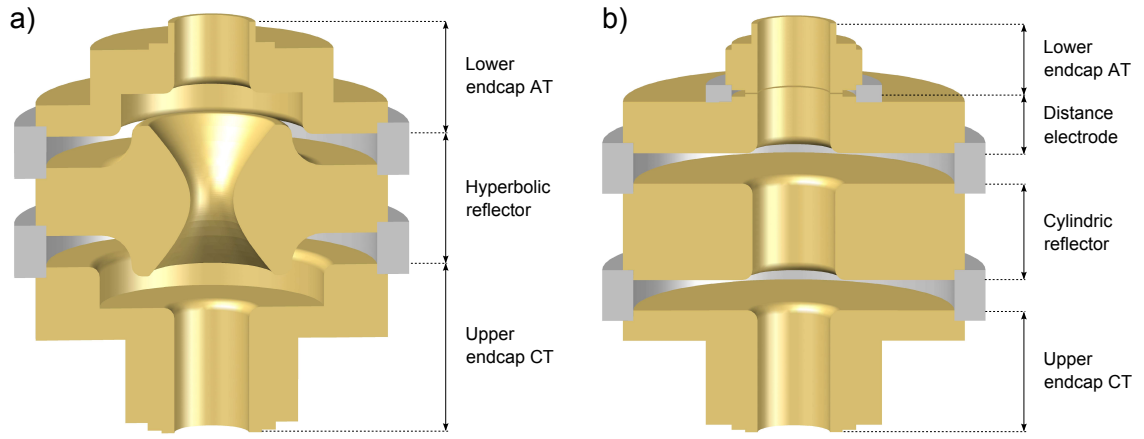

Figure 5.5: The formerly employed hyperbolic (a) and the presently implemented cylindrical (b) reflector electrodes with the corresponding adjacent electrodes are shown. The overall length is the same for both setups, but for the cylindrical design an additional distance electrode is inserted between reflector and analysis trap.

but also different charge states. The preparation of a single ion is described in chapter 7.

The reflector electrode

The reflector electrode basically has to meet two requirements:

1. During the creation process the electron beam has to be reflected to produce highly-charged ions and to prevent the electrons from hitting the microwave window at the opposite side of the trap tower.

2. Ions have to be transported from the CT through the reflector to the measurement traps.

Originally, a hyperbolically-shaped reflector electrode was employed, which turned out to fulfill neither of these requirements satisfactorily. Moreover, due to its additionally intended purpose as a mass-filter, the ions which were created within the reflector electrode experienced unstable trapping conditions during the creation process and impinged on the AT-electrodes. This is a problem as soon as there are electrically isolated patches on the surfaces (e.g. due to frozen rest gas or surface imperfections), which get charged by the ions and distort the cylindrical symmetry of the electric trapping potential. These electrostatic field errors were assumed to be one of the reasons for the fluctuations of the axial frequency in the AT, which prevented the detection of a single spin flip (see Sec. 4.2.2).
To overcome the described problems a new reflector was designed. Simulations of the electric potential, the electric gradient and the transport showed that a cylindrical shape provides

the best results concerning reflectivity of the electrons, shielding of the ions and transport efficiency. An additional distance electrode between reflector and analysis trap was implemented to minimize the number of impinging electrons on the AT-electrodes. Additionally, the inner diameter of the reflector electrode is 1 mm larger than that of the other electrodes. As a result secondary electrons created by impinging ions on the reflector and following the magnetic field lines, hit the distance electrode and thus are shielded from the measurement trap region.
With the new reflector the amount of electrons and ions passing the reflector electrode during the creation process was significantly decreased, whereas the transport efficiency was increased. It provided an important progress towards the required axial frequency stability and together with the other improvements described in Sec. 4.2.2 it finally enabled the detection of a spin flip.

Creation trap

The creation trap is required to store the ions while they are consecutively ionized. It is a simple three-electrode Penning trap since there is no need for a high harmonicity of the electric potential. The potential usually applied to the ring-electrode of the CT is in the range of $-100\,\mathrm{V}$, whereas both endcaps are kept to ground. Although there is an axial detection system for the creation trap it is not required for the ion production but was meant to investigate the charge-breeding process. Having finished the creation process, the ion cloud is immediately transported to the precision trap.

5.2.2 Precision trap

In the precision trap the high-precision measurement of the eigenfrequencies is performed while a spin flip attempt is conducted. It is placed in the homogeneous center of the superconducting magnet. In order to achieve the required harmonicity of the electric potential at the trap center, two correction electrodes are employed. The trap characteristics are summarized in Tab. 5.1. The trap is orthogonal but not completely compensated, which means that the C_4- and the C_6-term can not be eliminated for the same tuning ratio. This is no limitation for the dip- and double-dip detection techniques due to the small motional amplitudes of the ion but has to be taken into account when measuring the g-factor with the PnA-technique. Addressing the radial modes and the direct detection of the modified cyclotron frequency is accomplished by a split lower correction electrode.
The magnetic field homogeneity necessitates a gold layer without any ferromagnetic admixtures. Therefore, a pure gold layer of 1 µm was applied on a silver layer of 14 µm.

	precision trap	analysis trap
ring electrode length (mm)	0.92	0.92
correction electrode length (mm)	2.85	2.85
endcap electrode length (mm)	6.80	6.80
slit size (mm)	0.14	0.14
ring material	OFHC-copper	nickel
B_1-term (µT/mm)	13.41(23)	
B_2-term (µT/mm^2)	0.52(16)	10000(500)

Table 5.1: Characteristics of the two measurement traps. The electrodes are fabricated with tolerances of 10 µm. The B_1-term in the analysis trap is different for every axial position.

5.2.3 Analysis trap

The analysis trap is needed for the detection of the spin direction. To this end, its ring-electrode is made of nickel, which has a saturation magnetization of $M = 0.644\,\mathrm{T}/\mu_0$. Apart from that the trap is completely identical to the precision trap. Due to the ferromagnetic ring-electrode there is no need to gold-plate the electrodes with pure gold without any ferromagnetic content, but hard gold[2] can be employed. This on the one hand enlarges the eligible companies being able to perform the gold-plating and on the other hand enables a thicker gold-layer. Thus, for the AT-electrodes a hard gold layer of 5 µm in combination with a silver layer of 10 µm was employed.

Electrode preparation

The electrodes, all made of OFHC copper, are galvanically gold-plated. To prevent the gold atoms from diffusing into the copper a barrier layer of silver is used between the copper and the gold layer. In fact, the most suited material would be nickel, but is not employed since it is ferromagnetic and would result in highly unwanted magnetic inhomogeneities.
In order to achieve a surface as smooth as possible the surface of the analysis trap electrodes was carefully polished before gold-plating. This is necessary, since after manufacturing the surface of the electrodes is grooved, causing a shielding of the electric field during the galvanic gilding and thus prevents a smooth gold layer. As a result, the surface is not completely covered with gold but small areas of silver or copper are visible. Due to the different working functions of these materials the resulting patch potentials disturb the cylindrical symmetry

[2]Hard gold denotes gold containing brighteners like cobalt and/or nickel.

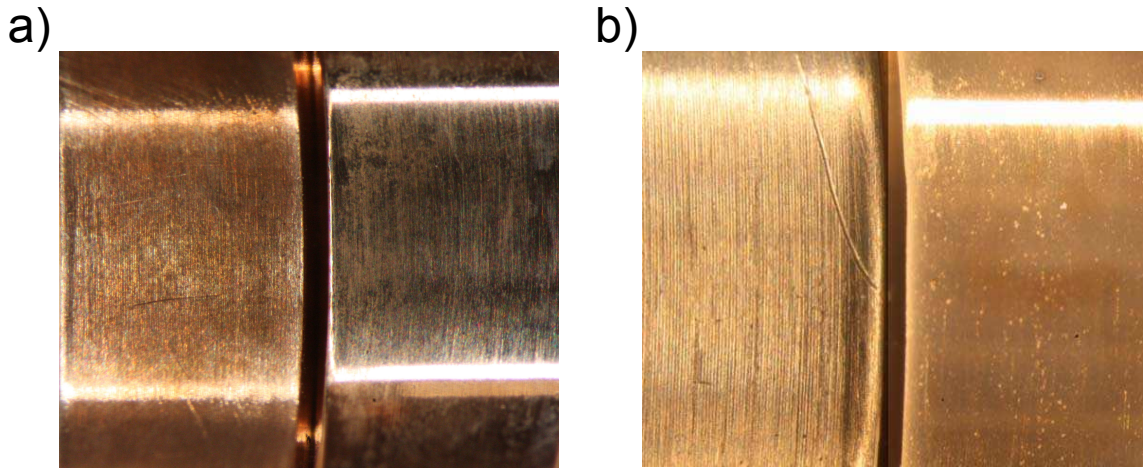

Figure 5.6: Pictures of two split electrodes before (a) and after (b) gold-plating. The surface of the left electrode is untreated after machining whereas the right electrode has been polished as described in the text.

of the electrostatic potential and prevent a high stability of the axial frequency.
The electrode surfaces are polished with "vienna polishing chalk" mixed with water. A cotton bud is fixed in a multifunction rotary tool and then the single electrodes are guided by hand until the surface is smooth. Here, particular care has to be taken for the split electrodes to avoid a rounding of the edges at the cut faces. Having finished the polishing, the electrodes are briefly cleaned with a mixture of sulphuric acid H_2SO_4 and hydrogen peroxide H_2O_2 to remove chalk residues as well as oxide layers. Afterwards they are immediately placed in distilled water to neutralize the acid. Finally, the electrodes are put in an ultrasonic bath filled with isopropanol C_3H_8O or acetone C_3H_6O. For the storage and the transport to the gold-plating company they are placed in a protective atmosphere of nitrogen gas to avoid anew oxidation of the surfaces.
With this procedure the surface of the electrodes is very smooth as can be seen in Fig. 5.6 and the symmetry of the trapping potential is improved [66]. Nevertheless, it has only been employed for the electrodes of the analysis trap since the precision trap is working very well and there was no need to replace these electrodes.

5.2.4 Transport section

The precision trap and the analysis trap are separated by five electrodes, constituting the transport section, which is required to shift the ion(s) from one trap to the other. For each g-factor measurement the ion is transported several hundred times, illustrating the importance of a reliably working transport. Moreover, it is mandatory for the measurement process that the spin orientation remains unchanged during the transport. This calls for

an adiabatic transport, which is achieved by slowly shifting the minimum of the electric potential by applying appropriate voltages to the electrodes. During the transport the voltages are ramped within 500 ms from the initial to the final value along with another 500 ms waiting time between each step. A potential depth of -14 V is used.
Formerly the transport section consisted of only two long electrodes. They, however, turned out to be the reason for transport problems, since the electric field inside an electrode, which is longer than wide almost vanishes. This implies that any imperfection on the electrode's surface shifts the center of the electrostatic potential to uncontrollable radii and might result in ion loss [61]. Therefore, the two long electrodes were exchanged against the five short ones shown in Fig. 5.3, which immediately provided a reliable transport.

5.3 Electronic components

Besides the Penning traps and the superconducting magnet many additional (mostly electronic) parts are needed to operate the experiment, which are described in this section. First, there are the custom-built detection systems, which enable the detection of a single ion. Another important device is the high-precision voltage source to provide the trapping potential, whose performance was further improved by a self-built voltage supply. In order to control the motion of the ion several excitation lines are employed. And finally, a suited microwave system is required to induce spin flips.

5.3.1 Detection systems

There are two detection systems used during this thesis: the axial detection system for the analysis trap and that for the precision trap. Both consist of a superconducting resonator, an amplifier in the cryogenic region and a second amplifier as well as a down-converter in the room-temperature region. A down-conversion of the signal to about 12 kHz is required for the analysis with the FFT-analyser SR1 from Stanford Research. The main parameters of the detection systems are summarized in Tab. 5.2.
For both resonators superconducting niobium titanium (NbTi) is used for the wire as well as for the housing to achieve high quality factors (Q-values) [73]. Experimentally, the Q-value can be determined by measuring the resonance frequency ω_0 and the 3 dB-width of the resonance $\Delta\omega_0$:

$$Q = \frac{\omega_0}{\Delta\omega_0}. \tag{5.1}$$

To provide low dielectric losses PTFE[3] is used as core material. The signal is tapped from the resonator to be amplified by a cryogenic ultra-low noise amplifier, which has been developed by Sven Sturm during his Ph.D.-thesis [61]. A detailed description of the amplifier can

[3] Polytetrafluoroethylene, commonly known as teflon.

		precision trap	analysis trap
Resonator	Resonance frequency (kHz)	712	412
	Quality factor	950	3100
	Parallel resistance (MΩ)	6.8	43
	Inductance (mH)	1.5	5.36
	SNR (dB)	12	24
Amplifier	Input capacitance (pF)	4	
	Input impedance (MΩ)	>7	
	Input voltage-noise density	$400\,\mathrm{pV}/\sqrt{\mathrm{Hz}}$	
	Input current-noise density	~ 4 fA$/\sqrt{\mathrm{Hz}}$	

Table 5.2: Characteristics of the axial detection systems for both measurement traps. For details see text.

be found in this thesis. The new amplifier constitutes a significant improvement compared to the old amplifiers and enabled a measurement at $T_z = 4.8\,K$ instead of the formerly $T_z = 60\,K$. Moreover, it improved the signal-to-noise ratio (SNR) due to its low input-related voltage noise density and the high input resistance. For the detailed specifications see Tab. 5.2.

5.3.2 High-precision voltage source

The voltage applied to the electrodes to create the electrostatic trapping potential has to be stable to $\Delta U/U \leq 2.5 \cdot 10^{-7}$ (see Sec. 4.2.2) since its fluctuations directly affect the stability of the axial frequency. Therefore, the high-precision voltage source UM1-14 [64] from *Stahl Electronics* is employed. It has ten 16-bit "fast-channels" and six 24-bit "precision-channels". The precision-channels are used for the ring- and the correction electrodes of the analysis and precision trap. They provide a voltage from 0 V to −4 V and from 0 V to −14 V for the AT and the PT, respectively. The fast-channels, having a voltage range from 0 to −14 V, are used for the transport of the ion between the traps. When ions are stored in the AT or the PT, their respective endcaps and all other electrodes are kept at ground.

It was observed [65] that the performance of the UM1-14 was limited by the stability of its supply-voltage, which has to be better than $\Delta U_{\mathrm{sup}}/U_{\mathrm{sup}} = 7 \cdot 10^{-4}$ for the required stability of the UM1-14's output voltage. Since no commercially available voltage source could fulfill

all requirement, a new voltage-supply was built with the main attention on stability, noise level and temperature dependence [65, 76]. Moreover, the voltage-supply is designed to be supplied by a single 12 V car battery to provide independence from the electric network. As a result, ground loops, noise arising from the network and, most important, ion-loss during power cuts are avoided. The dc-voltage of the battery is converted into ac-voltage by a sine-generator to be afterwards amplified by a power amplifier and a transformer. Then the voltage is commutated by a bridge rectifier and finally flattened by a filter, a choke and a voltage controller, which was also custom-built to meet the requirements. The voltage-supply provides output voltages of ± 15 V and ± 5 V with a maximum output current of 1.5 A. The achieved relative voltage stability of $\leq 2 \cdot 10^{-6}$ as well as the noise level of $34\,\mathrm{nV}/\sqrt{\mathrm{Hz}}$ and the temperature dependence of 8 ppm/K considerably exceed the requirements and enable an improved performance of the UM1-14.

5.3.3 Excitation lines

There are three different excitation lines implemented in the setup, which are denoted as dipolar-, quadrupole- and LC-excitation line.

The dipolar-excitation is connected to the lower endcap of the PT and the upper endcap of the AT. It is used to address the axial motion, namely to excite the ion for the phase-sensitive detection technique in the AT or for the recording of mass spectra. Another important application is the preparation of a single ion where the axial motion of unwanted species is excited to remove them from the trap.

The quadrupole excitation is connected to one half of the split lower correction electrode in both traps. It has to be noted that it is not a quadrupole excitation in the commonly used sense (compare for example with [77]), since no fourfold split electrode is used. This means that there are additional dipolar and a monopolar components. The quadrupole excitation is used to address the radial modes or couple them to the axial mode. Accordingly, it is employed for the direct excitation of the modified cyclotron or magnetron motion, for the double-dip technique, for cooling of the radial modes and for the PNA-technique.

The LC-excitation is capacitively (C) connected to that side of the resonator (L), which is connected to the trap electrode. It is used to change the effective temperature of the detection system and thus of the ion by the application of negative feedback or white noise on the detection systems.

The dipolar- and the quadrupole-excitation were finally identified to couple an inadmissible amount of noise into the trap being one of the reasons which prevented the detection of spin flips for quite some time. To solve this problem cryogenic switches were implemented in the course of the Ph.D.-thesis of Sven Sturm [61] to short the excitation lines in the cryogenic region when they are not required. This resulted in a significantly increased stability of the axial frequency in the analysis trap.

5.3.4 Microwave setup

The microwave system is required to produce the microwave irradiation at about 105 GHz. Therefore, in a first step the microwave syntheziser Anritsu MG3692B is employed to generate microwaves at 17.5 GHz. Its frequency is synchronized with the 10 MHz rubidium atomic clock. The OML Inc. model S10MS millimeter-wave-source module multiplies this frequency by a factor of six. The resulting 105 GHz radiation is guided by a waveguide to the hat. Here a silicon window is inserted as inlet for the microwaves into the closed apparatus, which is realized by a horn-horn transition. Inside the apparatus another waveguide is used to lead the microwaves to the UMF. Here a quartz-glass window and again a horn-horn transition provide access for the microwaves to the trap chamber.

Chapter 6

Minimization of environmental influences

Environmental conditions can significantly influence the stability of the eigenfrequencies of the ion. Accordingly, appropriate stabilization systems are an important part of a high-precision experiment [78–82] and have been designed and implemented for our experiment within this work. The parameters which have to be stabilized are the electrostatic trapping potential and the magnetic field. The stability of the trapping potential, besides the internal fluctuations of the voltage references, mainly depends on the ambient temperature of the voltage source, which changes for example due to different weather conditions or after filling of cryogenic liquids. These effects are minimized by actively stabilizing the temperature within a box around the complete experimental setup. Changes of the magnetic field can have several reasons [78, 81], which, with regard to the magnet, can basically be divided in external and internal sources. The *external magnetic field* changes due to

- fluctuations of the earth magnetic field
- electronic devices
- motion of ferromagnetic objects, like elevators for example.

Internal magnetic field changes originate from

- changes of material susceptibilities inside the bore of the magnet caused by different temperature distributions for different boil-off rates within the cryogenic reservoirs [83]
- modifications of the geometric dimensions of the magnet coils due to pressure-induced temperature changes
- variation of the suspension of the experiment due to a changing of the boil-off rate within the cryogenic reservoirs, hereby causing a movement of the ferromagnetic ring-electrode of the AT within the solenoid of the magnet

- the flux-creep effect resulting in a steady decay of the magnetic field [84, 85].

A pressure stabilization of the particular reservoirs only addresses the pressure induced changes, whereas a self-shielding compensation coil [86] around the trap chamber minimizes most of these magnetic field changes. As a result, the implementation of a compensation coil redundantized the formerly employed pressure stabilization at the present level of precision, which therefore is not described in this thesis.

The requirements as well as the realization and the performance of the respective stabilization systems for temperature and magnetic field fluctuations are described in this chapter.

6.1 Temperature stabilization

The external temperature mainly influences the axial frequency due to the temperature dependence of the high-precision voltage source UM1-14, which provides the trapping potential. Additionally, the temperature might also affect the modified cyclotron frequency by changing the position of the trap in the magnetic field of the magnet due to expansion or contraction of the suspension's material. However, no significant and especially no correlated temperature dependence of the modified cyclotron frequency could be observed in our setup and thus is not discussed in this thesis.
A temperature stabilization system has been implemented to stabilize the temperature around the experiment. This minimizes temperature-induced frequency fluctuations especially of the axial frequency as well as it reduces the measurement time loss after filling liquid cryogenics, since afterwards the settling of the temperature is sped up.

6.1.1 Requirements for the temperature stabilization

In order to determine the dependence of the axial frequency on the environmental temperature, the temperature was varied and the corresponding frequency change was measured. Fig. 6.1 reveals a strong correlation and the data analysis yielded a dependence of

$$\frac{\Delta\nu_z}{\Delta T}(\mathrm{AT}) = 0.57(1)\,\frac{\mathrm{Hz}}{\mathrm{K}} \mathrel{\widehat{=}} 1.4\,\frac{\mathrm{ppm}}{\mathrm{K}}@412\,\mathrm{kHz} \tag{6.1}$$

for the axial frequency in the analysis trap and a slightly lower relative dependence of

$$\frac{\Delta\nu_z}{\Delta T}(\mathrm{PT}) = 0.64(1)\,\frac{\mathrm{Hz}}{\mathrm{K}} \mathrel{\widehat{=}} 0.9\,\frac{\mathrm{ppm}}{\mathrm{K}}@687\,\mathrm{kHz} \tag{6.2}$$

in the precision trap. A major contribution to these measured temperature dependences can be ascribed to the high-precision voltage source UM1-14, which provides the voltages applied to the electrodes. Since the axial frequency is defined by these voltages, the temperature

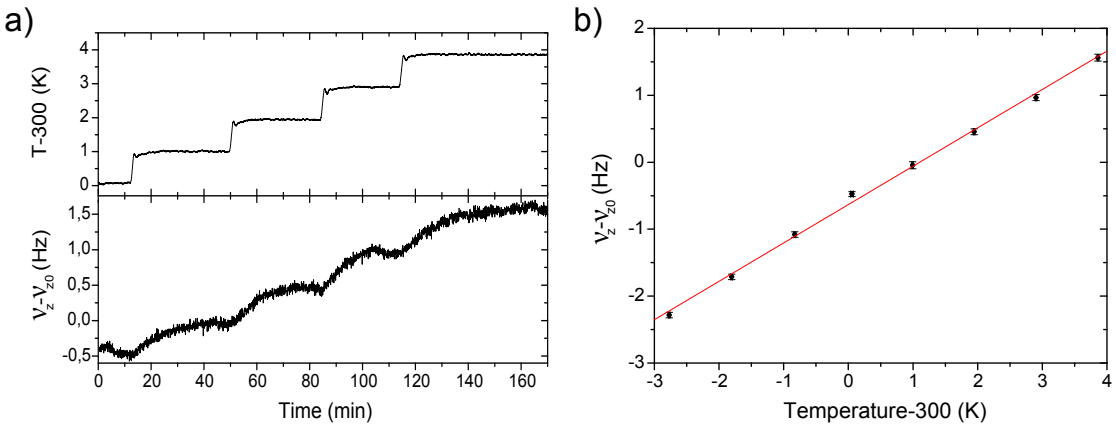

Figure 6.1: The axial frequency in the analysis trap was measured as a function of the temperature in the temperature stabilized box around the magnet (a). A linear fit (red line) to the data (b) yields a temperature dependence of the axial frequency of $\Delta\nu_z/\Delta T$=0.57(1) Hz/K.

dependence of the UM1-14 is directly reflected by the axial frequency. According to its datasheet [64], the UM1-14 has a typical temperature dependence of ±0.6 ppm/K for the PT-channels and ±0.4 ppm/K for the AT-channels.

Demanding maximum temperature induced frequency fluctuations of

$$\Delta\nu_{z,\max} = \frac{1}{4} \cdot \Delta\nu_{z,SF} = 60\,\text{mHz} \tag{6.3}$$

to enable the detection of a spin flip with nearly 100 % reliability, the environmental temperature has to be stabilized to at least $\Delta T_{\max}$=100 mK over the time scale required for the detection of a spin flip being of the order of a few minutes.

6.1.2 Setup of the temperature stabilization

To enable a temperature stabilized environment, a box starting at about half the height of the magnet encloses the setup. The upper part has to be removable in order to remove or insert the apparatus in the magnet bore and to allow to work at the setup. To this account the box is made of two parts. The lower part is permanently installed and consists of plywood boards. Holes are drilled to guide the cables into the box. The upper part is made of acrylic glass and has several closable apertures included to allow for liquid helium filling of the magnet and the cryostat as well as to provide access to the experiment for smaller changes without demounting the whole upper part.
The resistance of a PT-100 sensor (platinum resistance thermometer) is used to measure the temperature inside the box every 1.6 s. It is attached to the high-precision voltage source

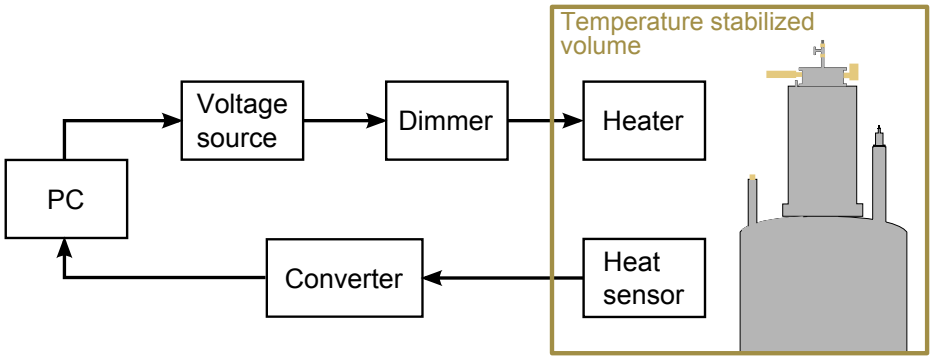

Figure 6.2: Schematic setup of the temperature stabilization system. The temperature inside the box is measured with a PT-100 and sent to the personal computer (PC). Here the controlling is performed with a *LabVIEW* program. The determined output voltage is provided by a voltage source which is connected to a dimmer. Depending on the voltage applied to the dimmer the heat power of the heater is regulated.

UM1-14, which provides the voltages applied to the electrodes and thus is the most important part to be temperature stabilized. In order to connect the PT-100 to a personal computer (PC) a "REDLAB Temp"-module from Meilhaus Electronic is used, providing eight inputs for temperature sensors as well as an USB-connector for the PC. The actual regulation is performed on the PC. Therefore, a *LabVIEW* program based on the principles of Fuzzy-logic [87] was written, which compares the measured temperature with the set temperature value and calculates an appropriate output voltage between 0 V and +10 V. This voltage is provided by a remotely controllable voltage source and applied to a dimmer, where the heater inside the box is connected to. Based on the applied voltage, the dimmer continuously regulates the heat power between "full power" and "switched off". Note, that there is no active cooling possibility since this would significantly complicate the setup.
Analogous to the commonly known PID-controller, the *LabVIEW* program has a proportional (P), an integral (I) and an derivative (D) part whose particular influence strength can be chosen by appropriate settings. These settings determine the behaviour of the regulation and have to be accurately adjusted to enable the most effective stabilization. In order to allow for an efficient regulation and especially a sufficient passive cooling, the set temperature value has to be chosen to be significantly higher than the room temperature outside the box. Therefore, usually a set point temperature of 28 °C is employed.

6.1.3 Results of the temperature stabilization

The temperature stabilization system works reliably and the regulation parameters have remained unchanged since they were adjusted. It takes about 15 min to heat the system

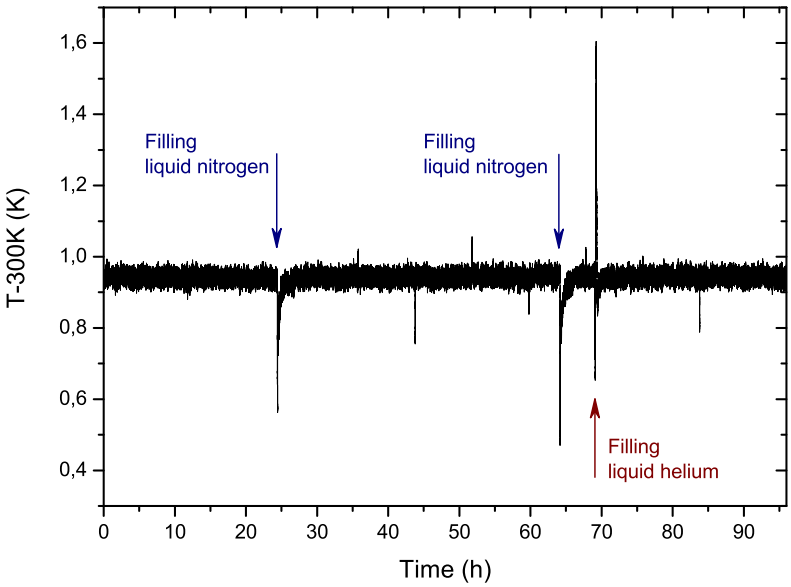

Figure 6.3: Measurement of the stabilized temperature with the temperature sensor attached to the high-precision voltage source UM1-14. After filling liquid nitrogen or helium it takes about two hours until the temperature is stabilized to the old value again.

from 24°C to 28°C. The delay between temperature and axial frequency, resulting from the required thermalization time, is of the order of 20 to 30 min, depending slightly on the absolute temperature change.

A typical measurement of the stabilized temperature measured with the sensor attached to the high-precision voltage source UM1-14 is shown in Fig. 6.3. Within this measurement period liquid nitrogen was filled two times and liquid helium one time. After filling it takes about two hours until the temperature is stabilized again. In Fig. 6.4a) a histogram of the temperature measurement over about one week is shown where the time periods during and two hours after filling are excluded. A Gaussian lineshape was fitted to the data and yielded an rms-width of σ=12.8 mK corresponding to a full-width-at-half-maximum (FWHM) of 30.1 mK over the measurement period of one week. This exceeds the requirements significantly. The Allan Deviation, calculated with the program AlaVAR 5.2 [88], shown in Fig. 6.4 also yields a stability of the temperature below 10 mK over all averaging times. The small peak at 50 s is caused by the regulation whereas the subsequent decreasing fluctuations with time represent the expected behaviour of Gaussian distributed noise without any correlation or drift.

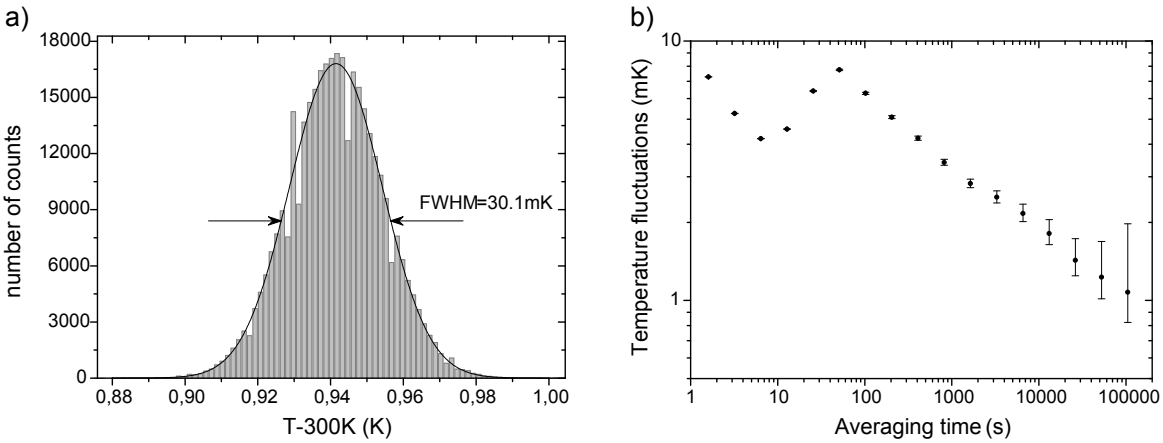

Figure 6.4: Histogram (a) and Allan deviation (b) of the stabilized temperature measured with the sensor attached to the high-precision voltage source UM1-14 during about one week without the filling periods. The time between two consecutive measurements is 1.6 s. A fit with a Gaussian lineshape to the histogram yields an rms-width of σ=12.8 mK, corresponding to a full width at half maximum (FWHM) of 30.1 mK. The Allan Deviation reveals a temperature stability beter than 10 mK over all averaging times.

6.1.4 Outlook for the temperature stabilization

The current temperature stabilization system fulfills all requirements and works reliably. Large parts of the system and especially the regulation program has been adopted by the TRIGA-Trap experiment [89]. However, if the achievable precision of the g-factor measurement is even further improved by advanced measurement techniques it might become necessary to improve the temperature stabilization system in the future. It turned out that the current setup is limited by the "REDLAB Temp"-module and its noise. Therefore, a better read-out device would already improve the performance of the stabilization system. Moreover, one could think about an active cooling system to accelerate the regulation.

6.2 Self-shielding compensation coil

Due to the simultaneous measurement of Larmor and free cyclotron frequency, the determination of the frequency ratio Γ is less sensitive towards possible drifts or fluctuations of the magnetic field. However, the finite measurement time for the free cyclotron frequency leads to a broadening of the g-factor resonance. For the double-dip-technique a measurement time of the order of 100 s is required and thus short-term fluctuations of the magnetic field are not negligible. For the PnA-technique [71] the measurement or more precisely the evolution time is only of the order of a few seconds, hereby already significantly reducing the

sensitivity towards magnetic field fluctuations. The achievable precision for a given initial phase resolution $\delta\Phi_{\mathrm{in}}$ depends on the evolution time T_{ev} [61] according to

$$\frac{\delta\nu_+}{\nu_+} \geq \frac{\delta\Phi_{\mathrm{in}}}{2\pi\cdot\nu_+}\frac{1}{T_{\mathrm{ev}}}. \tag{6.4}$$

However, the longest possible evolution time is defined by the magnetic field stability, since an unwrapping of the determined phase is not possible if phase fluctuations of the order of π occur. For the g-factor measurement of hydrogenlike silicon $^{28}\mathrm{Si}^{13+}$ [90] an evolution time of 5 s was employed yielding a relative uncertainty of $4.7\cdot10^{-11}$ for the frequency ratio Γ. In order to further improve the achievable precision, the magnetic field has to be stabilized. Magnetic field fluctuations can be shielded by implementing a self-shielding compensation coil as it was proposed and realized by G. Gabrielse and J. Tan in 1988 [86, 91]. It utilizes flux conservation in closed superconducting loops to passively compensate magnetic field fluctuations at the center of the trap and is nowadays often already included within superconducting magnets [79, 92]. We implemented the coil directly around the trap chamber, hereby also shielding fluctuations of the superconducting magnet itself.
The magnetic field fluctuations in our laboratory have been measured with a flux-gate. A typical measurement is shown in Fig. 6.5. It can be seen that the fluctuations decrease during the night from about 50 nT to 20 nT. Daily activities, e.g. moving chairs or displacing the cryogenic storage tanks, cause absolute magnetic field fluctuations of the order of 100 nT.

6.2.1 Design of the self-shielding compensation coil

The self-shielding compensation coil was designed according to the principles described in [86]. For the design, the external magnetic field and its fluctuations are considered to be parallel to the $\hat{z}$-axis of the coil, while the effect of a tilt between magnetic field and compensation coil is discussed in Sec. 6.2.4. To this end, if not marked differently, only the $\hat{z}$-component of the magnetic field is considered in the following.
The compensation coil consists of a single superconducting closed axial-symmetric solenoid as shown in Fig. 6.6a). According to Faraday's and Lenz' law the magnetic flux $\Phi = \int \mathbf{B}\cdot\mathrm{d}\mathbf{A}$ through a perfectly conducting closed loop is kept constant. To this end, if an external magnetic field $B_{\mathrm{ext}}(\rho,z)$ is applied, a current I_{c} is induced in the solenoid, which produces a magnetic field $B_{\mathrm{c}}(\rho,z)$ to achieve

$$\int_{A_{\mathrm{c}}} (B_{\mathrm{ext}}(\rho,z) + B_{\mathrm{c}}(\rho,z))\mathrm{d}A = 0. \tag{6.5}$$

Without loss of generality the conserved flux is set to zero. Employing a superconducting wire for the compensation coil, the induced current is persistent since at 4.2 K the wire has a vanishing resistance. For details of the construction see Sec. 6.2.2.
In order to shield magnetic field fluctuations the induced magnetic field $B_{\mathrm{c}}(\rho,z)$ has to

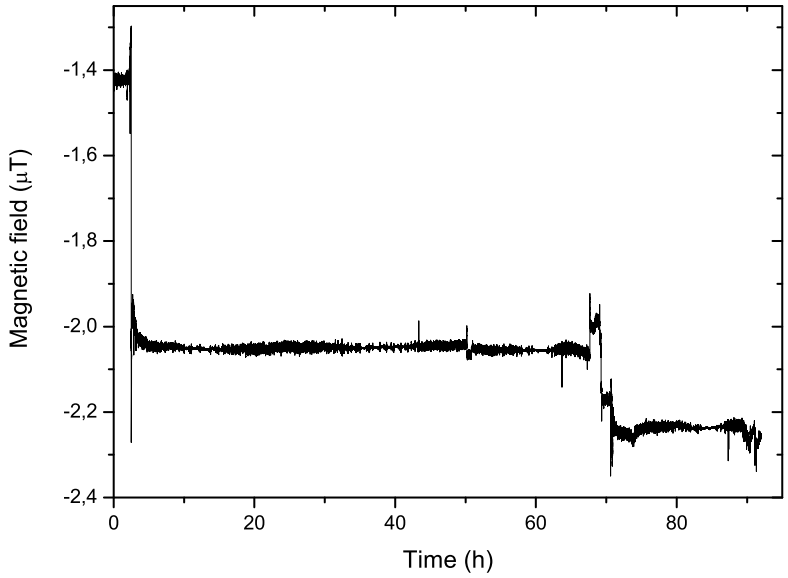

Figure 6.5: The magnetic field in the laboratory has been measured with a flux-gate. Typical daytime fluctuations are of the order of 50 nT, whereas during the night the fluctuations decrease to 20 nT. The discrete jumps originate from external distortions.

compensate $B_{\mathrm{ext}}(\rho, z)$, which can be achieved by a suitable geometry of the compensation coil. The shielding factor S at the center of the coil is given by the ratio of external and internal magnetic field at the considered position

$$S = \frac{B_{\mathrm{ext}}(0,0)}{B_{\mathrm{ext}}(0,0) + B_{\mathrm{c}}(0,0)}. \tag{6.6}$$

It is useful to consider the inverse shielding factor

$$S^{-1} = 1 + \frac{B_{\mathrm{c}}(0,0)}{B_{\mathrm{ext}}(0,0)} \tag{6.7}$$

and find $S^{-1} = 0$, corresponding to $B_{\mathrm{c}}(0,0) = -B_{\mathrm{ext}}(0,0)$, to obtain perfect shielding. The shielding factor depends on the geometry of the solenoid and thus the most suited geometry has to be determined. For the calculations the two geometry-dependent variables g_{c} and the self-inductance L_{cc} are introduced, which are related to the magnetic field at the center and the magnetic flux through the solenoid, respectively:

$$B_{\mathrm{c}}(0,0) = g_{\mathrm{c}} I_{\mathrm{c}} \qquad \text{and} \qquad \Phi = \int_{A_{\mathrm{c}}} B_{\mathrm{c}}(\rho, z) \mathrm{d}A = L_{\mathrm{cc}} I_{\mathrm{c}}. \tag{6.8}$$

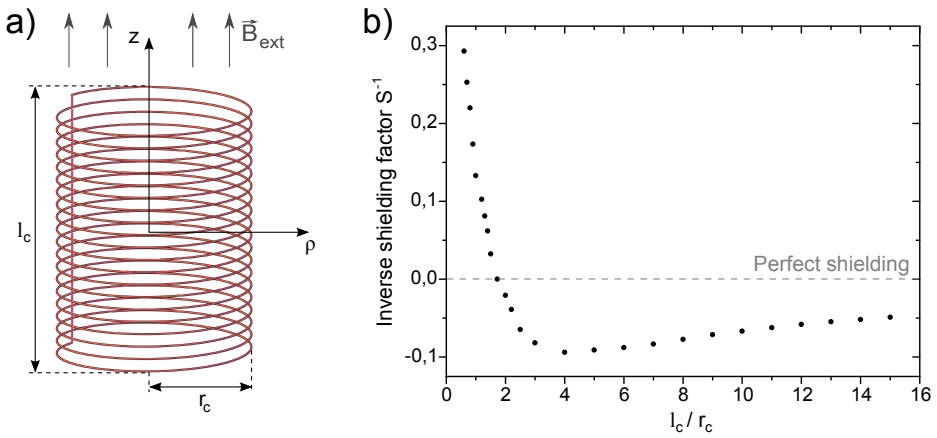

Figure 6.6: Sketch of the compensation coil (a) and the dependence of the inverse shielding factor S^{-1} on the ratio between length l_c and radius r_c of the single-layer coil, which was simulated with *COMSOL Multiphysics*. Perfect shielding is obtained for $l_c/r_c = 1.72$. For details see text.

Here, A_c is of the compensation coil.
When expanding Eq. (6.7) with $-\int_{A_c} B_{ext} dA / \int_{A_c} B_c dA = 1$, according to Eq. (6.5), the shielding factor can be expressed as

$$S^{-1} = 1 - \frac{B_c(0,0)}{\int_{A_c} B_c(\rho, z) dA} \cdot \frac{\int_{A_c} B_{ext} dA}{B_{ext}(0,0)} \tag{6.9}$$

$$= 1 - \frac{g_c A_c}{L_{cc}} \tag{6.10}$$

with the effective area

$$A_c = \frac{\int_{A_c} B_{ext} dA}{B_{ext}(0,0)} \tag{6.11}$$

depending on the spatial distribution of the external magnetic field. For a homogeneous external field and a compensation coil with radius r_c and the number of windings N_c this formular becomes

$$A_c(B_{ext} = \text{homogeneous}) = N_c \cdot \pi \cdot r_c^2. \tag{6.12}$$

If the diameter of the wire is much smaller than the length of the compensation coil l_c the current through the windings can be considered as uniformly distributed and the finite diameter of the wire can be neglected for the calculations. To calculate the shielding factor Eq. (6.10) is employed. It reduces the calculation of the shielding factor to the determination of three parameters, which only depend on the geometry of the compensation coil. Within this work *COMSOL Multiphysics* was used to simulate the compensation coil and determine g_c, A_c and L_{cc}. While the determination of g_c and A_c is straight forward according to Eq. (6.8) and Eq. (6.12), respectively, the self-inductance L_{cc} was calculated by evaluating

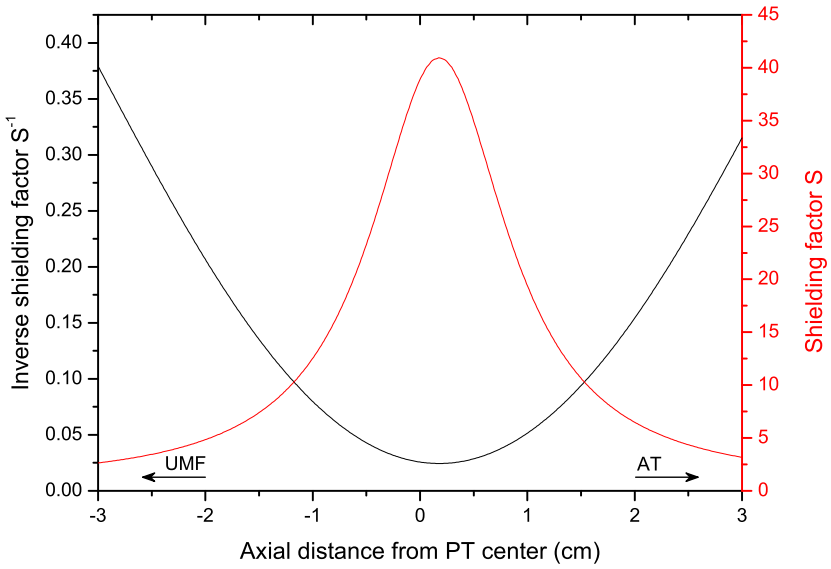

Figure 6.7: Simulation of the shielding factor of the compensation coil as a function of the axial position without considering the magnet's solenoid. A radius of $r = 3.7162\,\mathrm{cm}$ and a length of $l = 5.854\,\mathrm{cm}$ are used. At the center of the precision trap (PT) a shielding factor of $S = 39(11)$ is obtained.

the volume integral $\int_{V_\mathrm{c}} B_\mathrm{c}(\rho, z)dV$ over the volume enclosed by the compensation coil with COMSOL and dividing it by the length of the compensation coil:

$$L_\mathrm{cc} = \frac{1}{I_\mathrm{c}} \int_{A_\mathrm{c}} B_\mathrm{c}(\rho, z)dA = \frac{1}{I_\mathrm{c}} \frac{N_\mathrm{c} \int_{V_\mathrm{c}} B_\mathrm{c}(\rho, z)dV}{l_\mathrm{c}}. \tag{6.13}$$

Note that the number of windings cancels out within the calculation of the shielding factor. In order to find the geometry where perfect compensation is achieved, the dependence of the shielding factor on length-to-radius-ratio $l_\mathrm{c}/r_\mathrm{c}$ was analysed for a single-layer compensation coil in a homogeneous external magnetic field. The obtained result is shown in Fig. 6.6b) and yields a perfect shielding at the center of the solenoid for $l_\mathrm{c}/r_\mathrm{c}$=1.72.
For our setup, the radius of the compensation coil is determined by the trap chamber and thus is fixed to $r_\mathrm{c} = 37.3\,\mathrm{mm}$. Consequently, the ideal length would be $l_\mathrm{c} = 64.16\,\mathrm{mm}$. However, due to the UMF and the 77 K-shield, the available space above the precision trap is strictly limited, implying that the perfect geometry cannot be achieved. In fact the compensation coil with ideal l/r-ratio would have its center about 4.5 mm below the center of the precision trap. In other words, a compensation coil centred around the precision trap allows for a maximum length of 54.98 mm, corresponding to $l_\mathrm{c}/r_\mathrm{c} = 1.47$ and a shielding

factor of $S = 24$.
In order to find the optimum length-to-radius-ratio for a maximized shielding factor at the position of the PT-ring electrode, which is not necessarily identical to the center of the compensation coil, the shielding factor at this position was analysed for $r_c = 37.162\,\mathrm{mm}$ and varying length. For both, length and radius the thermal contraction between 300 K and 4.2 K has to be considered within the calculations. Finally, a length of l_c =58.54 mm was determined to yield a shielding factor $S = 39(9)$ at the center of the precision trap (see Fig. 6.7). The uncertainty was estimated by assuming an uncertainty for

- the axial position: $\delta z_c = 3\,\mathrm{mm} \quad \widehat{=} \quad \delta S = 7$
- the radius: $\delta r_c = 0.5\,\mathrm{mm} \quad \widehat{=} \quad \delta S = 4$
- the length: $\delta l_c = 0.5\,\mathrm{mm} \quad \widehat{=} \quad \delta S = 3$

of the compensation coil and simulating the corresponding difference of the shielding factor.

This calculation has to be extended by considering the solenoids of the superconducting magnets. The mutual interaction between these solenoids and the compensation coil alters the shielding factor and therefore has to be taken into account. However, we neither know the exact position of the magnet's solenoids nor their geometry. Accordingly, both had to be estimated from a technical drawing and thus constitutes an uncertainty for the obtained results of the simulations.
To extend the calculations to more than one axial-symmetric solenoid, the corresponding variables g_i and A_i of solenoid i are written in column vectors while the inductance becomes the symmetric inductance matrix $\boldsymbol{L}$ with the self-inductances L_{ii} as diagonal elements and the mutual inductances $M = L_{ij}$ as off-diagonal elements. The shielding factor then reads

$$S^{-1} = 1 - \mathbf{g}^T \mathbf{L}^{-1} \mathbf{A}. \tag{6.14}$$

For the simulations performed in this thesis only the main solenoid of the magnet is considered, since no information about the additional shim-coils is available. Accordingly, the system consists of two solenoids: the compensation coil with radius r_c, length l_c and number of windings N_c and the magnet solenoid being characterized by r_M, l_M and N_M. For this

system, the shielding factor is calculated to

$$\begin{aligned} S^{-1} &= 1 - \left[\begin{pmatrix} g_\mathrm{c} & g_\mathrm{M} \end{pmatrix} \begin{pmatrix} L_\mathrm{c} & M \\ M & L_\mathrm{M} \end{pmatrix}^{-1} \begin{pmatrix} A_\mathrm{c} \\ A_\mathrm{M} \end{pmatrix} \right] \\ &= 1 - \frac{1}{\det(\mathbf{L})} \left[\begin{pmatrix} g_\mathrm{c} & g_\mathrm{M} \end{pmatrix} \begin{pmatrix} L_\mathrm{M} & -M \\ -M & L_\mathrm{c} \end{pmatrix} \begin{pmatrix} A_\mathrm{c} \\ A_\mathrm{M} \end{pmatrix} \right] \\ &= 1 - \frac{L_\mathrm{c} L_\mathrm{M}}{L_\mathrm{c} L_\mathrm{M} - M^2} \left[\frac{A_\mathrm{c} g_\mathrm{c}}{L_\mathrm{c}} + \frac{A_\mathrm{M} g_\mathrm{M}}{L_\mathrm{M}} - \frac{M}{L_\mathrm{c} L_\mathrm{M}} (g_\mathrm{c} A_\mathrm{M} + g_\mathrm{M} A_\mathrm{c}) \right]. \end{aligned} \tag{6.15}$$

The parameters g_i, A_i and L_ii, with i representing the solenoid and the magnet, respectively, are determined simultaneously as described above for the single compensation coil. The mutual inductance M_ij is obtained in a similar way as the self-inductance:

$$M_\mathrm{ij} = \frac{N_\mathrm{i} \int_i B_\mathrm{j}(\rho, z) dV}{l_\mathrm{i} I_\mathrm{j}}. \tag{6.16}$$

For this system the simulation of the implemented compensation coil and magnet solenoid yielded a shielding factor of S_total=286(9)(10). Here, the first and second uncertainty are the uncertainties due to compensation coil and magnet, respectively. The second one was estimated in a similar way as for the compensation coil by varying

- the axial position: $\delta z_\mathrm{M} = 10\,\mathrm{mm} \;\widehat{=}\; \delta S = 10$
- the radius: $\delta r_\mathrm{M} = 10\,\mathrm{mm} \;\widehat{=}\; \delta S = 1$
- the length: $\delta l_\mathrm{M} = 1\,\mathrm{mm} \;\widehat{=}\; \delta S = 1$

of the magnet's solenoid within the simulations. The additional shim coils constitute an unknown uncertainty. Moreover, within the simulations the magnet's solenoid was considered to be a single-layer coil, which most likely is not the case in reality.
An increase of the shielding factor is expected since the solenoid of the magnet has a shielding factor itself. We measured the shielding factor of our superconducting magnet to be $S_\mathrm{M} = 6.7(1.3)$, which is very similar to shielding factors of other NMR-magnets [91] and which fits well to the simulated difference between the simulation of the compensation coil and the simulation, which includes the magnet's solenoid.

6.2.2 Construction of the compensation coil

The construction process of the compensation coil is illustrated on the photographs in Fig. 6.8. The coil is single-layer wound on a cylindrical copper holder. This holder aligns the compensation coil to the trap chamber by adjusting the inner diameter of the holder to the outer diameter of the trap chamber. At its top, four plates are used to screw the compensation coil to the UMF. A 195 µm diameter FORMVAR insulated NbTi wire of 170 µm

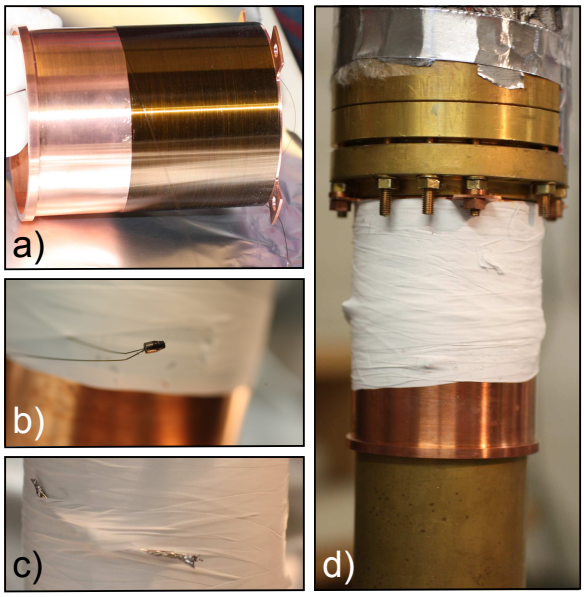

Figure 6.8: Photographs of the compensation coil. a) Single-layer winding of the NbTi-wire on the copper holder. b) The two ends of the wire are connected by a superconducting joint. c) A small part of the wire is wrapped around a 5 kΩ quench-resistor. d) The finished compensation coil is mounted around the trap chamber and screwed to the UMF. For stabilization and protection purposes teflon-tape is wrapped around the windings. For further details see text.

conducting diameter is employed. The windings are fixed with epoxid resin and afterwards covered with teflon tape.

Superconducting joint

The most critical part of the compensation coil turned out to be the superconducting joint. The two ends of the wire of the coil had to be connected to form the required closed loop. The variety of suited bonding materials is especially limited by the fact that the joint has to be superconducting while positioned within the 3.764-T field of the magnet. For superconducting magnets, which also require superconducting joints for its solenoids, the joint can be positioned outside the solenoids and thus does not experience the strong magnetic field. The task to achieve a superconducting joint is moreover complicated by the missing opportunities to properly test the joint. First tests of the joint were performed by placing it in liquid helium and measuring the resistance via a four-wire technique. However, this is limited by the resolution of the multimeter. Accordingly, the only reliable test parameter is the performance of the compensation coil itself. This, in turn, requires the possibility to measure the magnetic field inside the compensation coil at a temperature of 4.2 K. To this

end we built a small flux-gate, which we positioned in the center of the coil to measure the magnetic field change when applying an external magnetic field. The required cryogenic temperatures were provided by a pulse-tube cooler [93]. But, despite all efforts this did not provide reliable results and thus we could not test the compensation coil until we implemented it in the experiment and used the ion or to be more precise the cyclotron frequency of the ion as a highly-sensitive magnetic-field probe.
Several approaches to realize a superconducting joint were tested, which failed due to different reasons:

- Spot-welding melted the wires,
- Cold-welding of the twisted wires broke the wires,
- Cold-welding of parallel wires did not achieve a proper connection of the wires,
- Employing magnesium diboride[1] (MgB_2) powder. Here, the MgB_2-powder was enclosed in a small copper tube and after putting the dismantled wires into it, the copper tube was closed and compressed strongly to obtain a junction between the wires and the powder. After first promising results the method was found to be unreliable.

Finally, a reliable technique was developed in cooperation with the workshop of the University of Mainz:

- A hole drilled in a small plain cylinder of NbTi serves as guidance for the two wires which are inserted through. At the outlet of the cylinder the two wires were plasma welded to the cylinder, hereby connecting the NbTi-wires to the NbTi-cylinder.

With this technique a joint was realized, which is mechanically stable and shows a resistance below the resolution of the multimeter used for the four-wire measurement. Accordingly, this technique was employed for the joint of the compensation coil and, after implementation of the compensation coil in the experiment, the joint proved to be superconducting.

Quench resistor

It might become necessary to reset the current of the superconducting compensation coil when for example the magnetic field has drifted so far that the compensation coil cannot compensate the drift any more. To this account a quench resistor was implemented. A 5 kΩ-resistor is used, where the NbTi-wire of the coil is closely wrapped around several times. Applying a current to the resistor allows to heat the wrapped part of the wire above the critical temperature of the superconductor. If part of the wire is not superconducting but

[1] MgB_2 is a type-II superconductor with a critical temperature of $T_c = 39\,\mathrm{K}$ and a critical field of $H_c > 10\,\mathrm{T}$ at 4.2 K [94].

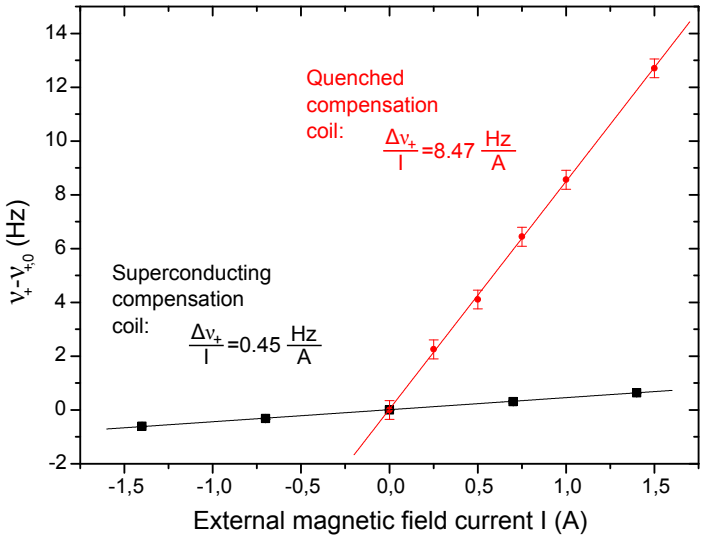

Figure 6.9: In order to determine the shielding factor S of the compensation coil, the dependence of the modified cyclotron frequency ν_+ in the PT on an external magnetic field is measured once while the coil is superconducting (double-dip technique) and once while it is quenched (PnA-technique). The error bars for the superconducting coil are smaller than the data points due to the (required) increased measurement precision, which was achieved with the PnA-technique. The strength of the external magnetic field is characterized by the current I applied to the employed magnetic field solenoid. Comparing the two resulting slopes yields a shielding factor of $S = 19$ for the precision trap, with a negligible uncertainty.

normal resistive, the resistance increases significantly and the stored current is dissipated as heat. This process is commonly denoted as a *quench*. When the temperature of the wire is cooled below the critical temperature after the quench, the wire enters the superconducting phase again. This is then the new equilibrium state where no current is stored in the compensation coil, which means that the entire compensation capability is available again.

6.2.3 Experimental results of the compensation coil

As a first test we measured the shielding factor, hereby simultaneously testing the superconducting joint and the overall design. Knowing that the compensation coil was operative, we tested the quench mechanism and finally, investigated the effect on the magnetic field stability seen by the ion. Here, however, the most significant test will be the presently ongoing g-factor measurement on $^{12}C^{5+}$ with an expected uncertainty of a few parts in 10^{11}.

Shielding factor

To measure the shielding factor an external magnetic field was applied and the corresponding change of the free cyclotron frequency of the ion inside the precision trap was measured. To generate the external magnetic field, a solenoid is placed below the superconducting magnet and the value of the applied current to this solenoid is used as a measure of the magnetic field strength. A comparison between the magnetic field change while the compensation coil is superconducting (operative) with the change while the compensation coil is quenched (inoperative) yields a shielding factor of S=19 (see Fig. 6.9) with a negligible uncertainty. Note that this is the shielding of the compensation coil only without considering the magnet. The shielding factor of the magnet itself was measured to be $S_{\mathrm{M}} = 6.7(1.3)$, by calibrating the external magnetic field of the additional solenoid with an NMR-probe and comparing these values to the magnetic field change seen by the ion. Accordingly, the overall shielding factor of magnet and compensation coil is $S_{\mathrm{total}} = 127.3(1.3)$. The deviation from the simulated shielding factor can be explained by the various uncertainties in the simulations as well as in the realization of the compensation coil. In addition to the uncertainties discussed in Sec. 6.2.1 especially the neglected additional shim coils of the magnet and the possible remaining finite resistance of the superconducting joint constitute an unknown uncertainty. Moreover, the additional external field, which has been applied for testing purposes cannot be considered to be homogeneous, which, however, has been an assumption for the calculation of the compensation coil. As discussed in [91] this can also influence the measured shielding factor.
Despite all difficulties a shielding factor of 19 was obtained, which constitutes a reduction of the magnetic field fluctuations of more than one order of magnitude and thus is a significant improvement towards an increased precision of the g-factor measurement (compare also Sec. 6.2.3).
The shielding factor was also measured in the analysis trap with the same method as described for the precision trap. Here, as expected, almost no shielding is observed ($S_{\mathrm{AT}} = 1.1$).

Quench

The minimum power required for a quench of the compensation coil was measured to be 3 mW, which can be neglected regarding the helium consumption compared to the overall thermal load of several 10 mW [73]. Afterwards, the quench itself was tested by measuring the magnetic field with and without 3 mW applied to the quench resistor. It works reliably and it takes only seconds to quench the coil as well as to enter the superconducting phase again.

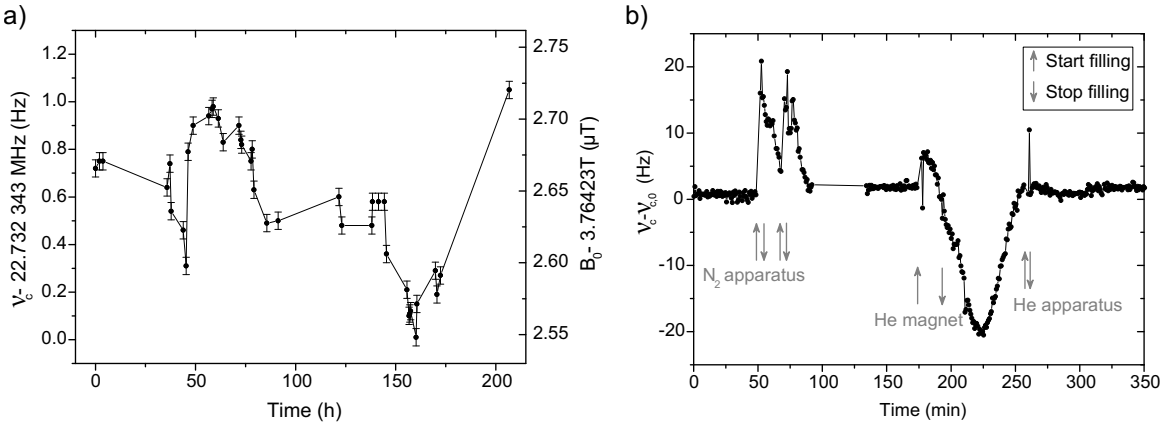

Figure 6.10: In (a) the free cyclotron frequency and hereby the magnetic field has been measured for more than one week. The peak-to-peak fluctuations of only 150 nT demonstrate the effect of the compensation coil on the longterm stability of the magnetic field. In (b) the influence of filling liquid nitrogen (N_2) and liquid helium (He) on the free cyclotron frequency was analysed with a lower resolution than in (a). During filling the system is exposed to extreme pressure and temperature changes, which cannot be compensated by the compensation coil (for more details see text). When the situation has settled down the compensation coil compensates the magnetic field to the same value as before the filling.

Magnetic field stability

The main motivation of the compensation coil was the reduction of the magnetic field fluctuations in the precision trap and thus the improvement of the free cyclotron frequency stability. The influence on the stability as well as the performance during filling cryogenic liquids was analysed. The measurement of the free cyclotron frequency over a time period longer than one week (see Fig. 6.10a)) reveals peak-to-peak fluctuations of the magnetic field of only 150 nT, corresponding to a relative change of $4 \cdot 10^{-8}$ in eight days.
In Fig. 6.10b) the free cyclotron frequency has been measured during filling liquid nitrogen and helium. To enable short measurement intervals positive feedback was employed and the averaging time was decreased, resulting in a lower resolution than presented in Fig. 6.10a). During filling, the whole experiment is exposed to extreme pressure and temperature changes, which mechanically alter the setup or the magnet or both of them. As a result the geometry of the compensation coil or even the magnetic field itself are modified implying that the corresponding magnetic field fluctuations cannot be compensated by the compensation coil. However, as soon as the situation is settled down (< 1 h) the magnetic field is stabilized again.
As already mentioned, the achievable precision with the PnA-technique was limited by the evolution time due to the magnetic field fluctuations. For the g-factor measurement of

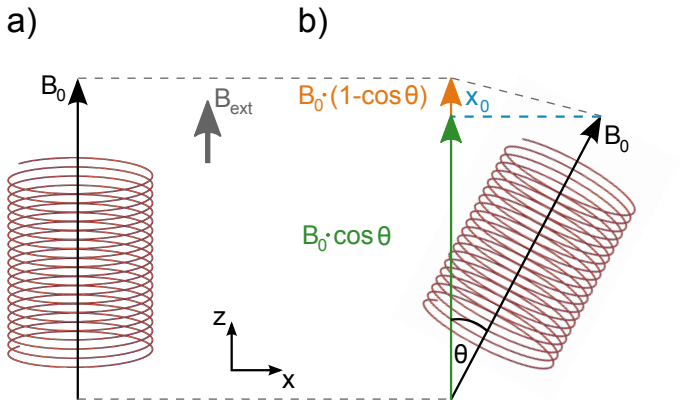

Figure 6.11: The magnetic field in the compensation coil parallel to the external magnetic field B_{ext} is B_0 (a). If the coil (or the external magnetic field) is tilted by the angle θ, the compensation coil produces an (additional) magnetic field in the $\hat{z}$-direction of $B_0(1-\cos\theta)$ in order to keep the $\hat{z}$-component of the magnetic field constant.

$^{28}Si^{13+}$ with the PnA-technique a maximum evolution time of 5 s was utilized yielding a g-factor resonance with a FWHM of $8 \cdot 10^{-10}$ and a relative uncertainty of the final frequency ratio[2] of $\delta\Gamma/\Gamma = 4.7 \cdot 10^{-11}$ [61,90]. Due to the compensation coil the evolution time could be increased to 10 s, which corresponds to a possible improvement of the precision for the modified cyclotron frequency measurement by a factor of two, provided that the remaining magnetic field fluctuations during the measurement time are averaged out. Accordingly, the compensation coil potentially enables an increased precision for the g-factor measurement being especially important for the current $^{12}C^{5+}$ measurement, which aims for a significant improvement of the electron mass uncertainty. This presently ongoing g-factor measurement will reveal the achievement of the compensation coil.
Another very important and pleasant result is the fact that the influence of pressure fluctuations on the modified cyclotron frequency can be neglected at the present level of precision, since the resulting magnetic field changes are compensated by the compensation coil. This means, that no pressure stabilization is required for neither of the four cryogenic reservoirs, hereby considerably simplifying the setup.

6.2.4 Limitations of the compensation coil - A tilted coil

The only significant effect on the modified cyclotron frequency was detected when the outlet of the liquid nitrogen reservoir of the apparatus was mechanically moved. It is assumed that this is related to a tilt of the compensation coil with regard to the external magnetic field

[2]The overall uncertainty of the g-factor itself has not been improved since already the double-dip measurement to $\delta g/g = 5 \cdot 10^{-10}$ was limited by the uncertainty of the electron mass [16].

and the resulting uncompensated transverse components. Assuming a tilt, there are two aspects which have to be considered:

- an initial and constant tilt of the compensation coil due to a tilted implementation of coil and/or the whole apparatus with regard to the magnetic field. Moreover, the external magnetic field might not be exactly parallel to the magnet's bore
- a fluctuating tilt caused by vibrations, which e.g. mechanically move the apparatus with respect to the magnet.

It is assumed that we observe a combination of both aspects. An initial tilt due to a misalignment would not affect the magnetic field stability as long as it remains constant. However, ground vibrations, for example due to construction work in the vicinity of our laboratory, result in a fluctuation of the tilt, which, at least in combination with the initial tilt, might affect the magnetic field.

In order to estimate the effect of a tilt on the magnetic field stability the consequences of a tilted compensation coil on the magnetic field seen by the ion are considered: If the axis of the compensation coil is parallel to the external magnetic field and no magnetic field fluctuations have been occurred so far the fields read

$$\boldsymbol{B}_{\text{ext}} = \begin{pmatrix} 0 \\ 0 \\ B_0 \end{pmatrix} \qquad \text{and} \qquad \boldsymbol{B}_{\text{c}} = \begin{pmatrix} 0 \\ 0 \\ 0 \end{pmatrix}. \tag{6.17}$$

To introduce a tilt θ between external magnetic field and compensation coil, we use, without loss of generality, the reference system of the compensation coil and consider the external magnetic field to be tilted. According to Faraday's law the compensation coil keeps the magnetic field in the coil constant by generating a magnetic field in the $\hat{z}$-direction of $B_{\text{c}} = B_0 - B_0 \cos\theta = B_0(1-\cos\theta)$ (see Fig. 6.11b) but cannot compensate the $\hat{x}$-component of the magnetic field:

$$\boldsymbol{B}_{\text{ext}} = \begin{pmatrix} B_0 \sin\theta \\ 0 \\ B_0 \cos\theta \end{pmatrix} \qquad \text{and} \qquad \boldsymbol{B}_{\text{c}} = \begin{pmatrix} 0 \\ 0 \\ B_{\text{c}} \end{pmatrix}. \tag{6.18}$$

As a result the magnetic field strength amounts to

$$|\boldsymbol{B}_{\text{tilt}}| = |\boldsymbol{B}_{\text{ext}} + \boldsymbol{B}_{\text{c}}| = B_0 \sqrt{\sin^2\theta + 1} \tag{6.19}$$

$$\approx B_0 \left(1 + \frac{\theta^2}{2}\right). \tag{6.20}$$

The small angles of $< 2\,\text{deg}$, which are considered, allow for the approximations made in the last step. Accordingly, the magnetic field changes by

$$\frac{\delta B}{B} = \frac{\theta^2}{2}. \tag{6.21}$$

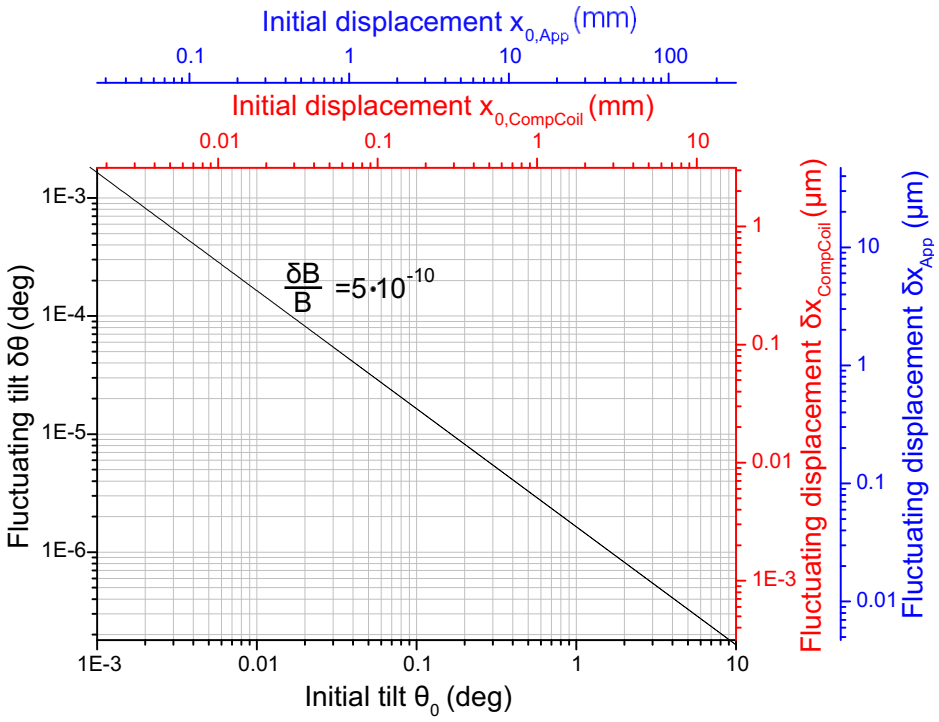

Figure 6.12: Calculated correlation of an initial (constant) tilt θ_0 and an additional fluctuating tilt $\delta\theta$, where the resulting angle is a combination of both ($\theta = \theta_0 + \delta\theta$). For details of the calculation see text. The fluctuating tilt is plotted as a function of the initial tilt for relative magnetic field fluctuations of $\delta B/B = 5 \cdot 10^{-10}$ (black line). The red and blue axis show the corresponding displacement of the bottom of the compensation coil holder and apparatus, respectively (compare Fig. 6.11).

In order to cause magnetic field fluctuations of $\delta B/B = 5 \cdot 10^{-10}$ the tilt fluctuations have to be $\delta\theta = 1 \cdot 10^{-3}$ deg. This corresponds to a fluctuation of the lower bottom of the apparatus (l_{App}=1.5 m) of 34 µm, which is assumed to be very unlikely. This is confirmed by observations at the experiment to measure the g-factor of the proton. There, formerly a pulse-tube cooler was employed to provide the cryogenic temperatures. This pulse-tube cooler was connected to the apparatus and vibrated actively, hereby causing fluctuations of the trap tower of about 20 µm [95, 96]. Since we do not have any vibrating device connected to the experiment we do not assume to have vibrations in this order of magnitude. Moreover, the experiment is located in the basement of the building and there is no railway or tram in the vicinity or any other facility which might cause ground vibrations of this magnitude. However, taking into account that the tilt is most likely the sum of an initial and constant tilt θ_0, which might be considerably large, and a small fluctuating tilt $\delta\theta(t)$, the magnetic

field fluctuations become more sensitive towards the tilt fluctuations:

$$\frac{\delta B_0}{B_0}(t) = \frac{(\theta_0 + \delta\theta(t))^2}{2} = \frac{\theta_0^2 + 2\theta_0\delta\theta(t) + \delta\theta(t)^2}{2} \tag{6.22}$$

$$\approx \theta_0\delta\theta(t) + const. \tag{6.23}$$

Since, we do not know neither θ_0 nor $\delta\theta$ we have to make several assumptions for the initial tilt θ_0 to analyse the impact of $\delta\theta$.
As a first approach one can use the tilt between the magnetic field and the axis of the electrostatic trapping potential of $\theta_0 = 0.15\,\mathrm{deg}$ (Sec. 8.4.3), which was measured via the eigenfrequencies of the ion. Although this tilt can be caused by various reasons, which might not be related to a tilt of the compensation coil it can serve as a first indication. With this initial tilt fluctuations of the apparatus of the order of 200 nm would cause magnetic field fluctuations of $5 \cdot 10^{-10}$ (compare Fig. 6.12).
As a second approach one can estimate the maximum possible elongation of apparatus and coil. To this end we assume that

- the magnetic field is parallel to the bore of the magnet,
- the apparatus is elongated by 5 mm at its bottom, corresponding to an angle of 0.2 deg,
- the compensation coil holder is inclined by 1.5 mm, which is the difference between outer radius of the trap chamber and inner radius of the compensation coil holder, corresponding to an angle of 0.9 deg.

In the worst case both misalignments add, resulting in an overall initial tilt of θ_0=1.1 deg. In this case, fluctuations of the apparatus of the order of 30 nm would cause magnetic field fluctuations of $5 \cdot 10^{-10}$ (compare Fig. 6.12). However, this is a very liberal estimation of the tilt, which is employed to provide an upper limit of the effect.
In order to overcome this possible limitation of the axial compensation coil and to shield the transverse components of the magnetic field changes it is planned to implement two additional transverse compensation coils around the present axial compensation coil. The design of these transverse compensation coils is currently under progress by Florian Köhler and is part of his Ph.D.-thesis [97].

6.2.5 Future possibilities to further reduce magnetic field fluctuations

The design and the realization of the compensation coil demonstrated that this technique can be successfully applied to our setup although the available space is strictly limited. Moreover, we succeeded in achieving a joint which proved to be superconducting. By implementation of the compensation coil we achieved an additional suppression of magnetic field fluctuations by a factor of 19, hereby increasing the achievable precision of the modified

cyclotron measurement by a factor of two due to the longer evolution time. This has the potential to determine the g-factor with the PnA-technique to a precision of a few parts in 10^{11}.

Since it is assumed that the remaining fluctuations might come from a tilt due to vibrations of the apparatus, the design of additional radial compensation coils is currently under progress. This is part of the Ph.D.-thesis of Florian Köhler [97].

One could additionally think about decoupling the experiment from ground vibrations by placing it on a vibrationally isolated and stabilized platform. This is, however, not only very expensive but, even more important, requires to move the magnet. This involves quite some risk for the magnet, which either has to be discharged or moved while being charged. Both options one would like to avoid.

To further shield external magnetic field fluctuations a pair of Helmholtz-coils could be placed around the magnet, whose current is permanently adjusted according to the measured value in the laboratory. Such a system has been realized for example at the UW-PTMS experiment [79] and at the PENTATRAP-experiment in Heidelberg [98].

Chapter 7

Preparation of the g-factor measurement

Before starting a g-factor measurement several preparative measurements have to be performed, which are subject of this chapter. First of all, the desired ion species has to be created and afterwards a single ion has to be isolated. For both, the analysis trap (AT) and the precision trap (PT) the electrostatic potential has to be optimized and the eigenfrequencies have to be measured. Moreover, the axial frequency stability in the AT has to be optimized to allow for the detection of a spin flip and finally, the Larmor frequency has to be determined in order to achieve the highest possible spin flip rate. These measurements constitute the largest part of the experimental work, whereas the final g-factor measurement runs entirely automated, being PC-controlled and synchronized by a self-written *LabVIEW* program. Furthermore, these preparative measurements usually take more time than the actual g-factor measurement itself - at least if they are performed for the particular ion species for the first time. As soon as the creation parameters are known and the trapping voltages as well as the eigenfrequencies are precisely measured, the whole creation and preparation process can be achieved within a few days, which might become necessary when the ion gets lost. In this chapter, the preparative measurements are presented in the same order as they are performed within experimental reality.

7.1 Ion creation

The trap tower is placed in a completely closed trap chamber, which necessitates the production of ions within this chamber. Accordingly, the first step towards a g-factor measurement is the creation and preparation of a single ion of the desired species, which is in this thesis lithiumlike silicon $^{28}Si^{11+}$. The mini-EBIT [75], described in Sec. 5.2.1, is employed to produce the ions. For the charge-breeding of $^{28}Si^{11+}$ an ionization energy of $\sim 0.5\,\mathrm{keV}$ is

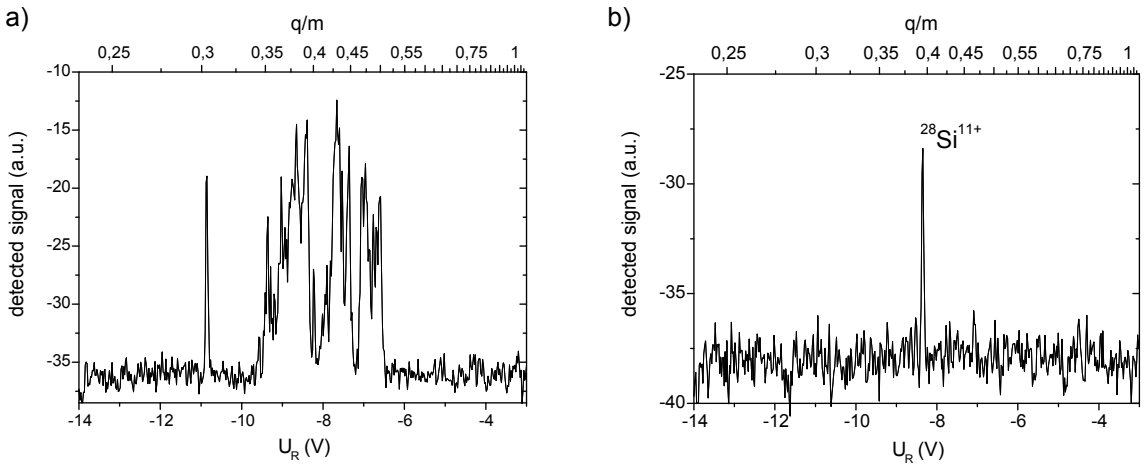

Figure 7.1: Mass spectra of an ion cloud after the creation process (a) and after cleaning (b) where only the ion species $^{28}Si^{11+}$ is left. By ramping the ring voltage U_R, ion species with different charge-to-mass-ratio q/m are brought into resonance with the detection system at different times during the voltage ramp.

required, being far below the maximum energy of 8 keV of the mini-EBIT. The electron beam was turned on for about 7 s. A voltage of 100 V was applied to the creation trap to store the ions. After the creation process an ion cloud, which contains many different species and charge-states is stored in the creation trap. This ion cloud is then transported to the PT to prepare a single ion.

7.2 Analysing the ion cloud - mass spectrum

In order to analyse the constituents of the ion cloud a mass spectrum is recorded [66], which is based on the peak detection described in Sec. 4.1.1. The ring voltage U_R is ramped from -14 V to -3 V within 10 s. As a result the axial frequency of ions with different charge-to-mass-ratio q/m is tuned in resonance with the axial detection circuit at different times of the voltage ramp. Simultaneously to the voltage ramp, a continuous dipolar excitation is applied to the trap at a frequency slightly above the resonance frequency of the axial detection system to increase the axial energy before the ions are brought into resonance with the tank circuit. A custom-made amplifier integrates over the power of the tank circuit and amplifies the signal, which then can be monitored with an oscilloscope. In order to assign the voltages to the correct q/m-ratios, the voltage ramp has to be synchronized to the recording of the signal. Measuring the signal strength as a function of time yields mass spectra as shown in Fig. 7.1 and provides the possibility to distinguish between the trapped ions. However, note, that different ion species with similar q/m-ratio appear at the same

position and cannot be resolved.

7.3 Selection of one ion species

As a first step towards a single ion, unwanted ion species and charge-states have to be removed from the trap without loosing the $^{28}Si^{11+}$ ions[1]. The strong space-charge interaction within this large ion cloud requires for a selective cleaning procedure with little interaction between the different species. In the course of this thesis it turned out that this is not fulfilled for the routinely employed axial cleaning, which is described in Sec. 7.3.2, especially if a large ion cloud contains only a small number of the required ions. This technique relies on the excitation of the axial motion, which results in an oscillation of the excited ions through the cold ion cloud. Due to collisions the excited ions can transfer their energy to the originally not-excited $^{28}Si^{11+}$ ions. As result the $^{28}Si^{11+}$ ions are removed from the trap as well. To this end, the highly-sensitive B_2-*cleaning* technique has been developed. Finally, both techniques are employed, starting with the B_2-cleaning technique until the amount of remaining ions allows for the application of the axial cleaning technique.

7.3.1 B_2-cleaning technique

For the B_2-cleaning technique the modified cyclotron mode of $^{28}Si^{11+}$ is excited in the precision trap. Afterwards the whole ion cloud is transported to the analysis trap where the large B_2-term of $10\,\mathrm{mT/mm^2}$ is available. The $^{28}Si^{11+}$ ions are brought into resonance with the axial tank circuit to resistively cool the axial motion. When the ions are in thermal equilibrium with the tank circuit, the electrostatic trapping potential is switched to 0 V. As a result the ions are no longer confined within the axial direction except for those ions whose energy due to the magnetic moment of the cyclotron motion is higher than their kinetic axial energy E_z:

$$E_\mathrm{cyc,z} \gg E_\mathrm{z} \tag{7.1}$$

$$\mu_\mathrm{z}^\mathrm{cyc} B_2 z_\mathrm{max}^2 \gg k_\mathrm{B} T_\mathrm{z} \tag{7.2}$$

$$\frac{1}{2} q\, r_+^2 \omega_+ B_2 z_\mathrm{max}^2 \gg k_\mathrm{B} T_\mathrm{z}. \tag{7.3}$$

Here, q is the charge of the considered ion, r_+ the radius of the modified cyclotron motion, ω_+ the modified cyclotron frequency, k_B is the Boltzmann constant and T_z is the mean axial temperature. z_max is the axial oscillation amplitude due to the magnetic moment of the cyclotron motion. It should be small enough to ensure that the ion stays within the region where the magnetic field has a quadratic dependence on the coordinate, which is of

[1] The whole preparation procedure is described for $^{28}Si^{11+}$ since this is the ion of interest for this thesis. Nevertheless, this can be applied in a similar way to any ion species, which can be produced by the mini-EBIT.

the order of $z_{\max} = 1\,\mathrm{mm}$ (compare Fig. 4.5). Accordingly, to be magnetically trapped, the $^{28}Si^{11+}$ ions have to be excited to a radius of at least

$$r_+ \geq \sqrt{\frac{2k_B T_z}{q\,\omega_+ B_2 z_{\max}^2}} = 26\mu\mathrm{m} \tag{7.4}$$

for an ion temperature of $T_z = 10\,\mathrm{K}$.

After about 1 s the electrostatic trapping potential is switched on again and the ions are transported to the PT, where the cyclotron mode of $^{28}Si^{11+}$ is cooled by sideband cooling. This technique is very selective even for large ion clouds since the immediate loss of ions on a cyclotron orbit smaller than 26 µm prevents energy transfer due to collisions. However, there are almost always ions, which are already created on a large cyclotron orbit implying that there are still some unwanted species left after the B_2-cleaning. Nevertheless, the number of unwanted ions is significantly reduced, hereby enabling the application of the axial cleaning technique.

7.3.2 Axial cleaning technique

In order to remove the remaining ions of unwanted species as well, the axial motion is excited by a dipolar excitation. Hot ions are evaporated by lowering the trapping potential to $-0.5\,\mathrm{V}$. The $^{28}Si^{11+}$ ions are tuned in resonance with the tank circuit to be resistively cooled during the excitation process. However, unwanted ions with a similar q/m-ratio as $^{28}Si^{11+}$ are also cooled and thus are not addressed by the excitation. It has to be assured that the excitation frequency does not match neither the magnetron frequency ν_-, the axial frequency ν_z nor the $2\nu_z$-frequency of $^{28}Si^{11+}$ since this would provoke the loss of $^{28}Si^{11+}$ as well. The modified cyclotron frequency ν_+ is too high to be affected by axial excitation drives.

We utilize two different excitation schemes [99] to excite the axial mode of undesired ions:

1. A dipolar SWIFT (Stored Waveform Inverse Fourier Transform) excitation provides high excitation amplitudes at all frequencies except for those within determined frequency ranges. The time domain signal is obtained by the inverse Fourier transform of the desired excitation frequency spectrum.

2. The dipolar excitation is swept over a wide range to match the axial oscillation frequency of the unwanted ion species.

Usually, both excitation schemes have to be employed several times until the trap is “clean”. Note, that we do not have the possibility to definitely exclude the presence of other unwanted ions in the trap. On the one hand, the mass spectrum does not cover all q/m-ratios, since for ions with $q/m < 0.235$ a voltage above the maximum voltage of the UM1-14 of $-14\,\mathrm{V}$ is required. On the other hand, even if the ion has a q/m-ratio, which is covered by the mass

spectrum the sensitivity might not be high enough to be detected. However, the presence of a second ion in the trap becomes noticeable by observing an unexpected behaviour of the $^{28}Si^{11+}$ ion, for example a poor frequency stability or sudden frequency jumps. The first indication of a clean trap is a stable noise-dip with the maximum possible depth, defined by the signal-to-noise-ratio of the noise-resonance.

7.3.3 Cyclotron cleaning technique

In order to distinguish between ions with a similar q/m-ratio the cyclotron cleaning technique is employed, which is highly selective, but inapplicable for a large q/m-range. It relies on the same principle as the axial cleaning technique but excites the modified cyclotron mode, which is specific for each ion species. This means on the one hand that the ion, which should be removed from the trap can be addressed very selectively. On the other hand this requires to identify the particular ion species in order to know the modified cyclotron frequency. Moreover, for the different ions species the particular modified cyclotron frequencies varies over a wide range of several MHz and thus it would take several hours to sweep over such a large frequency range. Accordingly, this technique is only employed if an unwanted ion species is present, which cannot be distinguished from $^{28}Si^{11+}$ by the axial cleaning technique.

7.4 Reduction to a single ion

Having removed all ion species except for $^{28}Si^{11+}$ the last step is the reduction to a single ion. The number of $^{28}Si^{11+}$-ions, which are in thermal equilibrium with the axial detection system, can be determined by measuring the width of the axial dip, which is proportional to the number of ions according to Eq. (4.15). Two techniques can be employed to reduce the number of ions:

- After excitation of the axial mode the trapping potential is lowered until the hottest ions evaporate.
- The modified cyclotron mode is excited before lowering the trapping potential to evaporate hot ions.

In both cases it is advisable to start with a small excitation amplitude and a little reduction of the trapping potential in order not to loose all ions simultaneously.

7.5 Setting up the g-factor measurement

Since the g-factor measurement is fully automated all required settings have to be determined before. This includes the measurement of the three eigenfrequencies of the ion in

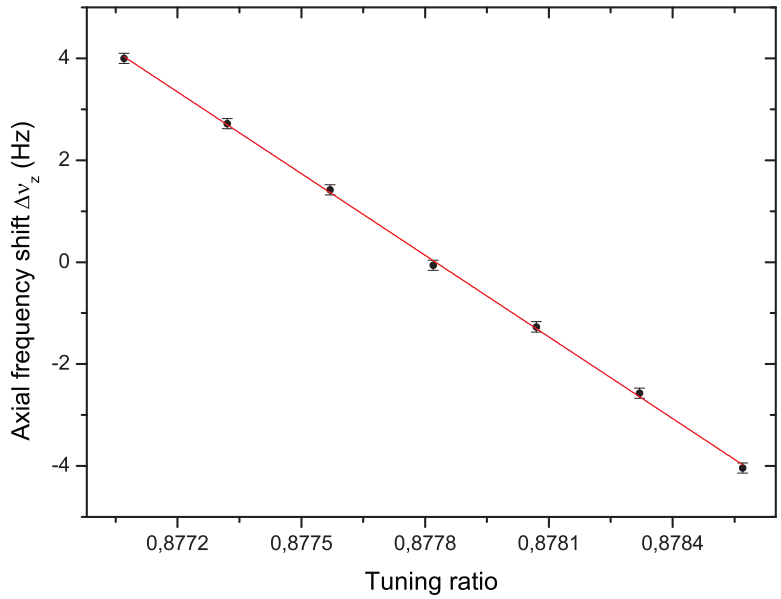

Figure 7.2: To optimize the tuning ratio TR in the precision trap the axial frequency shift $\Delta\nu_z$ due to a defined magnetron radius is measured as a function of the tuning ratio TR. The optimal TR_{opt} is determined from a linear fit to $TR_{opt} = 0.877825(7)$ at $\Delta\nu_z = 0$. For more details see text.

both measurement traps (see chapter 4) and the corresponding sideband-coupling frequencies as well as the adjustment of axial feedback and the knowledge of the Larmor frequency in the AT. Moreover the trapping potential has to be tuned to high harmonicity to avoid energy-related frequency shifts. Since it turned out that the spin flip rate in the analysis trap was significantly lower than expected from the theoretically predicted lineshape and the previous measurement of $^{28}Si^{13+}$, the Larmor resonance in the analysis trap was measured as well and several additional measurements were performed to analyze the reason for the low spin flip rate.

7.5.1 Optimization of the electrostatic trapping potential

The first step is the optimization of the electrostatic trapping potential in both measurement traps. Although the experimental realization is slightly different for the two traps, the basic principle is the same. In the presence of anharmonicities, the axial frequency for two different temperatures T_1 and T_2 of the particular eigenmode differs by

$$\Delta\nu_z = \nu_z(T_2) - \nu_z(T_1) \tag{7.5}$$

according to Eq. (3.16). The C_4-term can be eliminated by adjusting the voltage applied to the correction electrodes U_c and thus the tuning ratio $TR = U_R/U_c$. To this end, the axial frequency shift $\Delta\nu_z$ is measured as a function of the tuning ratio TR.
In the precision trap a burst excitation of the magnetron motion is performed, hereby increasing the magnetron radius and thus the energy in the magnetron mode to a well-defined value. The axial frequency of the cold (T_1) and the hot (T_2) ion is measured and, as expected from Eq. (3.16) a linear dependency of the frequency shift $\Delta\nu_z$ on the TR is derived as shown in Fig. 7.2. A vanishing frequency shift $\Delta\nu_z = 0$ indicates the optimal TR, which is deduced from a linear fit to the data to $TR_{opt} = 0.877825(7)$. Simulations of the trapping potential show that our trap is not completely compensated, which means that C_4 and C_6 cannot be eliminated simultaneously. However, for the oscillation amplitudes of the ion during the double-dip measurement the influence of the remaining C_6-term on the frequencies can be completely neglected.
In the analysis trap a magnetron excitation would result in an additional shift of the axial frequency due to the large B_2-term (see Eq. (3.18)). However, a change of the axial energy does not cause an additional shift of the axial frequency due to the B_2-term but only due to the C_4-term. To this end the axial temperature is increased by applying white noise to the axial detection system and again the resulting frequency shift as a function of the TR is measured.

7.5.2 Axial frequency stability in the analysis trap

For the detection of the spin orientation, the phase-sensitive detection technique is applied. A frequency stability of the order of $\delta\nu_{z,rms} \simeq 50\,\text{mHz}$ at a total axial frequency of 411 kHz has to be achieved to allow for reliable detection of a frequency jump of $\Delta\nu_{z,SF} = 240\,\text{mHz}$ caused by a spin flip. For this frequency stability, modelled by Gaussian distributed frequency fluctuations with a standard deviation of 50 mHz, the probability of a frequency jump of $\Delta\nu_z \geq 200\,\text{mHz}$, which is not caused by a spin flip, amounts to 0.006 %.
Due to technical problems the spin flip rate in the AT was only of the order of 1% (see Sec. 7.5.3), which means that in average about every 2 h a spin flip is induced. Thus, the magnetron and the reduced cyclotron mode are cooled after every 96^{th} phase measurement to prevent a heating of the corresponding mode, which would reduce the frequency stability. As can be seen in Fig. 7.3 the achieved frequency stability is very high even over several hours and thus ensures the unambiguous distinction between the two spin states.

7.5.3 Larmor resonance in the analysis trap

Within this experiment the analysis trap is only required for the determination of the spin state. This is achieved by inducing transitions between the two spin states and observing the

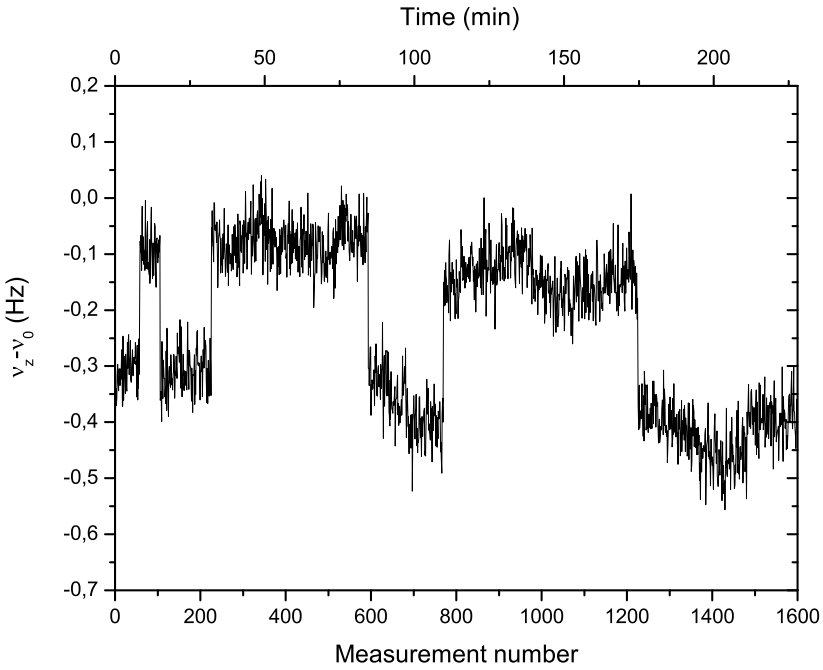

Figure 7.3: Measurement of the axial frequency ν_z with the phase sensitive detection technique as a function of time. After eight successive axial frequency measurements microwaves are irradiated for 30 s to induce a spin flip. The frequency stability allows for the unambiguous distinction between the two spin states up and down even over long time intervals of several hours.

direction of the frequency jump. Accordingly, spin flips have to be induced by irradiating microwaves at the Larmor frequency of the electron spin. The time required for the g-factor measurement depends on the spin flip probability in the analysis trap because at least one spin flip has to be observed before the ion can be transported to the precision trap. Thus, a spin flip probability as high as possible is required. However, for $^{28}Si^{11+}$ almost no spin flips could be observed. Scanning the irradiated microwave frequency yielded the Larmor resonance shown in Fig. 7.4 with a maximum spin flip probability of only 1%. The shape of the Larmor resonance can be theoretically calculated [100] and for the hydrogenlike silicon $^{28}Si^{13+}$ ion this prediction perfectly described the measured resonance [61]. Since the experimental parameters were not changed between the $^{28}Si^{13+}$ and the $^{28}Si^{11+}$ measurement, a similar shape (with a slightly different width) and especially a similar spin flip rate of about 25 % for the maximum available microwave power of the multiplier, was expected for the $^{28}Si^{11+}$ ion (see Fig. 7.5). However, the maximum spin flip rate was by a factor of 20

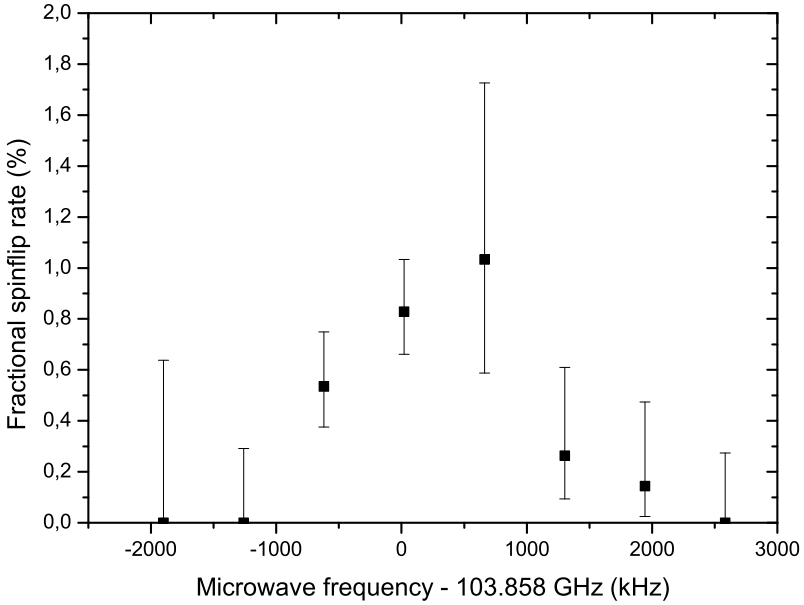

Figure 7.4: Larmor resonance measured in the analysis trap with a single $^{28}Si^{11+}$ ion for an axial temperature of $T_z = 11.0(0.7)$ K. The lineshape differs significantly from the theoretical prediction (see Fig. 7.5) and yields a maximum spin flip probability of only 1 %.

lower than expected and the shape of the resonance does not reflect the thermal Boltzmann distribution rather it is symmetric. In addition, the relative linewidth of 10^{-5} is one order of magnitude larger than expected from the theoretical lineshape. A broadening of the resonance would be expected if the resonance was saturated, which, however, would imply a spin flip rate of 50 % being in contrast to the maximum observed spin flip rate of 1%. To find the reason for the observed effect several parameters were tested:

1. The stability and the power of the microwave system, which both influence the spin flip rate, were tested. The microwave system can be tested as far as to the hat (compare Fig. 5.1) of the experiment and proved to work reliably. As a cross-check the synthesizer as well as the multiplier have been replaced, which had no effect on the spin flip rate.

2. The axial temperature of the ion was measured, since a higher axial temperature would cause a broadening of the Larmor resonance in combination with a decreased maximum spin flip rate as shown in Fig. 7.5. For higher axial temperatures, the Boltzmann distribution of axial energies is broadened (see Fig. 7.6), which is reflected

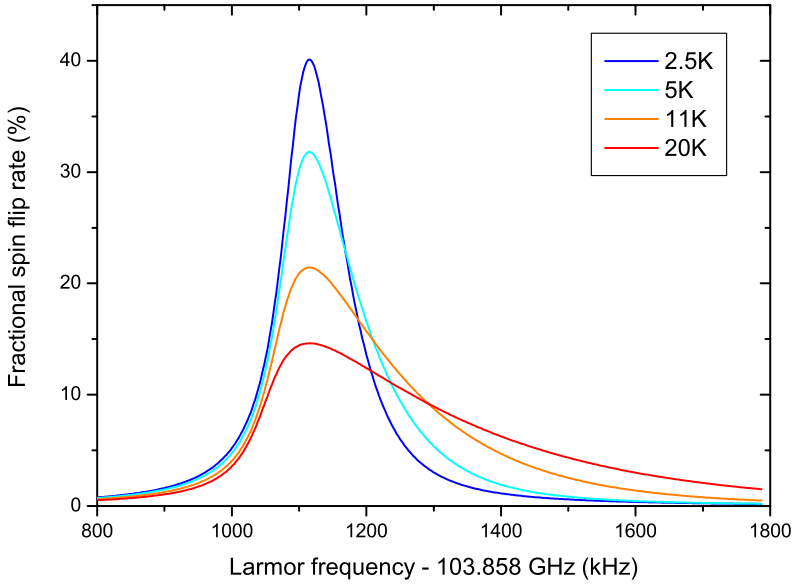

Figure 7.5: Theoretical lineshape of the Larmor resonance of a single $^{28}Si^{11+}$ ion in the magnetic bottle field of the analysis trap for different axial temperatures. The lineshape reflects the Boltzmann distribution of the ion's axial energy due to the magnetic inhomogeneity. It has been calculated according to the model developed in the Ph.D.-thesis of J.Verdú [100]. In the experiment the axial temperature is changed by the application of negative feedback as shown in Fig. 7.6.

by the magnetic field seen by the ion and thus by the Larmor frequency. Since the total microwave power, corresponding to the area below the Larmor resonance, is constant, the maximal spin flip rate decreases. We determined the axial temperature to be $T_z = 11.0(0.7)$ K, similar as for the hydrogenlike ion. As a next step we decreased the temperature with axial feedback to achieve a smaller linewidth and the corresponding increased spin flip rate. However, no significant dependence on the axial temperature could be observed.

3. The measured free cyclotron frequency was verified to check if we determined the magnetic field correctly and irradiate the right microwave frequency. The magnetic field agrees with the magnetic field measured with $^{28}Si^{13+}$ and several repetitions of the measurement confirmed the value. Nevertheless, we measured the spin flip probability over a broad range of microwave frequencies. This revealed that the Larmor frequency is correct but the Larmor resonance is one order of magnitude too broad.

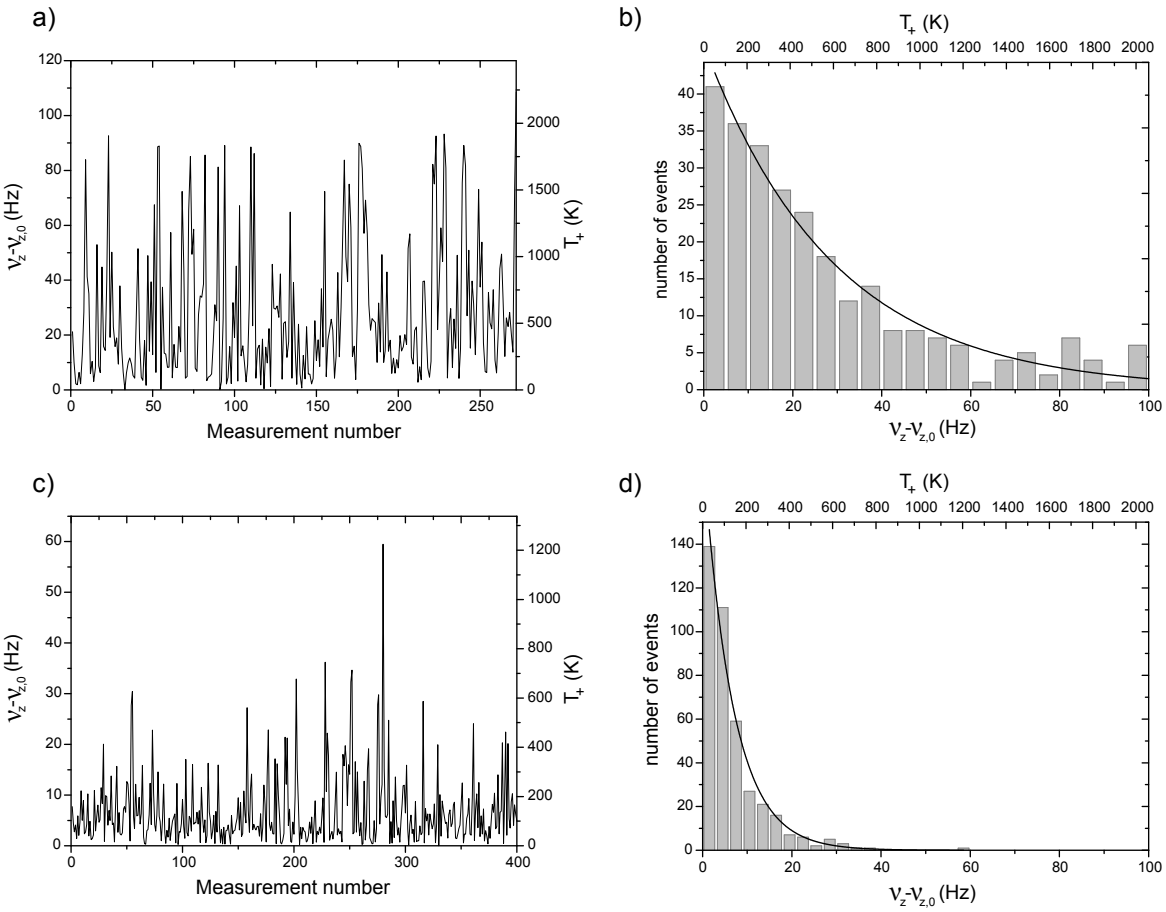

Figure 7.6: Temperature measurement in the AT without (a,b) and with (c,d) negative electronic feedback applied to the axial detection system. The modified cyclotron frequency is repeatedly coupled to the axial frequency and the corresponding axial frequency shift, which is a measure of the modified cyclotron energy, is measured for each coupling (a,c). Assuming statistical error bars an exponential fit to the Boltzmann-distributed histogram of the axial frequency jumps yields the modified cyclotron temperature T_+, which is directly proportional to the axial temperature $T_\mathrm{z} = (\nu_\mathrm{z}/\nu_+) \cdot T_+$. By application of negative feedback the axial temperature can be reduced from $T_\mathrm{z} = 11.0(0.7)\,\mathrm{K}$ to $T_\mathrm{z,FB} = 2.5(0.1)\,\mathrm{K}$, corresponding to $T_+ = 597(39)\,\mathrm{K}$ and $T_\mathrm{+,FB} = 136(8)\,\mathrm{K}$, respectively.

4. The stability of the free cyclotron frequency was investigated, to look for magnetic field fluctuations, which would correspond to fluctuations of the Larmor frequency. To this end, the modified cyclotron frequency in the AT was measured over 7.5 h as shown in Fig. 7.7. The measurement shows fluctuations of the order of $\delta\nu_+/\nu_+ = 1 \cdot 10^{-7}$ being about two orders of magnitude below the value, which could explain the broadening of the Larmor resonance. However, one measurement takes about 20 min and thus fluctuations on the scale of seconds cannot be excluded. But the stability of the magnetic field in the PT was measured to be orders of magnitude higher than the equivalent broadening of the Larmor resonance in the AT.

5. It was carefully looked for the presence of other ions in the trap, which might interact with the ion. Within several measurements no indication for another particle was found. Moreover, the same effect was observed for three different $^{28}Si^{11+}$ ions, which have been prepared by different cleaning techniques and even by different persons thus minimizing the possibility to end up with the same situation inside the trap.

6. The compensation coil, being the main modification of the setup since the $^{28}Si^{13+}$ measurement has been finished, was quenched during a spin flip drive, which however had no influence on the spin flip probability.

7. The spin flip rate of $^{28}Si^{13+}$ was measured again to see if the rate for this system is still high, which proved to be the case.

As a consequence of the low spin flip rate of 1%, on average one spin flip every 2 h is induced, which makes the investigation of the effect very time-consuming. Since none of the tested parameters could explain the low spin flip rate, the next step was to investigate another lithiumlike ion of a different species. We decided on lithiumlike oxygen $^{16}O^{5+}$, since it is simple to produce and, assuming a scaling of the effect with the nuclear charge Z, the effect might be even more significant. Here, the same width of the resonance but a slightly higher spin flip rate of about 6% was observed. Accordingly, we assumed that the broadening of the Larmor resonance is related to lithiumlike systems.
In the precision trap, however, we found no indication for a similar effect, which led to the conclusion that it is caused by the magnetic bottle, being the only difference between the two traps. For the precision trap the B_2-term was measured to be $B_2 = 0.52(16)\mu T/mm^2$ [61], which is a factor of 20,000 smaller than in the analysis trap. Assuming a linear scaling of the observed effect with the magnetic inhomogeneity, the corresponding linewidth of the g-factor resonance in the precision trap would be of the order of $7 \cdot 10^{-10}$ and thus one order of magnitude smaller than the width of the g-factor resonance measured with the double-dip technique (see Sec. 8.2). This implies that an equivalent effect in the precision trap could be neglected at the presented level of precision. To this end, we measured the g-factor of

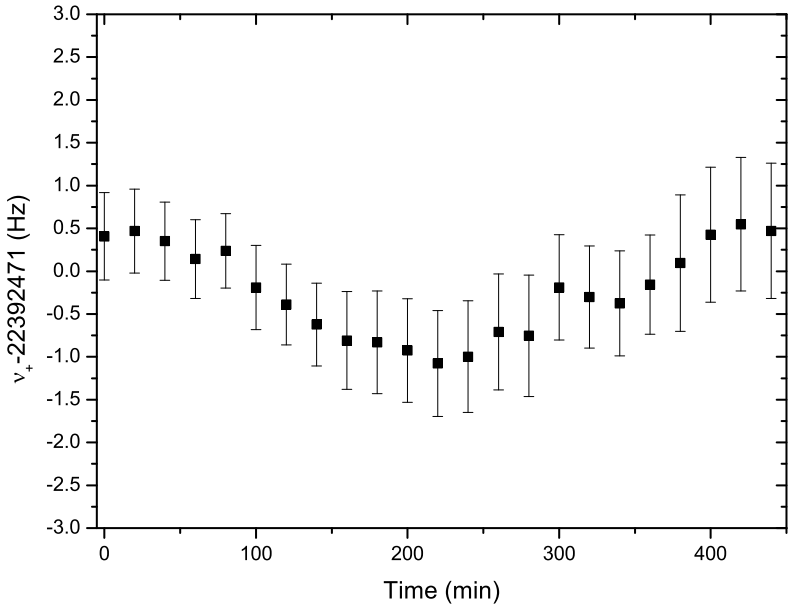

Figure 7.7: Series of modified cyclotron frequency measurements in the analysis trap (see Sec. 4.3.3). Each measurement is averaged over ten single measurements. The stability of the modified cyclotron frequency and thus of the magnetic field is of the order of $\delta\nu_+/\nu_+ = 1 \cdot 10^{-7}$, which is about two orders of magnitude smaller than the observed width of the Larmor resonance.

$^{28}Si^{11+}$ in the precision trap with a spin flip rate in the analysis trap of only 1% (see chapter 8).

Having finished the g-factor measurement with $^{28}Si^{11+}$ we went on to hydrogenlike carbon $^{12}C^{5+}$. For this system we observed almost no spin flips at all. As a result, we decided to go back to $^{28}Si^{13+}$ again and measured a Larmor resonance in the AT. We observed that the spin flip rate is indeed high but the resonance is also broadened by a factor of about 10 compared to the previous Larmor resonance of $^{28}Si^{13+}$ in the analysis trap. This previous resonance, however, has been recorded before several smaller changes of the experimental setup have been made, e.g. the exchange of the transport electrodes between analysis trap and precision trap. After this observation we changed the microwave setup, mainly the horn-horn transitions, which resulted in a higher available total microwave power. Due to the increased power and the corresponding high spin flip rate it became possible to investigate the Larmor resonance and its origin with $^{12}C^{5+}$ with sufficient high statistics. Finally,

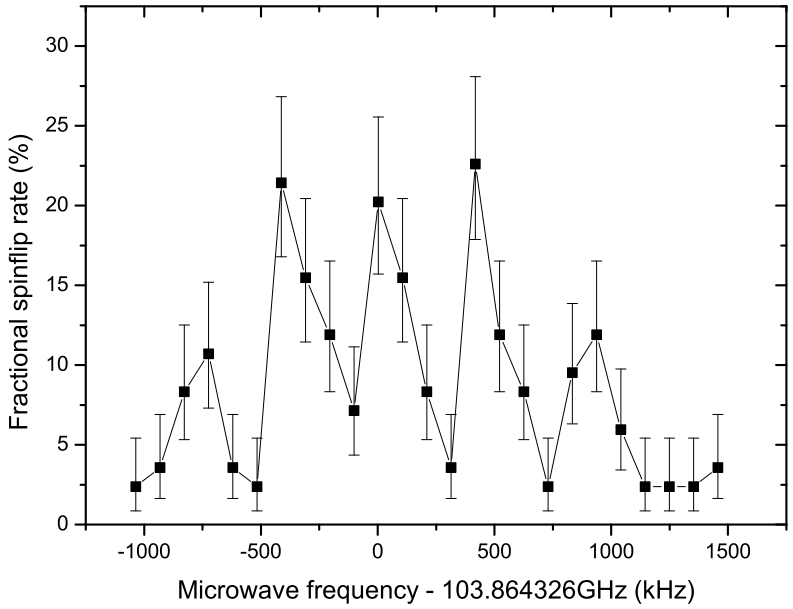

Figure 7.8: Larmor resonance in the analysis trap for a $^{12}C^{5+}$ ion. After cooling of the magnetron mode axial sidebands at $n \cdot \nu_z = n \cdot 412\,\mathrm{kHz}$ can be resolved. They originate from an axial displacement of the ion in the inhomogeneous magnetic field and the oscillation within the resulting B_1-term.

it was found that the observed effect was not a broadening of the resonance but a combination of axial and magnetron sidebands due to an axial and a radial displacement of the ion, respectively. The axial displacement with regard to the center of the magnetic bottle field can be determined. Appropriate voltages applied to the electrodes enable a controlled shift of the ion's axial position, which is known from theoretical calculations of the electric trapping potential. If the modified cyclotron frequency is measured at each position the magnetic field can be determined and the position of the ion inside the magnetic bottle field can be obtained. An axial displacement of about 80 µm from the minimum of the magnetic bottle was measured. The influence of a magnetic inhomogeneity on the shape of the Larmor resonance has been analyzed in the Ph.D.-thesis of N. Hermannspahn [101], however for a vanishing axial displacement. Due to the displacement the ion experiences a strong additional B_1-term, which has to be included in the calculations. In this case, the magnetic field along the $\hat{z}$-axis reads

$$B(z) = B_0 + B_1 \cdot z + B_2 \cdot z^2 \tag{7.6}$$

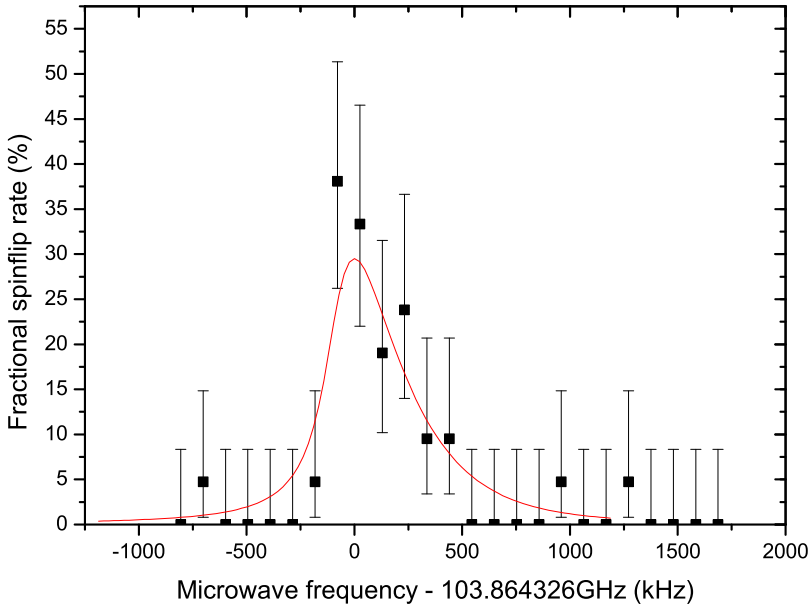

Figure 7.9: Larmor resonance in the analysis trap for a strongly magnetron cooled $^{12}C^{5+}$ ion positioned in the center of the magnetic bottle field. The red line is the theoretically predicted lineshape for an axial temperature of 7 K [100], which fits well to the data points (black boxes).

and the magnetic field seen by the ion amounts to

$$B(t) = B_0 + B_1 z_0 \sin(2\pi\nu_z t) + B_2 z_0^2 \sin^2(2\pi\nu_z t) \tag{7.7}$$

$$= B_0 + B_1 z_0 \sin(2\pi\nu_z t) + \frac{1}{2} B_2 z_0^2 (1 - \cos(2\pi 2\nu_z t)). \tag{7.8}$$

The corresponding effect on the Larmor frequency is

$$\nu_L(t) = \nu_L^0 + \Delta\nu_L^1 \sin(2\pi\nu_z t) + \Delta\nu_L^2 (1 - \cos(2\pi 2\nu_z t)) \tag{7.9}$$

where the coefficients have been summarized in $\Delta\nu_L^i$. The Fourier transformation of this frequency modulated oscillation yields sidebands for the Larmor resonance separated by $\nu_z \simeq 412\,\text{kHz}$. A radial displacement from the trap center can be analogously described, resulting in magnetron sidebands with a much smaller spacing of $\nu_- \simeq 4\,\text{kHz}$.
These theoretical considerations are confirmed by experimental observations[2]. As a first step, a strong sideband-cooling of the magnetron mode with negative feedback applied to

[2]The measured data are also part of the Ph.D.-thesis of Florian Köhler [97]

the axial detection system to suppress the magnetron sidebands was performed and resulted in the Larmor resonance shown in Fig. 7.8. Here strong axial sidebands due to the axial displacement at $n \cdot \nu_z = n \cdot 412\,\mathrm{kHz}$ can be resolved. As a next step the ion was shifted to the minimum of the magnetic bottle field in combination with strong magnetron cooling. The resulting Larmor resonance is shown in Fig. 7.9 as well as the theoretical prediction for an axial temperature of T_z (red line), which describes the experimental data well.
In summary, the observed unexpected shape of the Larmor resonance in the analysis trap was not the result of a broadening but rather it was a result of many overlapping axial and magnetron sidebands due to an axial and radial displacement with regard to the center of the magnetic bottle field. These sidebands could not be resolved with $^{28}Si^{11+}$ and $^{16}O^{7+}$ due to the extremely low spin flip rates. The magnetron sidebands can be suppressed by strong cooling, whereas the axial sidebands are eliminated by positioning the ion in the center of the magnetic bottle field.
The most important consequence of this solution is that the final *g*-factor value measured in the precision trap is not affected, except for the statistical error due to the low spin flip rate. Since the width of the Larmor resonance in the precision trap is about two orders of magnitude smaller than in the analysis trap and both, the axial and the magnetron frequency are larger compared to the analysis trap, possible sidebands would not be visible. Moreover, the magnetic inhomogeneity is by a factor of 20,000 smaller.

Chapter 8

The g-factor of lithiumlike silicon $^{28}Si^{11+}$

In the course of this thesis, the trapping and detection techniques as well as the preparative measurements, which have been presented in the previous chapters are all aimed at the determination of a single number - the g-factor of the $2s$-electron bound in lithiumlike silicon $^{28}Si^{11+}$. The final g-factor measurement itself is completely automated, which means that the whole measurement is performed by a self-written *LabView*-program, which controls and synchronizes all devices and records the data. This automation is necessary since most of the steps have to be precisely synchronized. During the measurement all disturbances have to be minimized, which means in practice that the laboratory is only entered to fill cryogenic liquids.
The g-factor measurement includes several hundred cycles of frequency ratio measurements and the corresponding spin state detection. A maximum likelihood fit to the resonance obtained yields the frequency ratio which corresponds to the maximum spin flip probability and thus is required to determine the g-factor. Overall three spin flip resonances have been recorded for different microwave powers and the weighted average of the three values yields the preliminary result, which has to be corrected for systematic shifts. At the presented level of precision a careful analysis of possible uncertainties has to be done before the final g-factor value can be calculated and compared to the theoretical value.

8.1 One measurement cycle

One measurement cycle of the g-factor measurement starts with the ion stored in the AT to determine the spin orientation of the valence electron. After cooling all eigenmodes of the ion, the axial frequency of the ion is measured successively with the phase-sensitive detection technique. After each eight measurements, microwaves are irradiated at the Larmor frequency with the maximum available power for 30 s. This sequence is repeated until at

least one spin flip is detected, hereby determining the spin orientation. Due to the low spin flip rate the spin state analysis took in average about 2 h, necessitating the interim cooling of the radial modes to achieve the required frequency stability even over these long time periods. Having observed a spin flip and thus knowing the spin state, the ion is adiabatically transported to the PT. After cooling the eigenmodes and waiting for the high-precision trapping voltages to settle, the modified cyclotron frequency is measured with the double-dip technique. This is necessary due to the low spin flip rate in the AT and the corresponding long time periods between two successive measurements in the PT. Between these measurements the magnetic field might have changed and a microwave frequency calculated with the free cyclotron frequency determined in the previous cycle might be off-resonant. To avoid measurement time loss due to this effect, the free cyclotron frequency is measured directly before the actual frequency ratio measurement and the microwave frequency is calculated according to this result.
The actual high-precision measurement of the frequency ratio Γ starts with the recording of an axial dip spectrum for an averaging time of 150 s. Afterwards, the modified cyclotron frequency is measured with the double-dip technique for the same averaging time. Simultaneously, microwaves are irradiated to induce a spin flip. A second axial dip is recorded to linearly interpolate the axial frequency to the time of the modified cyclotron frequency measurement. Finally, the ion is transported back to the AT to determine if the spin flip attempt in the precision trap was successful by determining the spin state and comparing it to the spin state which was detected before transport to the PT. Accordingly, the spin state analyse is the last step of the previous cycle as well as the first step of the next cycle. In the following all steps of one cycle are summarized in detail and the particular required time is given in parentheses:

1. Spin state detection in AT
    a) Sideband cooling of the magnetron mode (5 s)
    b) Sideband cooling of the modified cyclotron mode below a defined threshold with negative feedback applied to the axial tank circuit ($\sim$ 1 min)
        c) Eight axial frequency measurements with the phase-sensitive measurement technique ($\sim$ 30 s)
        d) Microwave excitation to induce a spin flip (30 s)
        e) Repeat steps c) and d) ten times ($\sim$ 10 min)
    f) Check if a spin-flip was successfully induced. If a spin flip is detected, continue with 2). If no spin flip is detected restart with 1a)
2. Sideband cooling of the magnetron mode (5 s)
3. Adiabatic transport to PT ($\sim$ 30 s)

4. Waiting time to achieve a settling of the trapping voltages (30 s)
5. Sideband cooling of the magnetron mode (3 s)
6. Open the cryogenic switches
7. Modified cyclotron frequency measurement with the double-dip-technique to determine the free cyclotron frequency and thus the current Larmor frequency for the microwave irradiation in step 9) (90 s)
8. Axial frequency measurement with the dip-technique (150 s)
9. Modified cyclotron frequency measurement with the double-dip technique. Simultaneously, microwave irradiation is performed at a frequency randomly distributed ($\Delta\nu_L/\nu_L \simeq \pm 5 \cdot 10^{-8}$) around the expected value for the Larmor frequency ν_L (150 s)
10. Axial frequency measurement with the dip-technique (150 s)
11. Sideband cooling of magnetron mode (3 s)
12. Close the cryogenic switches
13. Adiabatic transport to AT ($\sim$ 30 s)
14. Restart of the cycle with step 1).

As a result of the low spin flip rate in the analysis trap (see Sec. 7.5.3) one measurement cycle usually takes a few hours. The remaining parts of the cycle including the transports and the measurements in the precision trap take about 15 min in total. Thus, the overall measurement time for one g-factor resonance is of the order of one month. During liquid nitrogen and liquid helium filling the measurement was stopped and afterwards continued. The magnetron frequency is not measured at each cycle but only once before data taking for the g-factor resonance and once afterwards. This is sufficient since for a g-factor measurement to $\delta g/g = 10^{-9}$ the magnetron frequency has to be determined with a relative uncertainty of $\delta\nu_-/\nu_- = 10^{-3}$ (see Sec. 4.4). This corresponds to a total change of the magnetron frequency of 10 Hz. Over a time period of two months the magnetron frequency varies less than 0.1 Hz, which allows for the infrequent measurements of ν_-.

8.2 The g-factor resonance

The measurement cycle described in the last section is repeated a few hundred times. For each cycle the frequency ratio $\Gamma = \nu_L/\nu_c$ is determined by measuring ν_c while irradiating ν_L and it is analysed whether a spin flip has been induced or not. The spin flip rate as a function

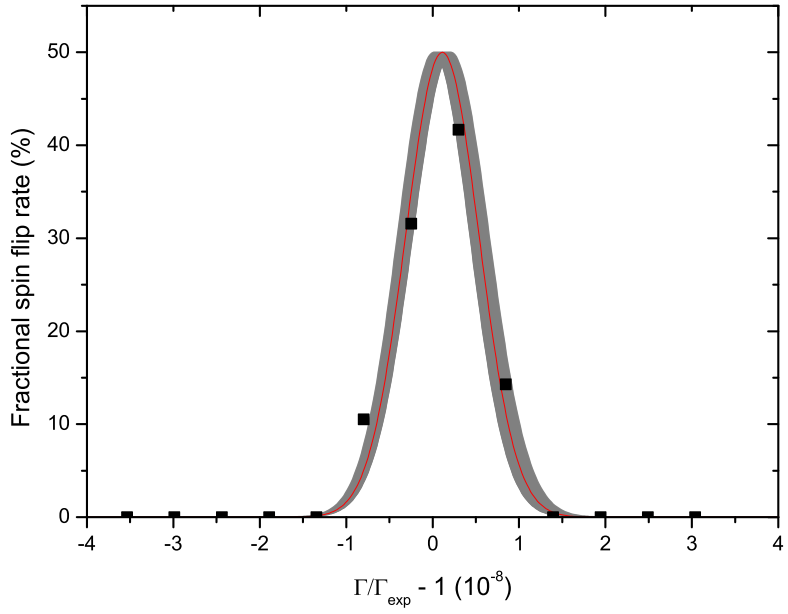

Figure 8.1: g-factor resonance of $^{28}Si^{11+}$ [41]. The spin flip rate is plotted as a function of the measured frequency ratio $\Gamma = \nu_L/\nu_c$. The center of the resonance can be obtained from a maximum likelihood fit with a Gaussian lineshape (red line) to a relative precision of $1 \cdot 10^{-9}$. The grey area indicates the confidence interval of the fit. The data points (black boxes) are only shown for visualization purposes since no binning is required for the fit procedure.

of the frequency ratio Γ yields a g-factor resonance as shown in Fig. 8.1. We have recorded three resonances each with a different microwave-power with an overall measurement time of about four months arising from the low spin flip rate in the analysis trap. To this end the microwave power in the precision trap was initially chosen to be as high as possible to be able to resolve a resonance even for low statistics. However, a high microwave power results in a saturated and broadened resonance and thus in a lower precision. Thus, the power was decreased from resonance to resonance, which is reflected by the smaller width and the corresponding reduced uncertainty (see Fig. 8.3). The effect of the high microwave power on the g-factor resonance is discussed in Sec. 8.4.6. The measurement of the three resonances yields a g-factor with a relative precision of the order of 10^{-9}. This is more than one order of magnitude more precise than the theoretical value and any further improvement of the experimental uncertainty would not result in a more sensitive test of the theoretical calculations. Thus, the measurement was stopped at this point.

8.3 Maximum-likelihood fit

A g-factor resonance is obtained by assigning each frequency ratio either to a successful or an unsuccessful spin flip attempt. Counting the successful attempts within a specified frequency ratio interval yields a histogram as indicated by the black data points in Fig. 8.1. A binning of the data is mandatory for a data analysis with a least-squares fit to the resonance. However, the choice of the width of the bins is rather subjective and can influence the fit result obtained. Moreover, the error bars for the binned spin flip rate are binomial distributed and thus asymmetric, especially for low spin flip rates. However, the least-square method generally assumes normally distributed error bars. Accordingly, a fit with standard least-squares methods does not provide correct estimates for the uncertainties of the fit parameters.

The limitations of binning and symmetric error bars can be overcome by employing the maximum likelihood method [102], which is a general method to estimate the parameters for an arbitrary (known) distribution. This method has already been applied for the g-factor measurement of hydrogenlike silicon $^{28}Si^{13+}$ [16, 61]. It requires no binning of the data but considers each individual data point.

For a given data set p_i the parameter set $\vartheta = \vartheta_1 ... \vartheta_m$ is found, which maximizes the maximum likelihood function

$$L(\vartheta) = \prod_{i=1}^{N} f(p_i; \vartheta) \tag{8.1}$$

and thus the probability to measure exactly the given data set. In practice, the numerical calculation of a sum is much more effective than the calculation of a product. Since only the position of the maximum is of interest and not the value of the likelihood function itself, the increasing monotony of the logarithm function can be used to decompose the product into a sum and maximize the loglikelihood function

$$\mathcal{L}(\vartheta) = \log\left(\prod_{i=1}^{N} f(p_i; \vartheta)\right) = \sum_{i=1}^{N} \log f(p_i; \vartheta), \tag{8.2}$$

which enables a more efficient numerical calculation.

For the specific case of the g-factor resonance the measured frequency ratios (corresponding to p_i) are differentiated in two terms of whether a spin flip was successfully induced for this particular frequency ratio or not. Accordingly, the loglikelihood function is given by

$$\mathcal{L}(\vartheta) = \sum_{i=1}^{J} \log f_1(p_{i,\mathrm{SF}}; \vartheta) + \sum_{j=1}^{M} \log f_2(p_{j,\mathrm{noSF}}; \vartheta), \tag{8.3}$$

with $f_2(p_{j,\mathrm{noSF}}; \vartheta) = 1 - f_1(p_{j,\mathrm{noSF}}; \vartheta)$. J and M are the numbers of successful and unsuccessful spin flips attempts, respectively. For the g-factor resonance a Gaussian lineshape is fitted to the data as discussed in Sec. 8.4.6, which means that $f_1(p_{i,\mathrm{SF}}; \vartheta) = \vartheta_1 \cdot e^{-((p_{i,\mathrm{SF}} - \vartheta_2)/\vartheta_3)^2}$.

Since the maximum likelihood method considers the ensemble of the individual spin flip attempts, reliable error estimates for the adjusted parameters ϑ can be determined. To this end, the maximum likelihood method is used to fit the g-factor resonances and determine the position of the maximum $\vartheta_2 = \Gamma'_{\mathrm{exp,(i=1,2,3)}}$.

8.4 Sources of error

Before calculating the final g-factor value a careful analysis of possible sources of errors has to be performed. As discussed in the following section the energy-related frequency shifts due to anharmonicities of electrostatic and magnetic trapping potential or a high microwave power can be neglected. This is a result of small particle amplitudes during the double-dip measurement as well as small inhomogeneities of the magnetic trapping potentials and a harmonic electric potential. During the double-dip measurement the axial temperature is in thermal equilibrium with the detection system and thus at $T_\mathrm{z} = 4.8\,\mathrm{K}$. The temperature of the radial modes are related to T_z according to

$$T_+ = \frac{\nu_+}{\nu_\mathrm{z}} T_\mathrm{z} = 159\,\mathrm{K} \quad \text{and} \quad T_- = \frac{\nu_-}{\nu_\mathrm{z}} T_\mathrm{z} = 0.07\,\mathrm{K}. \tag{8.4}$$

The magnetic inhomogeneity in the precision trap was reduced by a factor of 20 compared to the previous experiments on the g-factor of hydrogenlike carbon [28] and oxygen [29] mainly by increasing the distance between analysis trap and precision trap. The remaining magnetic inhomogeneity can be measured by shifting the axial position of the ion by suited variations of the trapping potential and measuring the magnetic field via the free cyclotron frequency at each position. For the precision trap a magnetic inhomogeneity of only

$$B_2 = 0.52(16)\mu\mathrm{T/mm}^2 \tag{8.5}$$

was determined [61]. In the following the particular sources of error are discussed.

8.4.1 Mirror charge shift

The $^{28}\mathrm{Si}^{11+}$ ion is confined in a Penning trap and thus enclosed by conducting walls. Accordingly, it induces mirror charges in the electrodes and the effect of the resulting electric potential on the eigenfrequencies of the ion has to be considered. This has been performed in a variety of publications, e.g. for highly-charged ions for a spherical trap by van Dyck Jr. [103] and for a cylindrical geometry by Porto [104] as well as by Häffner in the course of his Ph.D.-thesis [105].

The effect of the electric field of the mirror charges on the ion can be divided in a retarded ($\propto 1/r_0$) and a non-retarded part ($\propto 1/r_0^3$). In case of the free electron the retarded part of the order of 10^{-13} has to be considered while the non-retarded part can be neglected [106].

However, as a result of the significantly larger mass of an ion compared to the electron, the free cyclotron frequency and thus the velocity of the ion is much smaller than for the electron implying that the retarded contribution is completely negligible in our case. For the same reason, however, the non-retarded part has to be considered for the ion and results in a significant shift of the free cyclotron frequency. The effect of the non-retarded component on the free cyclotron frequency is analyzed by considering the Coulomb force, which acts between the ion and its mirror charge. The axial frequency is not affected by the mirror charge in a symmetric cylindrical trap without slits. However, the attraction between ion and mirror charge alters the radial energies and thus shifts the radial frequencies. The effect on the free cyclotron frequency of an ion with charge q and mass m confined in a cylindrical Penning trap with radius r_0 amounts to [105]

$$\frac{\Delta\nu_c}{\nu_c} = \left(-\frac{\nu_+}{\nu_c} + \frac{\nu_-}{\nu_c}\right) \frac{q^2}{4\pi\epsilon_0 m\, r_0^3\, (2\pi\nu_c)^2} = -6.86(34)\cdot 10^{-10}. \tag{8.6}$$

A 5 % uncertainty is given since a plain cylinder is considered and the slits between the electrodes are neglected. The mirror charge effect depends on the square of the charge and thus becomes more important for heavy highly-charged ions. However, due to the strong inverse scaling with the radius this limitation can be overcome by a large radius of the trap. Due to the PnA-technique the achievable experimental uncertainty is comparable with the uncertainty of the mirror charge shift as it has been demonstrated for hydrogenlike silicon $^{28}Si^{13+}$ [61, 90]. Thus, the shift was analyzed in detail for our specific trap setup including the slits between the electrodes as well as the split correction electrode [90]. This analysis yields a relative shift of the free cyclotron frequency of

$$\frac{\delta\nu_c}{\nu_c} = -6.58(33)\cdot 10^{-10}. \tag{8.7}$$

Accordingly, the measured free cyclotron frequency has to be corrected for this value. A detailed analysis of the uncertainty still needs to be done, so we remained with the conservative estimate of a 5 % error on the value. However, for the presented g-factor measurement of $^{28}Si^{11+}$ the uncertainty of the mirror charge shift is below the statistical uncertainty and thus does not limit the uncertainty of the final g-factor value.

8.4.2 Lineshape of the axial dip fit

Since all frequency information is obtained from a measurement of the axial dip the uncertainties of the axial frequency determination have to be analyzed thoroughly. The frequency information is obtained from a fit to the axial dip with the lineshape given in Eq. (4.16). In the following the statistic and systematic uncertainties of this fit are discussed.

8.4.3 Statistical uncertainty of the dip fit

Due to the lower charge state of $^{28}Si^{11+}$ compared to $^{28}Si^{13+}$ the linewidth of the axial noise dip is decreased by a factor $(11/13)^2$ according to Eq. (4.14), which yields a dip width of 1.35 Hz. Thus, the resolution of the FFT-analysis had to be increased to resolve the dip. This was achieved by an averaging time of 150 s. The effect of the averaging time and the dip width on the uncertainty of the dip fit has been discussed in the Ph.D.-thesis of Sven Sturm [61] and show that the precision increases with longer averaging times and smaller dip widths, respectively, as long as field fluctuations can be neglected. For an averaging time of 150 s the axial dip frequency of $^{28}Si^{11+}$ can be determined with an uncertainty of $\delta\nu_z$=25 mHz.
The modified cyclotron frequency is determined with the double-dip technique according to Eq. (4.34) and the corresponding uncertainty due to the axial dip fit can be calculated to

$$\delta\nu_+ \simeq \sqrt{\delta\nu_z^2 + \delta\nu_l^2 + \delta\nu_r^2}. \tag{8.8}$$

The uncertainty of the coupling frequency is always neglected since all frequency synthesizer are synchronized to the same frequency reference (see Sec. 8.4.8). The axial frequency is measured before and after the double-dip measurement and the average of both is used for the calculation of the modified cyclotron frequency, which reduces the uncertainty of the axial frequency by a factor of $\sqrt{2}$. For the narrower double-dips the uncertainty is conservatively assumed to be the same as for the single dip $\delta\nu_l = \delta\nu_r = \delta\nu_z$. As a result the modified cyclotron frequency can be determined with a relative uncertainty of

$$\frac{\delta\nu_+}{\nu_+} \simeq \frac{\sqrt{2\delta\nu_z^2 + 0.5\delta\nu_z^2}}{\nu_+} = 1.8 \cdot 10^{-9}. \tag{8.9}$$

The precision of this single measurement can be improved by many repeated measurements. For the g-factor measurement the width of the obtained g-factor resonance determines the achievable precision.

Systematic shift of the dip fit

For the lineshape of the fit to the axial noise dip, the parameters of the resonator, namely the resonance frequency $\omega_R = 2\pi\nu_R$, the quality factor Q, and the frequency dependence κ_{det} are required. The fit is robust to a variation of Q and κ_{det} but sensitive to a change of ν_R. The dependence of the resulting axial frequency on ν_R has been investigated by fitting simulated dips with different ν_R. The result yields a linear dependence of the axial frequency shift $\Delta\nu_z$ on the deviation from the correct resonance frequency $\Delta\nu_R$ according to $\Delta\nu_z/\Delta\nu_R = 5.8 \cdot 10^{-4}$. ν_R can be determined either by fitting the noise resonance of the detection circuit or by fitting a long averaged axial dip for different resonator parameters

and minimize the chi-square of the fit. The two determined ν_R differs by 10 Hz, which corresponds to a systematic uncertainty of the axial frequency of

$$\frac{\Delta\nu_z}{\nu_z} = 8 \cdot 10^{-9}. \tag{8.10}$$

This can be neglected due to the additional suppression by a factor of $(\nu_z/\nu_+)^2 = 1/900$ for the uncertainty of ν_c.
However, the modified cyclotron frequency is determined with the double-dip technique and thus via the axial noise dip as well. Accordingly, the influence of the systematic uncertainty of the fit parameter on the modified cyclotron frequency has to be considered and is calculated to

$$\nu'_+ = \nu_{rf} - (\nu_z + \Delta\nu_z) + (\nu_l + \Delta\nu_z) + (\nu_r + \Delta\nu_z) \tag{8.11}$$

$$= \nu_+ + \Delta\nu_z. \tag{8.12}$$

Based on this consideration the magnetron frequency is shifted to

$$\nu'_- = \nu_- - \Delta\nu_z \tag{8.13}$$

and the corresponding systematic shift of the free cyclotron frequency amounts to

$$\Delta\nu_c = \sqrt{(\nu_+ + \Delta\nu_z)^2 + (\nu_z + \Delta\nu_z)^2 + (\nu_- - \Delta\nu_z)^2} - \nu_c \tag{8.14}$$

$$\simeq \sqrt{\nu_c^2 + 2\nu_+\Delta\nu_z + 2\nu_z\Delta\nu_z - 2\nu_-\Delta\nu_z + 3\Delta\nu_z^2} - \nu_c \tag{8.15}$$

$$\simeq \nu_c\sqrt{1 + \frac{2\Delta\nu_z(\nu_+ + \nu_z - \nu_-) + 3\Delta\nu_z^2}{\nu_c^2}} - \nu_c \tag{8.16}$$

$$\simeq 6\,\text{mHz}. \tag{8.17}$$

Accordingly, a systematic uncertainty of $\delta\nu_c/\nu_c = 2.6 \cdot 10^{-10}$ has to be considered for the final g-factor value.

8.4.4 Uncertainties due to the magnetic trapping potential

In order to avoid a broadening of the g-factor resonance by measuring the frequency ratio in a very homogeneous magnetic field, the frequency ratio measurement was spatially separated from the spin state analysis by the double-Penning trap technique. Due to the large distance between analysis trap and precision trap in the current setup the magnetic inhomogeneity in the precision trap is only $B_2 = 0.52(16)\,\mu\text{T/mm}^{-2}$. According to Eq. (3.18) the resulting shift of the modified cyclotron frequency can be calculated to $\Delta\nu_+/\nu_+ = 1 \cdot 10^{-11}$ for an axial temperature of $T_z = 4.8\,\text{K}$ and the corresponding radial temperatures (see Eq. 8.4). However, the shift of the Larmor frequency $\Delta\nu_L/\nu_L$ is exactly the same and since both frequencies are measured simultaneously during the g-factor measurement this leading order

dependence cancels. The remaining contribution to the shift of the free cyclotron frequency arises from the axial frequency shift $\Delta\nu_z/\nu_z = 3.5 \cdot 10^{-10}$. For the measurement of the modified cyclotron frequency with the double-dip technique the corresponding shift of the free cyclotron frequency can be calculated analogous as presented in Sec. 8.4.3 and amounts to

$$\frac{\Delta\nu_c}{\nu_c} \simeq 1.1 \cdot 10^{-11}, \tag{8.18}$$

which can be neglected at the presented level of accuracy.

8.4.5 Uncertainties due to the electrostatic trapping potential

Two essentially different effects of the electrostatic trapping potential on the g-factor have to be considered. On the one hand a shift of the eigenfrequencies due to a non-vanishing C_4-term and on the other hand a drift of the electric potential during the double-dip measurement for the modified cyclotron frequency. Both effects are discussed in the following.

Anharmonicity of the electrostatic potential

In the presence of electrostatic anharmonicities the eigenfrequencies of the ion are shifted as a function of the energy in the three eigenmodes. As shown in Sec. 7.5.1, the trapping potential can be optimized with an uncertainty below 10^{-5}. The C_4-term depends linearly on the detuning of the TR

$$C_4 = \Delta TR \cdot D_4 = 6.8 \cdot 10^4\,\mathrm{m}^{-4}, \tag{8.19}$$

where D_4 has been numerically calculated for our trap to $D_4 = 6.8 \cdot 10^9\,\mathrm{m}^{-4}$ in [61]. According to Eq. (3.16) the corresponding shift for the modified cyclotron frequency can be calculated to

$$\frac{\Delta\nu_+}{\nu_+} = \frac{6\,C_4 \cdot q \cdot U_R}{m^2 \cdot (2\pi\nu_z)^4} \cdot \left[\frac{1}{4}\left(\frac{\nu_z}{\nu_+}\right)^3 - \frac{1}{2}\left(\frac{\nu_z}{\nu_+}\right)^2 - \left(\frac{\nu_z}{\nu_+}\right)^2 \frac{\nu_-}{\nu_z}\right] \cdot E_z \tag{8.20}$$

$$= 2.5 \cdot 10^{-13} \tag{8.21}$$

for a $^{28}Si^{11+}$ ion with an axial temperature of $T_z = 4.8\,\mathrm{K}$ and a ring voltage of $U_R = -8.5\,V$. The relation between the axial and the radial energies according to Eq. (8.4) has been employed to express the shift as a function of the axial energy only. The shift for the axial frequency amounts to

$$\frac{\Delta\nu_z}{\nu_z} = -1.3 \cdot 10^{-10}. \tag{8.22}$$

As described in Sec. 8.4.3 the corresponding effect on the modified cyclotron frequency due to the employed double-dip technique has to be considered as well and thus, the free cyclotron frequency is shifted by

$$\frac{\Delta\nu_z}{\nu_z} = -4.1 \cdot 10^{-12}. \tag{8.23}$$

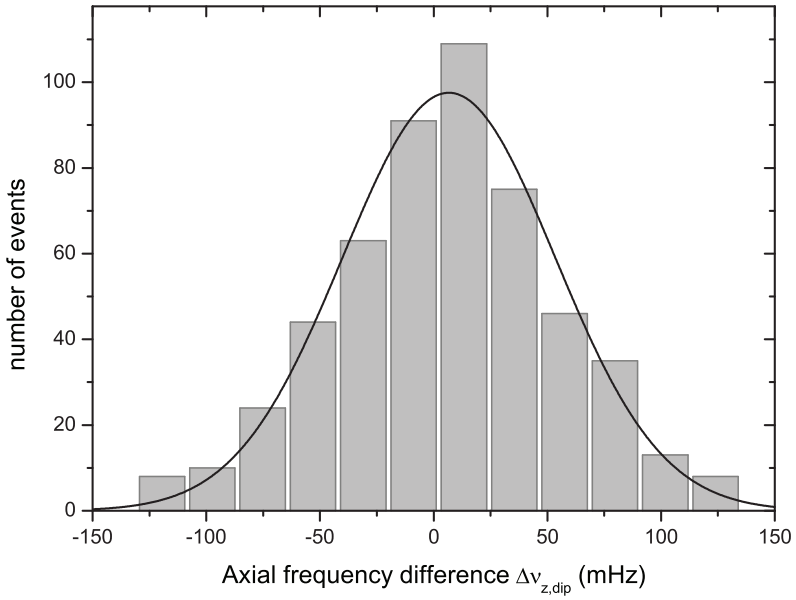

Figure 8.2: To analyze the axial frequency drift during the 150 s measurement time of the modified cyclotron frequency the frequency difference between the axial single dip before and after the double-dip measurement is plotted. Assuming statistical error bars, a fit with a Gaussian lineshape yields a systematic drift of the frequency of 6(2) mHz.

Accordingly, the shift due to a possible anharmonicity of the electrostatic trapping potential can be neglected.

Drift of the electrostatic potential

The modified cyclotron frequency is measured with the double-dip technique. While the double-dip is measured simultaneously to the microwave irradiation, the axial frequency, which is required for the double-dip technique as well, has to be measured separately. Assuming a linear drift of the electrostatic potential the effect on the modified cyclotron frequency can be eliminated by recording the single dip immediately before and after the double-dip measurement and utilizing the average of the two axial frequency measurements for the calculation of the modified cyclotron frequency. To analyze a possible drift of the axial frequency during the double-dip measurement, the axial frequency difference between the two single dips

$$\Delta\nu_{\mathrm{z,dip}} = \nu_{\mathrm{z,dip1}} - \nu_{\mathrm{z,dip2}} \tag{8.24}$$

is determined. The resulting histogram is shown in Fig. 8.2 and yields a systematic drift of 6(2) mHz, which is caused by the settling of the trapping voltage after transport. For a linear drift the influence on the g-factor is cancelled due to the averaging of the two dips. For a rather conservative estimate of a possible non-linear drift we assume an axial frequency error of $\frac{1}{4} \cdot 6\,\mathrm{mHz}$. This corresponds to a relative systematic shift of the free cyclotron frequency below $1 \cdot 10^{-10}$ and can be neglected.

Tilt of the electrostatic trapping potential

Although great care has been taken while assembling the trap-tower as well as inserting the apparatus into the magnet, a small tilt θ between the axis of the electrostatic trapping potential and the magnetic field is unavoidable since we have no possibility to adjust the alignment when the apparatus is placed in the magnet. A tilt results in a shift of the eigenfrequencies with respect to the ideal trap. However, the free cyclotron frequency is determined with the invariance theorem, which cancels frequency shifts due to a tilt or an ellipticity ϵ of the trapping potential to first order.
The invariance theorem not only eliminates the effect of trap imperfections but can also be utilized to estimate the size of the these imperfections. To this end the free cyclotron frequency obtained with the invariance theorem ν_c is compared to the sideband frequency $\overline{\nu}_\mathrm{c} = \nu_+ + \nu_-$, where shifts due to a tilted or distorted electric field do not cancel [57]. Both frequencies are related according to

$$\overline{\nu}_\mathrm{c} - \nu_\mathrm{c} = \nu_-(\frac{9}{4}\theta^2 - \frac{1}{2}\epsilon^2). \tag{8.25}$$

Assuming a vanishing ellipticity the tilt can be determined to

$$\theta = \sqrt{\frac{4}{9}\frac{\overline{\nu}_\mathrm{c} - \nu_\mathrm{c}}{\nu_-}} = (0.15 \pm 0.05)^\circ, \tag{8.26}$$

which demonstrates the precise alignment of the experimental setup.

8.4.6 Saturated g-factor resonance

For the three g-factor resonances recorded, a fractional spin flip rate of the order of 50 % was measured, implying that the resonances were saturated due to the high microwave power. Accordingly, a possible frequency shift of the maximum as well as a possible effect on the lineshape has to be analyzed thoroughly.

Lineshape of the g-factor resonance

The theoretical lineshape of the g-factor resonance has been derived in the Ph.D.-thesis of J. Verdú [100]. For small particle amplitudes the lineshape can be approximated by

a Gaussian lineshape. For high axial energies, however, in combination with a magnetic inhomogeneity B_2 the lineshape reflects the Boltzmann distribution of the axial energy and thus is asymmetric. Already for the g-factor measurement on $^{28}Si^{13+}$ the analysis of the lineshape revealed that with the current experimental setup the effect of the asymmetric contribution on the g-factor is below $\delta g/g \simeq 5 \cdot 10^{-11}$ [61] and thus a Gaussian lineshape was fit to the resonance. This is a result of the low particle amplitudes in combination with small magnetic field inhomogeneities. Accordingly, the achievable linewidth is determined by the fluctuations of the free cyclotron frequency, which are normally distributed and thus symmetric. For the g-factor measurement on $^{28}Si^{11+}$, performed in this thesis, the resonances were saturated, which leads to a symmetric broadening. Simulations of the resulting theoretical lineshape showed that the lineshape is completely dominated by the symmetric part, whereas the asymmetry can be neglected. Accordingly, the resonances were fit with a Gaussian lineshape.

Shift of the g-factor resonance

The effect of a saturated resonance on the frequency position of the maximum has already been investigated for the g-factor measurements of hydrogenlike carbon $^{12}C^{5+}$ and oxygen $^{16}O^{7+}$. For these experiments a significant shift of the maximum to higher frequencies for higher microwave powers was observed. This can be understood by considering large axial oscillation amplitudes of the ion in combination with a magnetic inhomogeneity B_2. The axial energy is Boltzmann distributed and fluctuates on time scales of the cooling constant. For large axial amplitudes the ion experiences a larger magnetic field due to the B_2-term. If the microwave power is high enough that the spin can be flipped at high axial energies and thus high magnetic fields, the Larmor frequency is shifted to higher frequencies, while the free cyclotron frequency is not affected. As a result the g-factor resonance is shifted to higher frequencies if the microwave power is increased.
However, the g-factor measurement of $^{28}Si^{11+}$ was performed at an axial temperature of $T_z = 4.8\,\mathrm{K}$ and thus considerably smaller axial amplitudes than for the $^{12}C^{5+}$ and $^{16}O^{7+}$ measurements performed at $T_z \simeq 61\,\mathrm{K}$ [53]. Moreover, the magnetic inhomogeneity is by a factor 20 smaller. Accordingly, a shift of the resonance is reduced by several orders of magnitude. In detail, the theoretical lineshape was calculated and the effect of the microwave power on the frequency position of the resonance was carefully analyzed for the conditions of our experiment. An overall variation of the microwave power by a factor of 1000 yielded a relative shift of the resonance position below 10^{-11}, which is completely negligible for the presented level of accuracy. This theoretical investigation is confirmed by the experimental measurements. Between the first and the third resonance the microwave power was varied by a total factor of about 50. As can be seen in Fig. 8.3 no dependence of the extracted g-factor value on the microwave power was observed. Due to the theoretical investigations

and the measured results it was concluded that the influence of the high microwave power on the final g-factor can be neglected due to the low axial energy of the ion.

8.4.7 Relativistic effects

The low modified cyclotron energy of $E_+ = 14\,\mathrm{meV}$ ($\beta = v/c \simeq 1 \cdot 10^{-6}$) during the sideband coupling results in a relative frequency shift due to a relativistic increase of the ion mass of

$$\frac{\Delta\nu_+}{\nu_+} \simeq -\frac{1}{mc^2}E_+ \simeq -5.2 \cdot 10^{-13}. \tag{8.27}$$

The shift of the Larmor frequency is even smaller and amounts to $\Delta\nu_\mathrm{L}/\nu_\mathrm{L} = -1.2 \cdot 10^{-13}$ according to Eq. (3.20). Thus, the frequency shifts due to relativistic effects can be neglected as well.

8.4.8 Time reference

In order to provide a common time reference for all involved devices the frequency synthesizers as well as the pulse generator and the FFT-analyzer are synchronized to a 10 MHz rubidium clock from Standford Research Systems. Accordingly, for the g-factor measurement where a frequency ratio is measured, the absolute uncertainty of the 10 MHz clock can be neglected and only the stability of the reference frequency is of importance. This is below $5 \cdot 10^{-11}$ for the considered time scales and thus eliminates uncertainties due to the time reference at the presented level of precision.

8.5 The final experimental result for the g-factor of $^{28}Si^{11+}$

We recorded three different g-factor resonances within a total measurement time of about four months. The microwave power was varied by an overall factor of about 50 between the first and the last resonance, hereby decreasing the width and thus improving the uncertainty of the extracted frequency ratio. As discussed in Sec. 8.4 the small oscillation amplitudes of the particle as well as the high harmonicity of the trapping potentials minimize the corresponding uncertainties to a negligible level. Only the frequency shift due to the interaction of the ion with its induced mirror charge as well as a systematic uncertainty of the fit to the axial dip have to be considered. Finally, after thorough analysis of the data and the investigation of possible uncertainties, the g-factor is determined. The weighted average of the three frequency ratios $\Gamma'_{\mathrm{exp},(\mathrm{i}=1,2,3)}$ shown in Fig. 8.3 is calculated to be

$$\Gamma'_\mathrm{exp} = 4637.318\,949(4). \tag{8.28}$$

This value has to be corrected for the mirror charge shift. Thus, the corrected frequency ratio amounts to

$$\Gamma_\mathrm{exp} = 4637.318\,946(4). \tag{8.29}$$

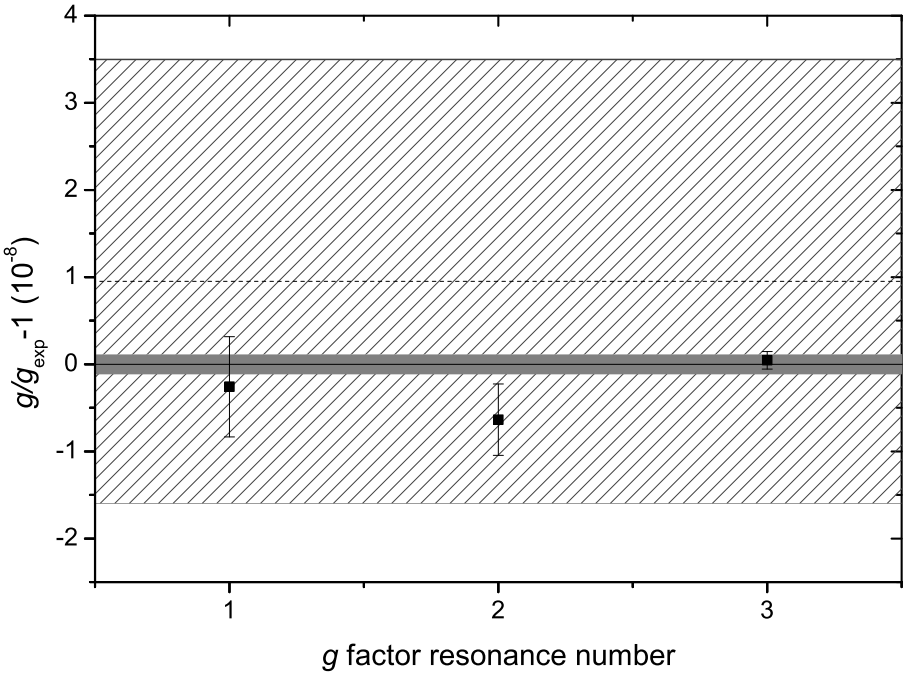

Figure 8.3: Comparison between the experimental and theoretical g-factor for $^{28}Si^{11+}$ [41]. We have recorded three resonance, which are indicated by the black squares. The microwave power has been varied by a total factor of ~ 50. The solid line is the weighted average of these three resonances with the corresponding experimental 1σ-uncertainty shown as a grey error band. The theoretical value is marked by the dashed line and the hatched area represents its uncertainty, being more than one order of magnitude less precise than the experimental value.

To determine the g-factor according to

$$g = 2\Gamma_{\mathrm{exp}} \frac{q}{e} \frac{m_{\mathrm{e}}}{m} \tag{8.30}$$

the mass of the electron and the ion, respectively, are required and thus have to be known to a sufficient accuracy. We take the electron mass

$$m_{\mathrm{e}} = 5.485\,799\,094\,6(22) \cdot 10^{-4}\,\mathrm{u} \tag{8.31}$$

from the 2010 CODATA compilation of fundamental constants [107]. The ion mass is obtained from the mass of the neutral silicon atom $m(^{28}\mathrm{Si}) = 27.976\,926\,534\,96(62)$ u measured by Redshaw *et al.* [108] corrected for the masses of the eleven missing electrons and their

respective binding energies taken from [109], which yields

$$m(^{28}\mathrm{Si}^{11+}) = 27.970\,894\,585\,81(66)\,\mathrm{u}. \tag{8.32}$$

With these values we determine the final experimental g-factor of lithiumlike silicon $^{28}\mathrm{Si}^{11+}$ to be

$$g_{\mathrm{exp}} = 2.000\,889\,889\,9(19)(5)(8). \tag{8.33}$$

The first error bar is the statistical uncertainty, the second one represents the systematic uncertainty and the last one the uncertainty due to the electron mass, respectively. The systematic error arises from the axial dip fit due to the limited knowledge of the required parameters of the detection system. The overall uncertainty of $\delta g/g = 1.1 \cdot 10^{-9}$ was limited by the low statistics due to the extremely low spin flip rate in the analysis trap.
This result is the most precise g-factor measurement of a three-electron system to date and the first determination of a lithiumlike g-factor with the double-Penning trap technique. Compared to the g-factor measurements of lithium ^{6,7}Li [19] with the atomic beam magnetic resonance technique and lithiumlike beryllium $^{9}\mathrm{Be}^{+}$ [20] with laser induced fluorescence the uncertainty is improved by two orders of magnitude and the sensitivity towards relativistic effects, which scale with the nuclear charge Z, is increased.

8.6 Comparison between experiment and theory

The theoretical value of the g-factor of lithiumlike silicon $^{28}\mathrm{Si}^{11+}$ was calculated to be [41]

$$g_{\mathrm{theo}} = 2.000\,889\,909(51), \tag{8.34}$$

which is in excellent agreement with the experimental g-factor value. The comparison between experiment and theory represents the most precise test of relativistic many-electron effects in magnetic fields. It confirms the relativistic many-electron calculations at the level of 10^{-4}, which is a factor of 15 more sensitive than the g-factor measurement of $^{9}\mathrm{Be}^{+}$ [20, 110]. The sensitivity of our test is limited by the accuracy of the theoretical predictions, which is more than one order of magnitude less precise than the experiment. Accordingly, an improvement of the theoretical uncertainty will directly enable an improved test of the calculations. Presently the theoretical accuracy is limited by the screened QED correction and the three-photon contribution to the interelectronic interaction. Rigorous calculation of these correction terms would further improve the theoretical g-factor and simultaneously the test of the relativistic many electron effects.
A special characteristic of the g-factor is the purely relativistic origin of the interelectronic interaction. As a result, the contribution of the negative energy Dirac states is of the

same order of magnitude as those of the positive states and thus, cannot be neglected. The correct treatment of the relativistic effects is only possible in the framework of QED, which, however, is rather difficult especially for higher orders like the two-photon exchange correction. Nevertheless it has been obtained for the case of the hyperfine splitting [44] and very recently for the g-factor of lithiumlike silicon [41]. It was found that the negative energy states contribute with -223 % and the positive energy states contribute with +323 % to the total two-photon correction, which is the sum of both (100 %). The experimental g-factor measurement confirms this result to 1 %, hereby verifying the necessity to consider the negative energy states for the theoretical calculation of the g-factor.

Chapter 9

Conclusion and outlook

In the course of this thesis the first g-factor measurement of a three-electron system with the double Penning trap technique has been performed. The g-factor of lithiumlike silicon $^{28}Si^{11+}$ has been measured to be

$$g_{\mathrm{exp}} = 2.000\,889\,889\,9(21). \tag{9.1}$$

The uncertainty is limited by the statistical uncertainty due to the low spin flip rate in the analysis trap, caused by technical problems, which could be solved after the measurement. Despite the resulting experimental challenges, concerning mainly the axial frequency stability over time periods up to half a day, the g-factor was measured with an uncertainty of $\delta g_{\mathrm{exp}}/g_{\mathrm{exp}} = 1.1 \cdot 10^{-9}$. This is the most precise g-factor measurement of a three-electron system to date. The theoretical prediction of

$$g_{\mathrm{theo}} = 2.000\,889\,909(51), \tag{9.2}$$

is in excellent agreement with the experimental observation. Thus, the comparison between experiment and theory constitutes the most sensitive test of the relativistic interelectronic interaction calculations in magnetic fields. It confirms the relativistic many-electron calculations at the level of 10^{-4} and the two-photon exchange correction in particular to 1 %. Since the experimental uncertainty is more than one order of magnitude better than the theoretical uncertainty it challenges theory to meet the experimental precision and thus to improve the test of the relativistic many-electron effects.

Environmental influences on the stability of the trapping potentials could be significantly minimized with the stabilization systems developed in the framework of this thesis. The temperature stabilization eliminates temperature induced fluctuations of the eigenfrequencies and especially of the axial frequency at the present level of precision.
The achievable precision for the g-factor measurement is limited by magnetic field fluctuations. In order to reduce fluctuations of the magnetic field a self-shielding superconducting

compensation coil was designed and implemented. The coil is wound around the trap chamber hereby also shielding fluctuations of the superconducting magnet itself. Although the available space was strictly limited, a geometry was found, which resulted in an additional shielding factor of 19 for external magnetic field fluctuations. In combination with the shielding factor of the magnet itself of 6.7, the magnetic field fluctuations seen by the ion in the trap are suppressed by an overall factor of 127(1). Another benefit of the compensation coil is that at the present level of precision no active pressure stabilization system is required for neither of the four cryogenic reservoirs. This significantly simplifies the experimental setup and reduces the susceptance to failure due to employed devices as well as possible source of noise. The possible limitation of a fluctuating tilt between the axis of the compensation and the magnetic field will be addressed by two additional transversal compensation coils, which are presently under design by my colleague F. Köhler.

9.1 Future *g*-factor measurements

The g-factors of hydrogenlike carbon, oxygen, silicon and now lithiumlike silicon have been measured over the past years with high accuracy down to a few parts in 10^{10}. The particular comparisons with the corresponding theoretical predictions provide stringent tests of QED theory. Still, there are a lot of fascinating measurements to be realized in the future, most of them relying on the g-factor measurement of hydrogen- and lithiumlike charge states. The probably most exciting perspectives are mentioned in the following.

9.1.1 Improvement of the electron mass

The achievable uncertainty of the experimental g-factor is presently limited by the uncertainty of the electron mass, which has been demonstrated by the g-factor measurement of $^{28}Si^{13+}$ with a precision of $\delta g/g = 5 \cdot 10^{-10}$ [61]. As a result it is planned to extract the electron mass from a g-factor measurement of hydrogenlike carbon $^{12}C^{5+}$

$$m_e = \frac{g_{\mathrm{theo}}}{2 \cdot \Gamma_0} \frac{e}{q} m \tag{9.3}$$

as it has already been done for the current value of the electron mass [111]. Due to the improved experimental setup and the new developed measurement technique for the modified cyclotron frequency [71] in comparison with an impressive theoretical accuracy [32], the determination of the electron mass by at least one order of magnitude more precise than the current CODATA value is feasible. Presently, this measurement is ongoing.

9.1.2 Heavy highly-charged ions

Since the BS-QED-contributions as well as the relativistic interelectronic interaction effects to the g-factor increase with the nuclear charge Z it is planned to extend the g-factor measurements to heavier ions. Our setup allows for the production of hydrogenlike ions up to calcium. The g-factor measurement of hydrogenlike and lithiumlike calcium $^{40}Ca^{19+,17+}$ with a similar precision as for silicon will allow for a more sensitive test of the BS-QED contributions and the relativistic many electron calculations. Moreover, the isotopic effect on the g-factor can be tested by comparing the g-factors of $^{40,48}Ca^{17+,19+}$.
For even heavier systems than calcium, the highly-charged ions have to be produced externally and injected into the trap as planned by the experiments, which are currently set up at HITRAP at the GSI Helmholtzzentrum für Schwerionenforschung in Darmstadt [112] and at the EBIT at MPIK in Heidelberg. However, the theoretical uncertainty of the g-factor for heavy ions is limited by the uncertainty due to the nuclear size correction, which increases strongly with Z. Fortunately, this limitation can be overcome by a comparison of the g-factor of the hydrogen- and the lithiumlike system of the same isotope [17]. Within this difference, the uncertainty of the nuclear size correction is significantly reduced and thus, the difference of the two g-factors can be calculated with a two orders of magnitude improved uncertainty. Accordingly, for a stringent test of QED with heavy systems the g-factor of the lithiumlike charge-state is required to be measured on the same level of accuracy as the hydrogenlike charge state.

9.1.3 Determination of the fine structure constant α

Besides the high-precision measurement of the electron mass another important fundamental constant can be extracted from a g-factor measurement - the fine structure constant α [34]. Here, again many-electron systems are essentially important, since the difference between the boron- and the hydrogenlike g-factor is required for the determination of α.
Presently, α is known with a relative precision of $\delta\alpha/\alpha = 2.6 \cdot 10^{-10}$ from the comparison between experiment and theory for the g-2 value [10] and thus depends strongly on QED calculations. A determination of α from the g-factor of the electron bound in heavy hydrogen- and boronlike ions will be largely independent from QED since the α-dependence of the bound g-factor mainly arises from the relativistic Breit-term. Therefore it was proposed to measure the g-factor of hydrogen- and boronlike lead [34] for a determination of α with a comparable precision as the value from the g-2 experiment.
To this end, a new experiment is presently setup by Sven Sturm at the MPIK in Heidelberg, which aims for the determination of the fine-structure constant α. The concept and the setup of the experiment will by very similar to our g-factor experiment on highly-charged ions in Mainz except for the trap, which has to provide open access for the highly-charged

ions from the Heidelberg EBIT [113]. The final uncertainty of α will be limited by the theoretical uncertainty but is expected to be at least comparable to the current value. From the experimental side, however, even a more precise determination of α seems to be feasible.

This outlook to the future g-factor measurements and the corresponding fascinating results concludes this thesis.

Bibliography

[1] S. Glashow. *Towards a unified theory: Threads in a tapestry.* Reviews of Modern Physics **52**(3), 539–543 (1980).

[2] T. Kinoshita. *Quantum electrodynamics.* World Scientific Publishing Company Incorporated (1990).

[3] S. Karshenboim. *Precision physics of simple atoms: QED tests, nuclear structure and fundamental constants.* Physics Rep. **422**, 1–63 (2005).

[4] R. P. Feynman. *QED: The Strange Theory of Light and Matter.* Princeton University Press (1988).

[5] W. Lamb and R. Retherford. *Fine structure of the hydrogen atom by a microwave method.* Phys. Rev. **72**, 241–243 (1947).

[6] P. Kusch and H. M. Foley. *Precision Measurement of the Ratio of the Atomic 'g Values' in the* $^2P_{\frac{3}{2}}$ *and* $^2P_{\frac{1}{2}}$ *States of Gallium.* Phys. Rev. **72**, 1256–1257 (1947).

[7] K. Blaum, Y. N. Novikov, and G. Werth. *Penning traps as a versatile tool for precise experiments in fundamental physics.* Contemp. Phys. **51**, 149–175 (2010).

[8] R. S. Van Dyck, P. B. Schwinberg, and H. G. Dehmelt. *Precise Measurements of Axial, Magnetron, Cyclotron, and Spin-Cyclotron-Beat Frequencies on an Isolated 1-meV Electron.* Phys. Rev. Lett. **38**, 310–314 (1977).

[9] D. Hanneke, S. Fogwell, and G. Gabrielse. *New Measurement of the Electron Magnetic Moment and the Fine Structure Constant.* Phys. Rev. Lett. **100**, 120801 (2008).

[10] T. Aoyama, M. Hayakawa, T. Kinoshita, and M. Nio. *Tenth-Order QED Contribution to the Electron g−2 and an Improved Value of the Fine Structure Constant.* Phys. Rev. Lett. **109**, 111807 (2012).

[11] T. Beier. *The* g_j *factor of a bound electron and the hyperfine stucture splitting in hydrogenlike ions.* Phys. Rep. **339**, 79 (2000).

[12] H. Persson *et al. A theoretical survey of QED tests in highly charged ions.* Hyperfine interactions **108**, 3–17 (1997).

[13] D. Glazov *et al. Tests of fundamental theories with heavy ions at low-energy regime.* Hyperfine Interactions **199**, 71–83 (2011).

[14] V. M. Shabaev *et al. Towards a test of QED in investigations of the hyperfine splitting in heavy ions.* Phys. Rev. Lett. **86**, 3959–3962 (2001).

[15] V. Yerokhin, P. Indelicato, and V. Shabaev. *Self-energy correction to the bound-electron g factor in H-like ions.* Phys. Rev. Lett. **89**, 143001 (2002).

[16] S. Sturm *et al. g Factor of Hydrogenlike* $^{28}Si^{13}$. Phys. Rev. Lett. **107**, 23002 (2011).

[17] V. M. Shabaev *et al. g factor of high-Z lithiumlike ions.* Phys. Rev. A **65**, 062104 (2002).

[18] V. M. Shabaev *et al. Theory of the* g *factor of lithium-like ions.* Nucl. Instr. and Meth. B **205**, 20–24 (2003).

[19] K. Böklen, W. Dankwort, E. Pitz, and S. Penselin. *High precision measurements of the g_J-factors of the alkalis using the atomic beam magnetic resonance method.* Phys. Lett. **21**, 294–295 (1966).

[20] D. J. Wineland, J. J. Bollinger, and W. M. Itano. *Laser-Fluorescence Mass Spectroscopy.* Phys. Rev. Lett. **50**, 628–631 (1983).

[21] A. Lapierre *et al. Lifetime measurement of the Ar XIV* $1s^2 2s^2 2p^2 P^o_{3/2}$ *metastable level at the Heidelberg electron-beam ion trap.* Phys. Rev. A **73**, 052507 (2006).

[22] I. Draganić *et al. High Precision Wavelength Measurements of QED-Sensitive Forbidden Transitions in Highly Charged Argon Ions.* Phys. Rev. Lett. **91**, 183001 (2003).

[23] W. Gerlach and O. Stern. *Der experimentelle Nachweis der Richtungsquantelung im Magnetfeld.* Zeitschrift für Physik A Hadrons and Nuclei **9**, 349–352 (1922).

[24] G. Uhlenbeck and S. Goudsmit. *Ersetzung der Hypothese vom unmechanischen Zwang durch eine Forderung bezüglich des inneren Verhaltens jedes einzelnen Elektrons.* Naturwissenschaften **13**, 953–954 (1925).

[25] P. Dirac. *The quantum theory of the electron.* Proceedings of the Royal Society of London. Series A **117**, 610–624 (1928).

[26] R. S. Van Dyck, P. B. Schwinberg, and H. G. Dehmelt. *Electron magnetic moment from geonium spectra: Early experiments and background concepts.* Phys. Rev. D **34**, 722–736 (1986).

[27] D. Ionescu *et al. Nonlinear extensions of the Dirac equation and their implications in QED.* Phys. Rev. A **38** (1988).

[28] H. Häffner *et al. High-Accuracy Measurement of the Magnetic Moment Anomaly of the Electron Bound in Hydrogenlike Carbon.* Phys. Rev. Lett. **85**, 5308–5311 (2000).

[29] J. Verdú *et al. Electronic g-Factor of Hydrogenlike Oxygen* $^{16}O^{7+}$. Phys. Rev. Lett. **92**, 093002 (2004).

[30] T. Beier *et al.* g_j *factor of an electron bound in a hydrogenlike ion.* Phys. Rev. A **62**, 032510 (2000).

[31] V. Shabaev and V. Yerokhin. *Recoil Correction to the Bound-Electron g Factor in H-like Atoms to All orders in* αZ. Phys. Rev. Lett. **88**, 91801 (2002).

[32] K. Pachucki, A. Czarnecki, U. D. Jentschura, and V. A. Yerokhin. *Complete two-loop correction to the bound-electron g factor.* Phys. Rev. A **72**, 022108 (2005).

[33] J. Zatorski, N. S. Oreshkina, C. H. Keitel, and Z. Harman. *Nuclear Shape Effect on the* g *Factor of Hydrogenlike Ions.* Phys. Rev. Let. **108**, 063005 (2012).

[34] V. M. Shabaev *et al. g-Factor of Heavy Ions: A New Access to the Fine Structure Constant.* Phys. Rev. Lett. **96**, 253002 (2006).

[35] T. Beier, P. Indelicato, V. Shabaev, and V. Yerokhin. *New value for the electron's mass—theoretical foundations.* J. Phys. B **36**, 1019 (2003).

[36] J. Schwinger. *On quantum-electrodynamics and the magnetic moment of the electron.* Phys. Rev. **73**, 416–417 (1948).

[37] R. Bouchendira *et al. New Determination of the Fine Structure Constant and Test of the Quantum Electrodynamics.* Phys. Rev. Lett. **106**, 080801 (2011).

[38] G. Breit. *The magnetic moment of the electron.* Nature **122**, 649–649 (1928).

[39] D. Glazov and V. Shabaev. *Finite nuclear size correction to the bound-electron g factor in a hydrogenlike atom.* Phys. Lett. A **297**, 408–411 (2002).

[40] A. V. Nefiodov, G. Plunien, and G. Soff. *Nuclear-Polarization Correction to the Bound-Electron g Factor in Heavy Hydrogenlike Ions.* Phys. Rev. Lett. **89**, 081802 (2002).

[41] A. Wagner *et al.* g *factor of lithiumlike silicon* $^{28}Si^{11+}$. submitted to Phys. Rev. Lett. (2012).

[42] D. A. Glazov *et al. Relativistic and QED corrections to the g factor of Li-like ions.* Phys. Rev. A **70**, 062104 (2004).

[43] D. A. Glazov, A. V. Volotka, and V. M. Shabaev. *private communication* (2012).

[44] A. V. Volotka *et al. Test of Many-Electron QED Effects in the Hyperfine Splitting of Heavy High-Z Ions.* Phys. Rev. Lett. **108**, 073001 (2012).

[45] V. A. Yerokhin, P. Indelicato, and V. M. Shabaev. *Evaluation of the self-energy correction to the g factor of S states in H-like ions.* Phys. Rev. A **69**, 052503 (2004).

[46] R. N. Lee, A. I. Milstein, I. S. Terekhov, and S. G. Karshenboim. *Virtual light-by-light scattering and the g factor of a bound electron.* Phys. Rev. A **71**, 052501 (2005).

[47] Z. Yan. *Calculations of magnetic moments for lithium-like ions.* J. Phys. B **35**, 1885 (2002).

[48] D. Glazov *et al. Screened QED corrections to the* g *factor of Li-like ions.* Phys. Lett. A **357**, 330–333 (2006).

[49] A. V. Volotka *et al. Screened QED Corrections in Lithiumlike Heavy Ions in the Presence of Magnetic Fields.* Phys. Rev. Lett. **103**, 033005 (2009).

[50] D. A. Glazov *et al. Evaluation of the screened QED corrections to the g factor and the hyperfine splitting of lithiumlike ions.* Phys. Rev. A **81**, 062112 (2010).

[51] V. M. Shabaev. *QED theory of the nuclear recoil effect on the atomic g factor.* Phys. Rev. A **64**, 052104 (2001).

[52] Z. Yan. *Calculations of magnetic moments for three-electron atomic systems.* Phys. Rev. Lett. **86**, 5683–5686 (2001).

[53] H. Häffner *et al. Double Penning trap technique for precise g factor determinations in highly charged ions.* Eur. Phys. J. D **22**, 163–182 (2003).

[54] L. Brown and G. Gabrielse. *Geonium theory: Physics of a single electron or ion in a Penning trap.* Rev. Mod. Phys. **58**, 233–311 (1986).

[55] K. Blaum. *High-accuracy mass spectrometry with stored ions.* Phys. Rep. **425**, 1–78 (2006).

[56] L. Brown and G. Gabrielse. *Precision spectroscopy of a charged particle in an imperfect Penning trap.* Phys. Rev. A **25**, 2423–2425 (1982).

[57] G. Gabrielse. *Why is sideband mass spectrometry possible with ions in a Penning trap?* Physical review letters **102**, 172501 (2009).

[58] G. Gabrielse, L. Haarsma, and S. L. Rolston. *Open-endcap Penning traps for high precision experiments.* Int. J. Mass Spectrom. Ion Processes **88**, 319–332 (1989).

[59] G. Gabrielse and F. MacKintosh. *Cylindrical Penning traps with orthogonalized anharmonicity compensation.* Int. J. Mass Spectrom. Ion Processes **57**, 1–17 (1984).

[60] G. Werth, H. Häffner, and W. Quint. *Continuous stern-gerlach effect on atomic ions.* Adv. At. Mol. Opt. Phys. **48**, 191–217 (2002).

[61] S. Sturm. *The* g*-factor of the electron bound in* $^{28}Si^{13+}$ *- The most stringent test of bound-state quantum electrodynamics.* Ph.D. thesis, Johannes Gutenberg-Universität Mainz (2012).

[62] B. Schabinger *et al. Experimental g factor of hydrogenlike silicon-28.* Eur. Phys. J. D **66**, 71 (2012).

[63] D. Lide. *Handbook of chemistry and physics.* CRC Press (2001).

[64] Stahl electronics. *UM1-14 and UM1-5; Ultrahigh Precision Multichannel Voltage Source.* Datasheet (2007).

[65] A. Wagner. *Design of a battery-based, low-noise voltage source for the experiment to measure the g-factor of the electron bound to highly-charged calcium ions.* Diploma thesis, Johannes Gutenberg-Universität Mainz (2008).

[66] S. Schabinger. *Ein Experiment zur Bestimmung des* g*-Faktors des gebundenen Elektrons in wasserstoff- und lithiumähnlichen mittelschweren Ionen.* Ph.D. thesis, Johannes Gutenberg-Universität Mainz (2011).

[67] S. Stahl *et al. Phase-sensitive measurement of trapped particle motions.* J. Phys. B **38**, 297–304 (2005).

[68] B. R. D'Urso. *Cooling and Self-Excitation of a One-Electron Oscillator.* Ph.D. thesis, Harvard University (2003).

[69] E. A. Cornell, R. M. Weisskoff, K. R. Boyce, and D. E. Pritchard. *Mode coupling in a Penning trap:* π *pulses and a classical avoided crossing.* Phys. Rev. A **41**, 312–315 (1990).

[70] M. Kretzschmar. *A Quantum Mechanical Model of Rabi Oscillations Between Two Interacting Harmonic Oscillator Modes and the Interconversion of Modes in a Penning Trap.* AIP Conf. Proc. **457**, 242 (1999).

[71] S. Sturm, A. Wagner, B. Schabinger, and K. Blaum. *Phase-Sensitive Cyclotron Frequency Measurements at Ultralow Energies.* Phys. Rev. Lett. **107**, 143003 (2011).

[72] E. A. Cornell *et al. Single-ion cyclotron resonance measurement of $M(CO^+)/M(N_2^+)$.* Phys. Rev. Lett. **63**, 1674–1677 (1989).

[73] S. Stahl. *Aufbau eines Experimentes zur Bestimung elektronischer g-Faktoren einzelner wasserstoffähnlicher Ionen.* Ph.D. thesis, Johannes Gutenberg-Universität Mainz (1998).

[74] J. Otamendi. *Development of an Experiment for Ultrahigh-Precision g-Factor Measurements in a Penning-Trap Setup.* Ph.D. thesis, Johannes Gutenberg-Universität Mainz (2007).

[75] J. Alonso *et al. A miniature electron-beam ion source for in-trap creation of highly charged ions.* Rev. Sci. Instrum. **77**, 03A901 (2006).

[76] A. Wagner *et al. A battery-based, low-noise voltage source.* Rev. Sci. Instrum. **81**, 064706–064706 (2010).

[77] M. König *et al. Quadrupole excitation of stored ion motion at the true cyclotron frequency.* Int. J. Mass Spectrom. Ion Processes **142**, 95–116 (1995).

[78] S. Brunner, T. Engel, and G. Werth. *Field stabilization of a superconducting magnet by helium pressure control.* Meas. Sci. Technol **6**, 222 (1999).

[79] R. Van Dyck, D. Farnham, S. Zafonte, and P. Schwinberg. *Ultrastable superconducting magnet system for a penning trap mass spectrometer.* Rev. Sci. Instrum. **70**, 1665–1671 (1999).

[80] I. Bergström *et al. SMILETRAP—A Penning trap facility for precision mass measurements using highly charged ions.* Nucl. Instrum. and Meth. A **487**, 618–651 (2002).

[81] M. Marie-Jeanne *et al. Towards a magnetic field stabilization at ISOLTRAP for high-accuracy mass measurements on exotic nuclides.* Nucl. Instrum. and Meth. A **587**, 464–473 (2008).

[82] C. Droese *et al. Investigation of the magnetic field fluctuation and implementation of a temperature and pressure stabilization at SHIPTRAP.* Nucl. Instrum. and Meth. A **632**, 157–163 (2011).

[83] R. Van Dyck, S. Zafonte, and P. Schwinberg. *Ultra-precise mass measurements using the UW-PTMS.* Hyperfine Interactions **132**, 163–175 (2001).

[84] P. W. Anderson. *Theory of Flux Creep in Hard Superconductors.* Phys. Rev. Lett. **9**, 309–311 (1962).

[85] P. W. Anderson and Y. B. Kim. *Hard Superconductivity: Theory of the Motion of Abrikosov Flux Lines.* Rev. Mod. Phys. **36**, 39–43 (1964).

[86] G. Gabrielse and J. Tan. *Self-shielding superconducting solenoid systems.* J. Appl. Phys **63** (1988).

[87] L. H. Zadeh. *Fuzzy Sets.* Information and Control **8**, 338–353 (1965).

[88] See:. *http://www.alamath.com.* for a program to calculate the Allan deviation.

[89] J. Ketelaer *et al. TRIGA-SPEC: A setup for mass spectrometry and laser spectroscopy at the research reactor TRIGA Mainz.* Nucl. Instrum. and Meth. A (2008).

[90] S. Sturm *et al. Challenging QED Calculations: Improved Measurement Accuracy in the* g*-Factor Determination of Hydrogenlike* $^{28}Si^{13+}$. submitted to PRL (2012).

[91] G. Gabrielse *et al. A Superconducting Solenoid System Which Cancels Fluctuations in the Ambient Magnetic Field.* J. Magn. Reson. **91**, 564–572 (1991).

[92] G. Bollen and S. Schwarz. *Penning trap mass measurements on rare isotopes—status and new developments.* J. Phys. B **36**, 941 (2003).

[93] S. Ulmer. *Entwicklung des experimentallen Aufbaus zur Messung des* g*-Faktors des Protons in einer Penning-Falle.* Diploma thesis, Ruperto-Carola-University of Heidelberg, Deutschland (2006).

[94] C. Buzea and T. Yamashita. *Review of the superconducting properties of* MgB_2. Superconductor Science and Technology **14**, R115 (2001).

[95] C. Mrozik. *Weiterentwicklung und Verbesserung des experimentellen Aufbaus zur Messung des magnetischen Moments des Protons.* Diploma thesis, Johannes Gutenberg-Universität Mainz (2009).

[96] H. Kracke. *Detection of individual spin transitions of a single proton confined in a cryogenic Penning trap.* Ph.D. thesis, Johannes Gutenberg-Universität Mainz (2013).

[97] F. Köhler. *in preparation.* Ph.D. thesis, Ruperto-Carola-University of Heidelberg, Germany (2014).

[98] J. Repp. *The setup of the high-precision Penning-trap mass spectrometer PENTATRAP and first production studies of highly charged ions.* Ph.D. thesis, Ruperto-Carola-University of Heidelberg, Germany (2012).

[99] S. Guan and A. Marshall. *Stored waveform inverse Fourier transform (SWIFT) ion excitation in trapped-ion mass spectrometry: Theory and applications.* Int. J. Mass Spectrom. Ion Processes **157**, 5–37 (1996).

[100] J. Verdú. *Ultrapräzise Messung des elektronischen g-Faktors in wasserstoffähnlichem Sauerstoff.* Ph.D. thesis, Johannes Gutenberg-Universität Mainz (2003).

[101] N. Hermanspahn. *Das magnetische Moment des gebundenen Elektrons in wasserstoffartigem Kohlenstoff (C^{5+}).* Ph.D. thesis, Johannes Gutenberg-Universität Mainz (1999).

[102] A. Van den Bos. *Parameter estimation for scientists and engineers.* Wiley Online Library (2007).

[103] R. S. Van Dyck, F. L. Moore, D. L. Farnham, and P. B. Schwinberg. *Number dependency in the compensated Penning trap.* Phys. Rev. A **40**, 6308–6313 (1989).

[104] J. V. Porto. *Series solution for the image charge fields in arbitrary cylindrically symmetric Penning traps.* Phys. Rev. A **64**, 023403 (2001).

[105] H. Häffner. *Präzisionsmessung des magnetischen Moments des Elektrons in wasserstoffähnlichem Kohlenstoff.* Ph.D. thesis, Johannes Gutenberg-Universität Mainz (2000).

[106] D. G. Boulware, L. S. Brown, and T. Lee. *Apparatus-dependent contributions to g-2?* Phys. Rev. D **32**, 729–735 (1985).

[107] P. J. Mohr, B. N. Taylor, and N. D. B. (2012). URL `http://physics.nist.gov/constants`.

[108] M. Redshaw, J. McDaniel, and E. G. Myers. *Dipole Moment of* PH^+ *and the Atomic Masses of* ^{28}Si, ^{31}P *by Comparing Cyclotron Frequencies of Two Ions Simultaneously Trapped in a Penning Trap.* Phys. Rev. Lett. **100**, 093002 (2008).

[109] W. Martin and R. Zalubas. *Energy levels of silicon, Si I through Si XIV.* Journal of physical and chemical reference data **12**, 323–380 (1983).

[110] E. Lindroth and A. Ynnerman. *Ab initio calculations of g_j factors for* Li, Be^+, *and* Ba^+. Phys. Rev. A **47**, 961–970 (1993).

[111] T. Beier *et al. New Determination of the Electron's Mass.* Phys. Rev. Lett. **88**, 11603 (2001).

[112] F. Herfurth *et al. Precision measurements with highly charged ions at rest: The HITRAP project at GSI.* Int. J. Mass Spectrom. **251**, 266–272 (2006).

[113] A. Martínez *et al. The Heidelberg EBIT: Present results and future perspectives.* In *Journal of Physics: Conference Series*, 1, 012001. IOP Publishing (2007).

Danksagung

Jetzt ist es soweit - die Doktorarbeit ist geschrieben, nur die Danksagung fehlt noch. Schon lange grübele ich immer mal wieder wie ich es bewerkstelligen kann meine Dankbarkeit für euch in Worte zu fassen. Es wird mir höchstens ansatzweise gelingen.

Mein größter Dank gilt *Prof. Dr. Klaus Blaum* aus unzähligen Gründen die ich gar nicht alle aufzählen kann. Deine Freude an der Physik und an deiner Arbeit sind immer wieder auf's Neue ansteckend. Danke für die Möglichkeit an diesem Experiment und in dieser Gruppe promovieren zu dürfen. Danke, für all deine Hilfe auch über die Physik hinaus und dein Vertrauen in mich. Danke, für alles was du mir ermöglicht hast. Danke für deine Mühe mit den Korrekturen in den letzten Wochen und die erheiternden eMails spät in der Nacht. Danke, dass du immer und für jede Frage überall auf der Welt erreichbar bist egal wie viele Arbeitsstunden deine Woche hat. Und ganz besonders danke ich dir für deine selbstverständliche helfende, unterstützende, motivierende und immer herzliche Art - die doch so überhaupt nicht selbstverständlich ist.

Prof. Dr. Selim Jochim danke ich für die Bereitschaft meine Arbeit als zweiter Gutachter zu betreuen.

Prof. Dr. Günter Werth danke ich für die Unterstützung bei Manuskripten jeder Art und für die Bereitschaft seine große Erfahrung im Bereich der Penning-Fallen Physik und beim Schreiben von Artikeln mit uns zu teilen. Außerdem für die unterhaltsamen Geschichten aus allen Gegenden dieser Welt.

Ich danke *Dr. Wolfgang Quint* für seine Beiträge zu unserem Experiment und das gemeinsame Rätseln über unser AT-Problem.

Ganz besonders bedanken möchte ich mich bei *Sven Sturm* für die gemeinsamen Jahre im Labor. Danke für all die lustigen Momente und die Freundschaft die sich entwickelt hat. Danke für das gemeinsame Durchstehen von schweren Zeiten, nicht nur beim Experiment, aber auch für das gemeinsame Feiern von Erfolgen. Du bist ein unerschöpflicher Quell von Wissen und neuen Ideen und du bist immer gerne bereit diese mit anderen zu teilen. Danke, dass du auch während der heißen Phase deines Schreibens immer bereit warst über das Ex-

periment zu diskutieren. Ich danke dir für alles was ich von dir gelernt habe und wünsche dir ganz viel Erfolg für dein Experiment. Ganz besonders wünsche ich dir α und bin gespannt auf das was noch kommt.

Ich möchte *Birgit Schabinger* danken für die gemeinsame Zeit im Labor und für die vielen Gepräche auch über die Physik hinaus. Du warst immer da, immer hilfsbereit und hast mit deiner unermüdlichen Arbeit den Grundstein für diese und die kommenden g-Faktor Messungen gelegt.

Florian Köhler danke ich vor allem für seine fröhliche und ausgeglichene Art besonders in den Momenten wo mal wieder gar nichts klappt. Und deine Bereitschaft dir dann mein Gejammer anzuhören. Ich drücke dir fest die Daumen für den Faktor 20.

Besonders danken möchte ich *Crícia de Carvalho Rodegheri*. Unser legendäres Gespräch bei den MATS-Tagen wird mir immer in Erinnerung bleiben und war der Beginn einer wunderbaren Freundschaft. Ich danke dir - du weißt wofür.

Bedanken möchte ich mich auch bei allen (ehemaligen) Mitarbeitern aus der *MATS-Gruppe* aus Mainz und Heidelberg für die tolle Arbeitsatmosphäre und den hilfreichen Erfahrungsaustausch, sowie für die vielen gemeinsamen Aktivitäten auch abseits der Physik. Holger, Julia, Stefan, Szilard - unsere Finnland-Konferenz und die abschließende Odyssee durch Europa war ein einmaliges Erlebnis an das ich immer gerne zurückdenke.

I would like to thank *Prof. Dr. Vladimir Shabaev, Dr. Günter Plunien, Dr. Dmitry Glazov* and *Dr. Andrey Volotka* for the great collaboration. Andrey and Dmitry, thanks for the patient answers to all the questions concerning the theoretical calculations. And especially thank you for finding the right words to explain your difficult and complex calculations to an experimentalist. Andrey, thank you for reading my theoretical chapter and checking if I wrote everything correctly.

Erwin Gries und *Herbert Geibel* möchte ich für ihre Hilfsbereitschaft bei allen kryotechnischen Problemen danken und dafür dass sie die Heliumkanne gefüllt haben auch wenn wir mal wieder vergessen haben sie zurück zu bringen.

Ich danke den *Mitarbeitern der Werkstätten des Instituts für Physik* für die jederzeit spontane Hilfestellung wenn mal wieder etwas ganz schnell und eigentlich sofort gemacht werden musste. Insbesondere danke ich Herrn Felzer für die hilfreichen Diskussionen und Ideen bezüglich der Herstellung eines supraleitenden Joints.

Ich danke den vielen guten Seelen, die uns in allen Bereichen neben der Physik unterstützen: *Christine Best, Elvira Stuck-Kerth, Gertraud Dücker* und dem Team der Warenannahme *Anton Gläser, Wolfram Vogt* und *Maria Barna*.

Außerdem möchte ich ganz besonders *meiner Familie* danken vor allem dafür, dass sie immer hinter mir stehen und mich unterstützen. Und einfach dafür, dass es sie gibt.
Danke *Mama*, für dein Mitfiebern, Mitleiden und Mitfreuen in allen Bereichen. Danke, dass du zu jeder unmenschlichen Zeit mit in den Stall gekommen bist. Danke für die vielen Schokoballen. Ganz besonders danke ich dir für Gina und dafür dass du dich immer um sie gekümmert hast wenn ich keine Zeit hatte, besonders in den letzten Wochen.
Danke *Papa* für deinen unerschütterlichen Glauben, dass die Wissenschaft genau das richtige für mich ist. Danke, für die vielen Gespräche und deine Ratschläge in allen Lebenslagen. Danke für die vielen vielen Fahrten von und nach Camberg bei denen ich so manche Stunde Schlaf nachholen konnte. Ich danke dir und Marion für eure Unterstützung in allen Bereichen meines "Neustarts".
Meinen Geschwistern *Nils, Arne* und *Silke* danke ich dafür, dass sie da waren wenn ich sie gebraucht habe.

Zu guter Letzt danke ich dir *Holger*. Ich danke dir für deinen Glauben an mich und deine Hilfe und Unterstützung in jeder Beziehung. Für die Bereitschaft auch Samstags nachts über Physik zu diskutieren oder mit mir den Fehler im LabView Programm zu suchen. Für die vielen unermüdlichen Korrekturen und Diskussionen über Frequenzshifts. Für deinen Optimismus und deine aufmunternden Worte wenn das Experiment mal wieder gar nicht so wollte wie es sollte. Dafür, dass du mich trotzdem zum Lachen gebracht hast. Für Ablenkung und Ansporn in den richtigen Momenten. Für deine Gelassenheit und deine Geduld. Und am allermeisten danke ich dir für deine Liebe und für deine Freundschaft.

Ihr alle habt einen wichtigen Anteil an dieser Arbeit und ich danke euch von ganzem Herzen.